ABSTRACT

Convection from Laser-Scanned Real Ice Roughness on a Simulated NACA 0012 Airfoil

David Matthew Hawkins, M.S.M.E.

Mentor: Stephen T. McClain, Ph.D.

Aircraft surfaces develop ice accretions under certain in-flight conditions. Ice accretions on aircraft surfaces increase skin friction drag, decrease lift, and increase the aircraft weight. Computational models of ice accretion on airfoils can be performed with the LEWICE code developed at the NASA Glenn Research Center. Previous research to improve the convection models in LEWICE used multiple surface representations of ice roughness in both accelerated flows and flows with negligible acceleration. However, the earlier work used simulated surface roughness elements such as cones and hemispheres to enhance convective heat transfer. The current research examines convective heat transfer along test plates with surface panels replicating laser-scanned real ice roughness along the leading 17.1% (3.6 in.) of a 21 in. NACA 0012 airfoil. A new leading edge trip is also used to force turbulent flow over the surfaces for comparison with data from naturally transitioning flow cases.

Convection from Laser-Scanned Real Ice Roughness on a Simulated NACA 0012 Airfoil

by

David Matthew Hawkins, B.S.M.E.

A Thesis

Approved by the Department of Mechanical Engineering

____

Kenneth Van Treuren, Ph.D., Chairperson

Submitted to the Graduate Faculty of
Baylor University in Partial Fulfillment of the
Requirements for the Degree
of

Master of Science in Mechanical Engineering

Approved by the Thesis Committee

____

Stephen T. McClain, Ph.D., Chairperson

____

David Jack, Ph.D.

____

Randall Jean, Ph.D.

Accepted by the Graduate School
December 2016

____

J. Larry Lyon, Ph.D., Dean

Page bearing signatures is kept on file in the Graduate School.

TABLE OF CONTENTS

LIST OF FIGURES

LIST OF TABLES

NOMENCLATURE

A_c	Ice accretion parameter
A_{pix}	Pixel area (4.00E-04 in^2)
A_t	Total area of heated section
b^n	Winning codebook vector
B_T	Correlated uncertainty (1.4 K)
c	Airfoil chord length
C_D	Coefficient of drag
C_{D_F}	Friction drag coefficient
C_{D_P}	Pressure drag coefficient
c_f	Skin friction coefficient
C_k	Conduction parameter for the k^{th} heated section (0.9, 0.9, 1.05, 1.1, 1.05)
c_p	Specific heat of fluid
C_p	Pressure coefficient
D	Drag
E	Voltage across heater
F_s	Surface geometry scaling factor (10)
F_t	Transition function
F_x	Force in the x-direction acting on the surface of an object
g	Acceleration of gravity vector
g_x	Component of the acceleration of gravity vector in the x direction

g_y	Component of the acceleration of gravity vector in the y direction
h	Convective heat transfer (convection) coefficient
I	Current through heater
k	Measured roughness element height
k_f	Thermal conductivity of fluid
k_p	Thermal conductivity of Plexiglas (0.205 W/mK)
k_s	Thermal conductivity of solid OR sand-grain roughness element height
k_φ	Thermal conductivity of body in direction normal to the surface
L_{ha}	Length of heated section
l_t	Transition length
N	Direction normal to the ice manifold in the direction of flow OR measurement sample size
N^0	Direction normal to the airfoil surface in the direction of flow
$N_{f,stag}$	Freezing fraction at stagnation point
N_x^j	Orthogonal distance from an ice surface point to the mean ice shape
p	Pressure
p_∞	Freestream pressure
Pr	Prandtl number
Q	Heat expressed as an energy quantity
$\dot{Q}$	The rate at which energy flows from one boundary to another
$\dot{Q}_{conv}$	Convection term in data reduction equation
$\dot{Q}_{cond}$	Conduction term in data reduction equation
$\dot{Q}_{gen}$	Heat generation term in data reduction equation
$\dot{Q}_{rad}$	Radiation term in data reduction equation

q''_{evap}	Evaporative heat loss from surface water
q''_{ke}	Kinetic heat gain to body from impinging droplets
q''_{lat}	Latent heat gain to body from freezing
q''_{nc}	Net convective heat loss from body
q''_{sens}	Sensible heat loss (or gain) from surface water
q''_{w}	Wall heat flux
r_a	Leading edge radius of curvature of NACA 0012 airfoil
Re	Reynolds number
Rq	Roughness height root-mean-square
s	Surface direction along airfoil
S	Direction along mean ice manifold in the direction of flow OR Standard deviation
S^0	Direction along airfoil surface in the direction of flow
S_E	Element diameter standard deviation
St	Stanton number
T_∞	Freestream temperature
T_{BL}	Temperature inside boundary layer
T_{IR}	IR camera temperature reading
T_s	Surface temperature
T_{SS}	Calibrated subsurface thermocouple temperature
T_{UP}	Calibrated under plate thermocouple temperature
t	time OR Student's t-value
t_p	Plexiglas sub-plate thickness (0.72″)
t_s	Exposure time to icing conditions

u	Streamwise velocity inside a boundary layer
U	Uncertainty
U_∞	Freestream velocity
U_{CI}	Cut in velocity (5 m/s)
U_e	Local freestream velocity
V	Velocity vector
V_{eff}	Effective velocity measured by hot-film wire(s)
V_{meas}	Measured velocity by Pitot-static probe
V_N	Velocity normal to hot-film wire
V_T	Velocity tangential to hot-film wire
w	Wall-normal velocity
W_{ha}	Width of heated section
x	Streamwise location on plate
x_{cr}	Critical distance for flow transition
x_k	Sand-grain equivalent roughness height in LEWICE
x_t	Transition location
z	Wall-normal distance from plate surface

Greek

α	Thermal diffusivity OR angle of wire of x-array probe
δ	Velocity boundary layer height
δ_T	Thermal boundary layer height
Δt_s	Ice accretion time
θ	Angle of velocity vector

ε	Emissivity (0.95)
ζ	Dummy integration variable representing x in Stanton number correlations
κ	Tangential velocity attenuation factor (0.115)
μ	Dynamic fluid viscosity
ν	Kinematic fluid viscosity
ξ	Unheated starting length (1.7285″)
ρ	Fluid density
ρ_{ice}	Ice density
σ	Stefan-Boltzmann constant (5.67E-8 W/m^2K^4)
τ_w	Wall shear stress
φ	Direction normal to body surface

Subscripts

TC,cal	Thermocouple temperature measurement during calibration
TC,test	Thermocouple temperature measurement during test
IR,cal	Infrared temperature measurement during calibration
FS	Freestream temperature as measured by thermocouples

Abbreviations

AOA	Angle of attack
ABS	Acrylonitrile butadiene styrene
BUSWT	Baylor University subsonic wind tunnel
CNC	Computer numerical control
CAD	Computer aided design

DEM	Discrete element method
ES-DEM	Extended surface discrete element method
FAA	Federal aviation administration
IR	Infrared
IRT	Icing research tunnel
LWC	Liquid water content
MVD	Median volumetric diameter
NACA	National advisory committee for aeronautics
NASA	National aeronautics and space administration
RMH	Roughness maximum height
SLD	Supercooled large droplets
SOM	Self-organizing maps
STL	Stereolithography file format
VIST	Vertical icing studies tunnel

ACKNOWLEDGMENTS

For years, musicians have shouted “is there anybody out there?” to concertgoers, with no response other than a hearty “wooo!” I’m here to answer that question from a different stage. There are lots of people “out there” who have helped me reach this point as a graduate student. Some of you have changed the trajectory of my life. Without you, I would not be here now writing these words.

My graduate advisor, Dr. Stephen McClain, has been an incredible mentor, and I would not have completed this project without him. Dr. McClain, thank you for seeing potential in me and allowing me to work on your team. I’m grateful for your time, your willingness to teach, and your patience. I would also like to thank Dr. David Jack and Dr. Randall Jean for serving on my thesis committee.

I am so thankful for my predecessors, Logan Tecson, Chris Walker, Mike Hughes, and Tim Shannon. Their contributions to this project built a solid foundation that allowed me to expand the work of this research grant. I also owe much thanks to Mr. Ashley Orr for his excellent work and guidance in helping me create the surfaces studied in this project. Thanks are due also to my fellow graduate students Tim Shannon, Mike Hughes, Timothy Russell, Andrew Hays, Kyle Vinton, and Travvis Scott for their friendship and support during the long hours we spent together.

Dr. David Jack has been my mentor and friend for many years, and I would not be where I am today without him. Dr. Jack, thank you for always pushing me to be better. As my Scoutmaster in Boy Scouts, you prepared me to be a responsible leader. When I

came to you discouraged about undergraduate engineering, you and the wonderful Mrs. Trisha Jack opened your home to me and showed me how engineering can be so much more exciting than I thought. As my professor during my time at Baylor, you offered me advice and encouragement about how to succeed. Thank you.

To my siblings, Katy, Zach, and Cameron, thank you so much for being there when I needed you. I'm glad we continue to grow closer over the years, and I'm so grateful for our conversations. Thanks for pointing out where I'm wrong, thanks for pushing my buttons, and thanks for the long phone calls which kept me sane. I must also thank my grandparents and extended family for cheering me on in my studies, for filling the holiday visits with joy, and for lovingly enduring the explanations of my various projects.

Finally, to my parents, thank you for the constant love and support. You taught me to go outside my comfort zone and to set high goals for myself. You've sacrificed to give me a phenomenal education, and to teach me to love Truth and beauty. Thanks for making life an adventure. "I'll check it out."

DEDICATION

To my loving parents who taught me magic,
And my kooky siblings who taught me ways to use it.

CHAPTER ONE

Introduction

Motivation

Ice accretions on aircraft surfaces pose a hazard for the aviation industry. In the 1920s, when powered airplanes were surging into popularity, a pilot for the U.S. Air Mail Service said “the greatest of all our problems is ice” [1]. Ice accretions continue to trouble modern aircraft as well, with 819 fatalities linked to airframe icing over a span of 19 years from 1982-2000 [2]. Accidents even occurred during summer months, with general aviation and commuter airlines encountering icing conditions at slow speeds in lower altitudes [2].

The dangers caused by ice accretions can grow very rapidly. One study showed that even two minutes in icing conditions has a significant effect on both the lift coefficient and stall angle of an airfoil [3]. The stall angle is the critical airfoil angle of attack (AOA) where increasing the angle of attack no longer increases the lift coefficient. An aircraft will stall if the stall angle is exceeded, which results in a rapid loss of lift. Figure 1.1 shows how quickly ice accretions on an airfoil influence the lift coefficient and stall angle [3]. In addition to a reduction to lift and stall margin, aircraft also experience increases in weight and skin friction drag from ice accretions. Further, ice accretions can also cause sensors and moving parts to fail.

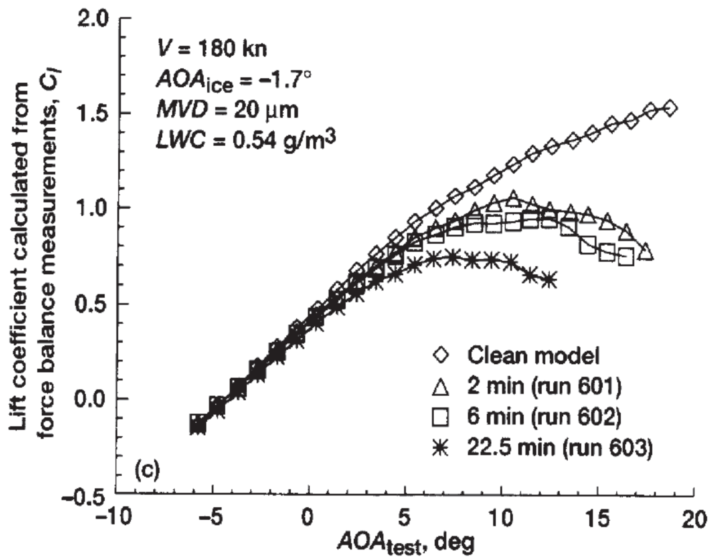

Figure 1.1: Effect of icing exposure time on airfoil lift per angle of attack (AOA) [3]

Pilots generally attempt to avoid icing conditions altogether, but they may not always find this possible. Of course, there are design options to prevent ice buildup (anti-icing) or to get rid of already accreted ice (de-icing).These practices include glycol-based antifreeze sprays, electrical heaters, hot engine air redirection, pneumatic boots, electro-pulse methods, or even ultrasound debonding [6]. Nevertheless, these systems are imperfect. They may fail in-flight, some require lots of energy to run, and all require extensive testing before being approved. Often they necessitate efficiency compromises in power or propulsion. Electrical power must be used to energize heating elements, or hot air must be taken away from the propulsion power of engines and redirected onto the icy surfaces [7].

Since 1964, the Federal Aviation Administration (FAA) has required airplane manufacturers to demonstrate that their aircraft can safely fly in icing conditions defined in Title 14, §25, Appendix C of the U.S. Code of Federal Regulations (known as Appendix C icing conditions) [8]. This code was updated in 2014 to define additional safe flight requirements in Appendix O icing conditions [9]. Ultimately, aircraft designers must make economically sensible choices for aircraft to tolerate some amount of ice accretion while still remaining operational. This results in expensive testing to demonstrate compliance. However, ice accretion prediction codes can reduce the amount of time and money required for testing by simulating the process [9].

LEWICE is an ice accretion prediction code developed by NASA and widely used in the commercial aviation industry. The code calculates the size and shape of ice accretions over time so that appropriate de-icing systems can be designed for many different weather conditions. LEWICE can still be improved, though, because the physics of ice accretion are not fully understood. LEWICE currently predicts ice accretion based on historical experimental correlations for the convective heat transfer from surface roughness [11]. Ice surface roughness is important because it couples the chaotic local fluid flow, droplet impingement, and heat transfer processes [4,10]. The historical roughness correlations are based on sand-grain equivalent sizes of roughness elements with simple geometries placed in ordered patterns. Real ice roughness is much more random, and LEWICE consistently over-predicts the convective heat transfer, especially when large protrusions develop, as seen in Figure 1.2.

Large protrusions are dependent on the early onset roughness which grows in the first one or two minutes of ice accretion. If the early roughness is modeled poorly, the predictions for ice protrusions which develop after longer exposure times will consequently be flawed as well. Therefore, it is important to develop an accurate model for how early ice roughness develops, and that has been the focus of recent icing studies at Baylor.

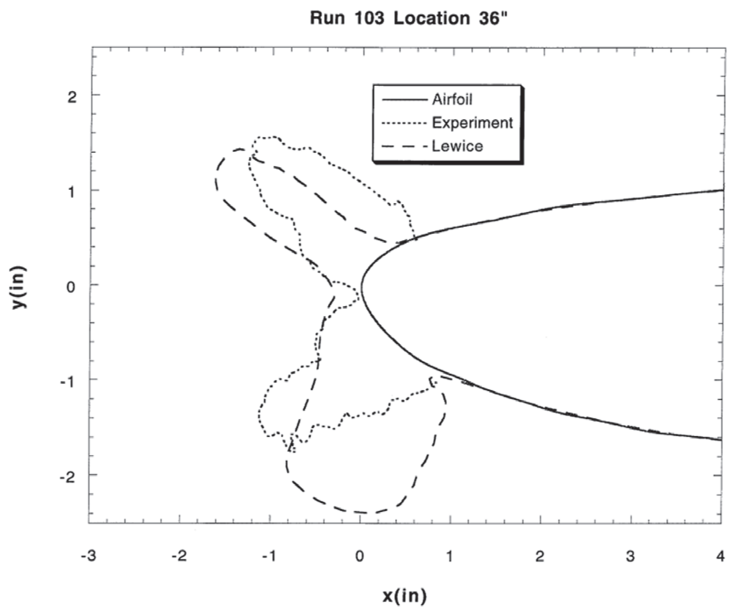

Figure 1.2: Comparison of LEWICE ice shape prediction to experimental accretion from the NASA Glenn Icing Research Tunnel [12]

To improve the prediction capabilities of LEWICE, previous studies at Baylor University have investigated different parameters of ice-accreted surface roughness. Tecson [13] used a Lagrangian droplet simulator to generate roughness with a random distribution to match historical experiments. He then made convective heat transfer enhancement measurements and velocity boundary layer measurements of these surfaces with negligible freestream acceleration, and with constant heat flux boundary conditions.

Since real ice accretions do not have a constant thickness, the heat flux through ice accretions is not uniform. Walker [14] retested the surfaces generated by Tecson using varying thermal boundary conditions. However, the surfaces used by Tecson [13] and Walker [14] were made with an abrupt smooth-to-rough transition with constant properties downstream in an effort to imitate historical experiments. Investigations in laser scanned ice accretions yielded preliminary information about real ice roughness shapes [15,16].

Shannon [17] created a new surface by scaling the Lagrangian droplet simulated roughness elements to match the streamwise size variations of a real ice laser scan. This surface was manufactured using both ABS plastic and machined aluminum so that the thermal conductivity of different materials could be compared. These surfaces were then tested with a constant heat flux boundary condition in flow with negligible freestream acceleration as before, and also with a ceiling insert to accelerate the flow to replicate flow acceleration found on the leading 17.1% chord of a 21" chord NACA 0012 airfoil, as seen in Figure 1.3. The majority of ice accretion occurs in the leading 17.1% chord region shown. The NACA 0012 airfoil was chosen because it is symmetric about the chord line, and is a good baseline to compare with future studies on more complex airfoils. The NACA 0012 airfoil has also been used in numerous historical studies, and is well-documented.

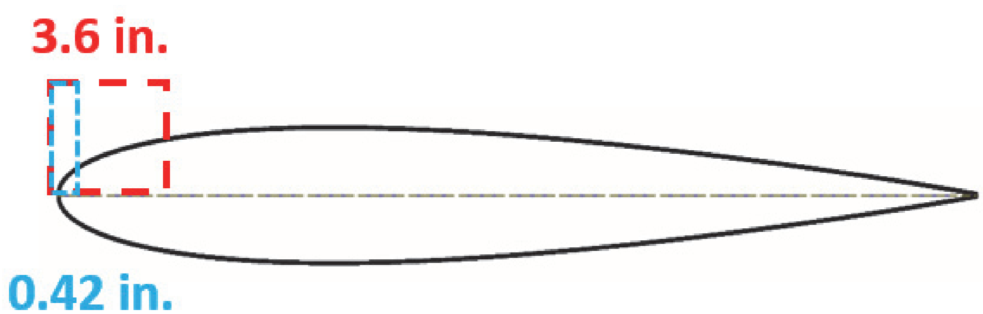

Figure 1.3: Diagram of a 21" chord NACA 0012 airfoil profile highlighting the leading 17.1% chord region (red) and the leading 2% chord region (blue) [18]

Because of the inherent nature of flow acceleration using a ceiling insert, the stagnation flow in the leading 2% of the chord was not matched. Therefore, Hughes [18] created new surfaces using the Lagrangian droplet simulator which were scaled to model realistic ice accretions on the stagnation region of the leading 2% chord of a 21" chord

NACA 0012 airfoil (seen in Figure 1.3), and these were studied in the Vertical Icing Studies Tunnel (VIST) at NASA Glenn Research Center. However, all of the surfaces mentioned in these studies used simulated roughness elements rather than real surface roughness.

Objectives and Significance of Work

Thanks to new developments in laser scanning, creating surface models of real ice roughness is now feasible [19]. The objective of this study is to improve upon the work of Tecson [13], Walker [14], Shannon [17], and Hughes [18] by 1) creating a new surface from an unwrapped laser scan of an ice accretion on a NACA 0012 airfoil, and 2) investigating the new surface in the same methods as the aforementioned experiments to test for correlation to previous studies. The real ice surface will be created from both ABS plastic and machined aluminum, and the surfaces will be studied in flows with negligible freestream acceleration and flows which replicate the acceleration found on the leading 17.1% chord of a NACA 0012 airfoil.

Further, this study will investigate the hypothesis that a thin film liquid layer near the stagnation point of an airfoil creates turbulent flow, leading to enhanced convective heat transfer. Convective heat transfer enhancement measurements and velocity boundary layer measurements will be acquired. Additionally, a new sawtooth leading edge trip will be created to force turbulent flow downstream of the trip. This will replicate turbulent flow possibly created by a thin film liquid layer near the stagnation point. For further comparison, two of the previous Lagrangian droplet simulated roughness surfaces will be retested using the sawtooth leading edge trip.

Presentation Outline

Chapter Two provides summarized technical background for fluid mechanics, heat transfer, airfoils, surface roughness, and a history of aircraft icing investigations. Chapter Three details the experimental methods used in the preparation and completion of this study. Chapter Four describes the data reduction methods used to analyze the data, as well as the uncertainty analysis. Chapter Five presents the results of the investigation and discusses the significance. Chapter Six presents conclusions from the results, recommendations for improving ice accretion codes, and suggestions for future work.

CHAPTER TWO

Technical Background

Fluid Mechanics and Heat Transfer

Velocity Boundary Layers

In 1904, Ludwig Prandtl introduced the concept of boundary layers in fluid flow over surfaces. Prior to this revelation, the role of friction in fluids—that is, viscosity—was unclear [20]. Fluids were treated as inviscid until the Navier-Stokes equations were derived in the mid-1800s. The Navier-Stokes equations consist of the continuity equation, the momentum equation, and the energy equation. In 2D, for unsteady, incompressible flow, in a regular Cartesian coordinate system, the Navier-Stokes equations (minus the energy equation) are presented below in Eqs. (2.1) through Eq. (2.3), respectively.

Continuity:
$$\frac{\partial(\rho u)}{\partial x}+\frac{\partial(\rho v)}{\partial y}=0 \tag{2.1}$$

X-Momentum:
$$\rho\left(\frac{\partial u}{\partial t}+u\frac{\partial u}{\partial x}+v\frac{\partial u}{\partial y}\right)=-\frac{\partial P}{\partial x}+\rho g_x+\mu\left(\frac{\partial^2 u}{\partial x^2}+\frac{\partial^2 u}{\partial y^2}\right) \tag{2.2}$$

Y-Momentum:
$$\rho\left(\frac{\partial v}{\partial t}+u\frac{\partial v}{\partial x}+v\frac{\partial v}{\partial y}\right)=-\frac{\partial P}{\partial y}+\rho g_y+\mu\left(\frac{\partial^2 v}{\partial x^2}+\frac{\partial^2 v}{\partial y^2}\right) \tag{2.3}$$

The Navier-Stokes equations were the first fluid flow model which accounted for internal friction (viscosity). These equations can be simplified and used to find some closed-form solutions under specific conditions and certain geometries, but they have never been solved analytically for a general flow case [21]. Without the ability to solve viscous flow problems, innovators like the Wright brothers were unable to calculate the frictional shear force on a surface in a fluid flow. Without the shear force, it was impossible to quantify properties like drag or predict flow separation from surfaces [20].

Prandtl's groundbreaking boundary layer concept was a new way of approaching fluid viscous resistance. He theorized that fluids behave as if inviscid except in a thin region near a surface—the boundary layer. Inside the boundary layer, fluid viscosity is very important because of the no-slip condition assumed at the surface. The no-slip condition is an experimental observation that fluid particles closest to a surface will have a velocity of zero relative to the surface [21]. Fluid velocity tangent to a surface must rapidly decrease from a nonzero value to a value of zero at the surface, and viscosity plays a huge role in how this happens. The fluid viscosity is assumed to be constant throughout the entire flow, but the viscous effects are much more important inside the boundary layer due to the large velocity gradients near the surface. Prandtl's boundary layer concept paved the way to a better understanding of shear stress, skin friction drag, and flow separation.

Figure 2.1 illustrates how a velocity boundary layer develops as fluid flows over a smooth flat plate. The flow which can be considered inviscid is the freestream velocity (U_∞). For a given distance down the plate (x), the velocity inside the boundary layer (u) will change as a function of the distance normal from the surface (z). The boundary layer thickness increases in the direction of the flow, and the thickness at any location x is called the boundary layer height (δ). The velocity of the flow at the surface is zero, and the velocity of the flow at δ is defined to be 99% of the freestream velocity.

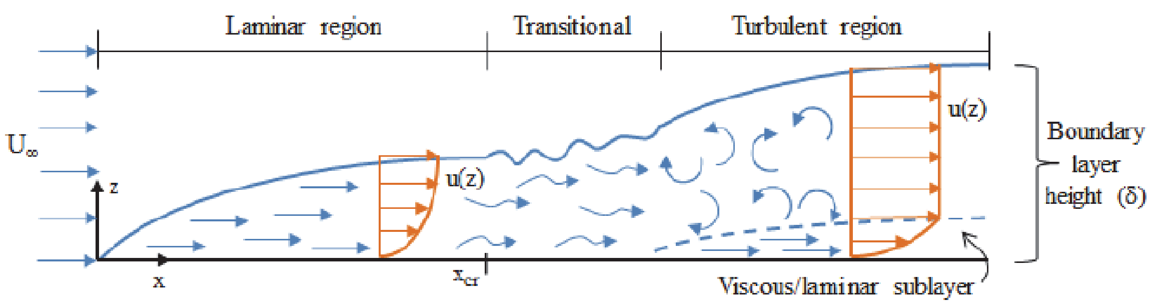

Figure 2.1: Velocity boundary layer development on a flat plate (not to scale) [13]

Outside the boundary layer, the freestream velocity flows in streamlines nearly parallel to the plate. Inside the boundary layer, the flow develops through three different regimes. The boundary layer begins in the laminar region, in which fluid particles move in well-ordered streamlines. Once a critical distance (x_c) has been reached from the leading edge of the plate, the fluid begins transitioning to turbulent flow. The turbulent region is chaotic due to high shearing stresses produced by the velocity gradient. The flow is dominated by swirling eddies, which are rotating areas of fluid. A very thin laminar viscous sublayer also forms beneath the turbulent region, and swirling eddies are extinguished because of the proximity to the surface. Even though the velocity in the turbulent region is highly chaotic, the time-averaged velocity profiles appear uniform in the turbulent region.

To characterize flows over surfaces so that multiple cases can be compared, it is helpful to quantify flows using Reynolds number. Reynolds number is a non-dimensional parameter which is commonly described as the ratio of inertial forces (the freestream) to viscous forces (flow in the boundary layer). It is also helpful to understand Reynolds number as a geometric slenderness ratio describing where viscous effects are important.

Flows with larger Reynolds numbers are considered turbulent and have thinner boundary layers. The local Reynolds number is defined in this context by Eq. (2.4) [21]

$$\mathrm{Re}_x = \frac{\rho U_\infty x}{\mu} \tag{2.4}$$

where ρ is the fluid density, U_∞ is the freestream velocity, x is the surface distance from the leading edge of the plate, and μ is the dynamic viscosity of the fluid. For flow over a smooth flat plate, a Reynolds number of less than $5\text{x}10^5$ is considered laminar, and flows with higher Reynolds numbers will either be transitional or turbulent. Reynolds number is useful for scaling experiments, because flows with similar Reynolds numbers will behave similarly to one another [21].

Because of the no-slip condition and the huge change in velocities within boundary layers, a wall shear stress (τ_w) will develop on a surface. Newton's shear-stress law "states that the shear stress is proportional to the velocity gradient" [20]. At the wall, the shear stress is given by Eq. (2.5) [21]

$$\tau_w = \mu \left. \frac{\partial u}{\partial z} \right|_{z=0} \tag{2.5}$$

where μ is the dynamic viscosity of the fluid and $\frac{\partial u}{\partial z}$ is the velocity gradient.

Quantifying a surface's shear stress is important because it causes skin friction drag—something which was incalculable before Prandtl's boundary layer concept. The wall shear stress can be changed into a non-dimensional variable called the skin friction coefficient, given by Eq. (2.6) [21].

$$c_f = \frac{\tau_w}{1/2\,\rho U_\infty^2} \tag{2.6}$$

This coefficient can be used to calculate the drag on an object related to skin friction, which is discussed later in this chapter.

Thermal Boundary Layers

Temperature also plays an important role in fluid flows over surfaces, because things tend to heat up whenever friction is involved. If there is a temperature difference between a surface and the fluid moving over it, a thermal boundary layer will develop which is similar to the velocity boundary layer [22]. The thermal boundary layer represents a gradient of temperature which changes from the freestream temperature (T_∞) to the surface temperature (T_s). Like velocity boundary layers, thermal boundary layers increase thickness in the direction of the flow, and the thickness at any location x is called the thermal boundary layer height (δ_T). The temperature of the flow at δ_T is considered to be 99% of the freestream temperature. The temperature inside the boundary layer (T_{BL}) changes as a function of the vertical distance from the surface (z). This concept is illustrated in Figure 2.2.

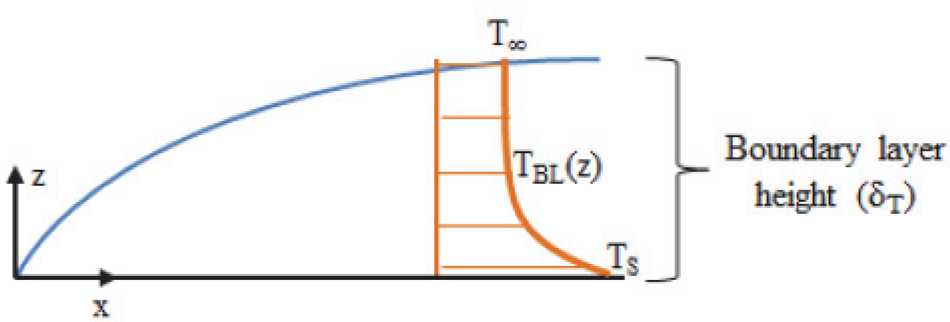

Figure 2.2: Thermal boundary layer development on a flat plate (not to scale) [13]

A flow's thermal boundary layer can be related to its velocity boundary layer using a non-dimensional quantity known as the Prandtl number. The Prandtl number is a ratio of the rates that viscous and thermal information propagate downstream in a flow. This also means that the Prandtl number describes the relative thicknesses of the velocity and thermal boundary layers. The ratio is described by Eq. (2.7) [23]

$$\Pr = \frac{\nu}{\alpha} = \frac{c_p \mu}{k_f} = \frac{\delta}{\delta_T} \tag{2.7}$$

where v is the kinematic viscosity (also known as momentum diffusivity) of the fluid, α is the thermal diffusivity of the fluid, c_p is the specific heat of the fluid, and k_f is the thermal conductivity of the fluid. Flows with Prandtl numbers much greater than one have thicker velocity boundary layers than thermal boundary layers, and the inverse is true for flows with Prandtl numbers much smaller than one.

Heat Concepts

Heat is described as thermal energy interacting at a boundary, and is denoted by the variable Q. There are three types of heat: radiation, conduction, and convection. Radiation is the only form of these heat interactions that does not require a medium and is caused by a temperature differential. Conduction takes place in a medium, whether that be a solid, a liquid, or a gas. Convection may be considered a special form of conduction associated with the flow of energy from one medium into another via a moving fluid [24]. In the present context, convection is used to describe air flowing over a solid surface. When discussing heat, it is helpful to use $\dot{Q}$, which is the rate at which energy flows from one boundary to another. Dividing $\dot{Q}$ by a characteristic surface area yields the surface heat flux term (*q''*).

Black-body Radiation is described by the Stefan-Boltzmann law, given in terms of flux by Eq. (2.8) [24]

$$q''_s = \varepsilon\sigma\,(T_s^4 - T_\infty^4) \tag{2.8}$$

where ε is the emissivity of a surface, σ is the Stefan-Boltzmann constant, T_s is the surface temperature, and T_∞ is the temperature of the freestream fluid. This specific form of the equation models the energy transfer from a surface to the surrounding fluid.

Conduction through solids is described by Fourier's law, given in terms of flux and in one-dimensional form by Eq. (2.9) [24]

$$q'' = -k_s \frac{\partial T}{\partial y} \tag{2.9}$$

where k_s is the thermal conductivity of the solid, and $\frac{\partial T}{\partial y}$ is the one-dimensional temperature gradient within the solid. If the conduction is steady and there is no energy generation within the solid, then the temperature gradient will be linear. This means that Eq. (2.9) can be rewritten to form Eq. (2.10) [24]

$$q'' = -k_s \frac{T_a - T_b}{t} \tag{2.10}$$

where T_a and T_b represent the temperatures at the boundaries of the solid, and t represents the thickness of the solid.

Convection of energy from a solid into a moving fluid is often modeled by Newton's Law of Cooling, given in terms of flux by Eq. (2.11) [24]

$$q'' = -h(T_s - T_\infty) \tag{2.11}$$

where T_s is the surface temperature of the solid, T_∞ is the freestream temperature of the fluid, and h is the convective heat transfer coefficient. The convective heat transfer coefficient is the primary variable defining the rate of energy transfer between a surface and fluid but is often very difficult to obtain. The methods used to obtain this coefficient are explained in the next chapter.

Once a local convective heat transfer coefficient is obtained on a surface, it can be used to calculate the location's Stanton number. A Stanton number is a non-dimensional parameter representing the ratio of the convective heat transfer coefficient to the thermal capacity of a fluid. The local Stanton number is given by Eq. (2.12) [22]

$$St_x = \frac{h}{\rho U_\infty c_p} \tag{2.12}$$

where ρ is the fluid density, U_∞ is the freestream velocity, and c_p is the fluid's specific heat. Stanton numbers are helpful to compare convective heat transfer coefficients across surfaces uncoupled from fluid properties or flow conditions. The local Stanton number is related to the local skin friction coefficient. For forced external convection in air (Pr ≈ 1.0), the Stanton number can be simplified further using what is known as Reynolds' analogy, seen in Eq. (2.14) [23].

$$St_x = \frac{C_{fx}}{2} \tag{2.14}$$

Theoretical Stanton number correlations are used in this study for both laminar and turbulent flow over smooth flat plates. Boundary conditions of constant heat flux and an unheated starting length (ξ) are used. For flows with negligible freestream acceleration, theoretical correlations are given in Eq. (2.15) and Eq. (2.16), respectively. For the accelerated flows used in this study, new theoretical correlations were needed. The theoretical laminar correlation was based on the correction of Smith and Spalding [25] applied to the flat plate expression of Eq. (2.15). The theoretical turbulent correlation was based on the correction of Ambrok [26] applied to the flat plate expression of Eq. (2.16). Both new theoretical correlations, corrected for an unheated starting length, are given in Eq. (2.17) and Eq. (2.18), respectively. In these equations, ζ is a dummy integration variable representing x. For more information, see Shannon [17].

$$\mathrm{St}_{x,\mathrm{laminar,\ no\ xcel}} = \left[1-(\xi/x)^{3/4}\right]^{-1/3} 0.453\,\mathrm{Re}_x^{-1/2}\,\mathrm{Pr}^{-2/3} \tag{2.15}$$

$$\mathrm{St}_{x,\mathrm{turbulent,\ no\ xcel}} = \left[1-(\xi/x)^{9/10}\right]^{-1/9} 0.0308\,\mathrm{Re}_x^{-1/5}\,\mathrm{Pr}^{-2/3} \tag{2.16}$$

$$\mathrm{St}_{x,\mathrm{laminar,\ xcel}} = \left[1-(\xi/x)^{3/4}\right]^{-1/3} \frac{0.453\,\mathrm{Re}_x^{-1/2}\,\mathrm{Pr}^{-2/3}}{\left[\int_0^{\zeta}\left(\frac{U_e(\zeta)}{U_e(x)}\right)^{(2.95\,\mathrm{Pr}^{0.07})-1}\frac{d\zeta}{x}\right]^{\frac{1}{2}}} \tag{2.17}$$

$$\mathrm{St}_{x,\mathrm{turbulent,\ xcel}} = \left[1-(\xi/x)^{9/10}\right]^{-1/9} \frac{0.0308\,\mathrm{Re}_x^{-1/5}\,\mathrm{Pr}^{-2/3}}{\left[\int_0^{\zeta}\left(\frac{U_e(\zeta)}{U_e(x)}\right)\frac{d\zeta}{x}\right]^{\frac{1}{5}}} \tag{2.18}$$

Airfoils

When a fluid flows over an immersed body, the velocity of the fluid changes. Because the body displaces fluid mass, the flow velocity around the body must increase according to the conservation of mass. For air flowing over an airfoil, the body is most often shaped so that air moves faster over the top surface than the bottom. Bernoulli's equation, written in the mid-1700s (well before Prandtl's time), is given in Eq. (2.19) [21].

$$\frac{P}{\rho g}+\frac{V^2}{2g}=\text{constant} \tag{2.19}$$

This equation shows that if velocity increases along a streamline, the pressure must decrease proportionally. Decreasing pressure along an airfoil is known as a favorable pressure gradient. However, the pressure will eventually reach a minimum value and begin to increase again, which is known as an adverse pressure gradient. An illustration of these concepts is shown in Figure 2.3.

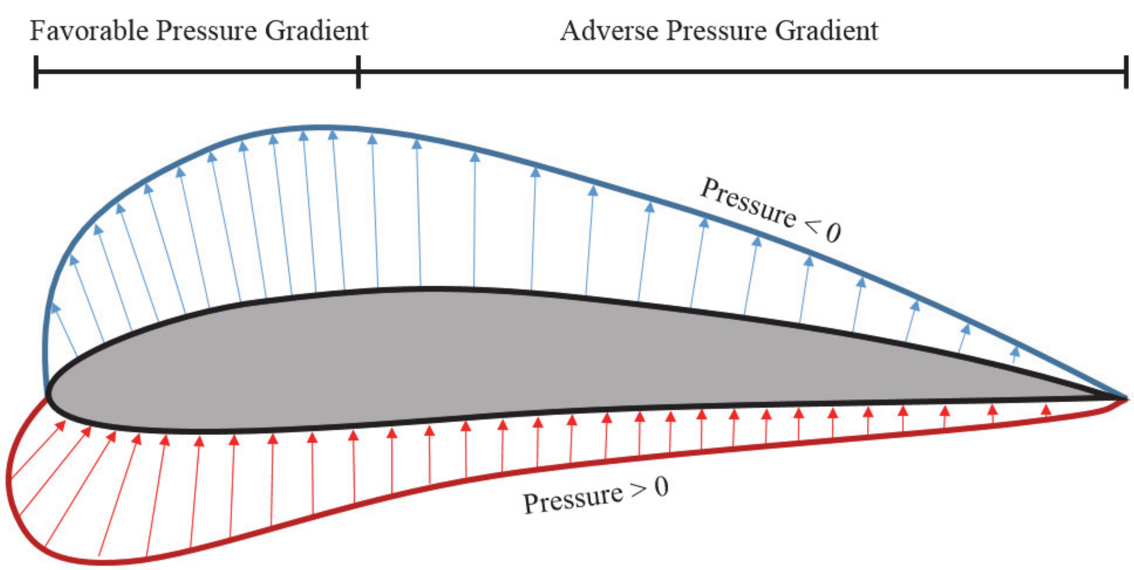

Figure 2.3: Surface pressure distribution on an airfoil

When pressure on the front of an airfoil is greater than pressure on the back, the airfoil experiences pressure drag. Aerodynamicists have been able to approximate pressure drag since the beginning of the 1900s [20]. However, pressure drag is only one part of the total drag that an airfoil experiences. The other part is skin friction drag, which arises from shear stresses caused by viscous flow over the surface. From Eq. (2.5) and Newton's shear stress law, recall that shear stress is proportional to the velocity gradient. High speeds mean high shear stress. From the differential version of Bernoulli's equation, the velocity gradient must be opposite in sign to the pressure gradient. Low pressure means high speeds, but increasing pressure (an adverse pressure gradient) means decreasing speeds. Eventually, an adverse pressure gradient can slow the fluid momentum enough so that it separates from the airfoil surface, creating a wake of dead air. The separation point occurs when the velocity gradient is zero at the wall. These concepts are illustrated in Figure 2.4.

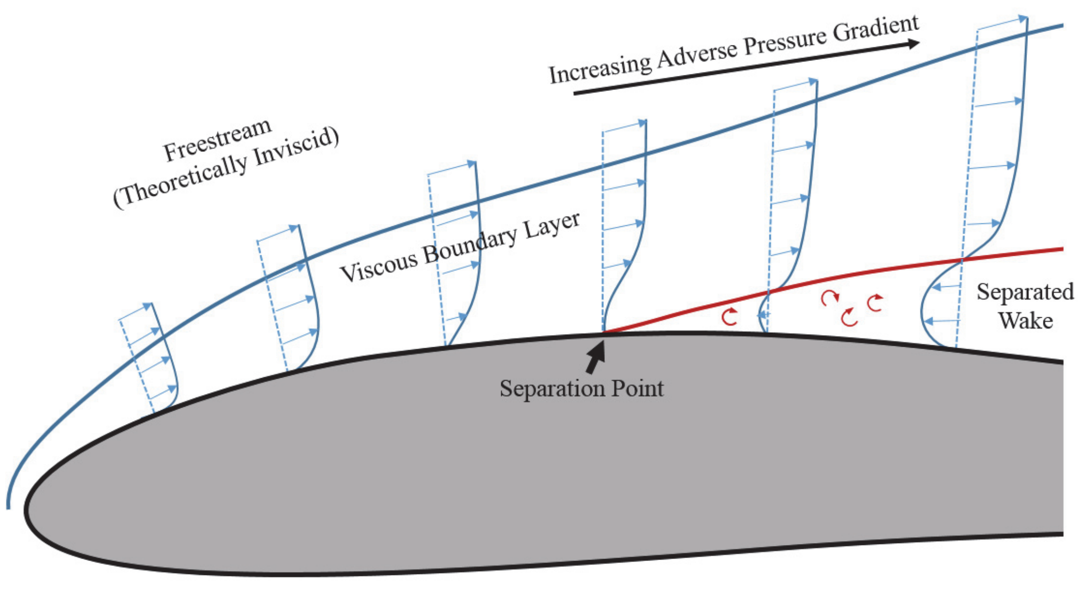

Figure 2.4: Boundary layer separation process (not to scale)

One of the main objectives of modern analytical fluids is to evaluate total drag on a body—both pressure drag and skin friction drag. In theory, this is as simple as calculating the components of force on the surface of an object in the direction of the upstream velocity, as shown in Eq. (2.20) [21].

$$D = \int dF_x = \int \left(p\cos\theta + \tau_w \sin\theta \right) dA \tag{2.20}$$

In this equation, the pressure (p) term represents the pressure drag, and the shear (τ_w) term represents the skin friction drag at the wall. Since pressure drag is much easier to experimentally determine than skin friction, modern aerodynamicists have spent more effort designing ways to model shear forces on bodies.

Often, drag is modeled with a non-dimensional coefficient, which makes it useful when designing scale models. The coefficient of drag is composed of two non-dimensional components: the pressure drag coefficient and the friction drag coefficient, as shown in Eq. (2.21) [21].

$$C_D = C_{D_p} + C_{D_f} \tag{2.21}$$

Each individual drag coefficient is made up of different models for the pressure coefficient and the coefficient of friction. For instance, the global pressure drag coefficient is most often modeled as shown in Eq. (2.22) [21]

$$C_{D_p} = \frac{\int C_p \cos\theta dA}{A} \tag{2.22}$$

where the local pressure coefficient is given in Eq. (2.23).

$$C_{p_x} = \frac{p - p_\infty}{1/2\, \rho U_\infty^2} \tag{2.23}$$

Unfortunately, an equation for C_{D_f} is not as easily given. The friction drag coefficient is often a function of Reynolds number and relative surface roughness, and has only been determined experimentally thanks to Prandtl's boundary layer concept. However, the global friction drag coefficient is almost always found in terms of the local skin friction coefficient (seen previously with respect to the Stanton number in Eqs. (2.13) and (2.14)), which is given below in Eq. (2.24) [21].

$$C_{f\,x} = \frac{\tau_w}{1/2\,\rho U_\infty^2} \tag{2.24}$$

For turbulent flows, inertial forces will often be much larger than viscous forces, and the pressure difference in the numerator of the pressure coefficient will scale with the dynamic pressure in the denominator. In these cases, the pressure coefficient will scale independently from the Reynolds number, and the drag coefficient is only slightly influenced by the Reynolds number. However, for flows with very small Reynolds numbers, viscous forces are much more significant, and Reynolds number holds more influence. General experimental relationships for the coefficient of drag in both turbulent and laminar flows are shown in Eq. (2.25) and Eq. (2.26) respectively [21].

$$C_{D_{turbulent}} \approx \frac{0.072}{\sqrt[5]{\mathrm{Re}_x}} \tag{2.25}$$

$$C_{D_{laminar}} \approx \frac{1.328}{\sqrt{\mathrm{Re}_x}} \tag{2.26}$$

Airfoils are relatively simple to construct and test in a wind tunnel, especially if only pressure and velocity data are desired. However, measuring skin friction on a curved surface is more difficult, and if convective heat transfer coefficient data is desired, the wiring and instrumentation for heaters becomes quite complex. Therefore, many heat transfer experiments are performed on flat plates rather than airfoils for ease of instrumental setup. As long as the flow has the same acceleration profile as the airfoil would induce, the experimental difference is negligible. Additionally, flat plate experiments are ubiquitous among aerodynamicists which simplifies the comparison and validation of data.

Surface Roughness Models

Airflow over smooth surfaces is a good starting place for flow studies, but real surfaces frequently have some form of roughness which affects the flow. As early as 1914, ten years after Prandtl's Boundary Layer presentation, Richard von Mises was the first to suggest a variable for the absolute roughness of a surface, which he then converted into a non-dimensional "relative roughness" ratio [27]. He related relative roughness and Reynolds number to a friction factor he used to characterize pipe flows. In 1933, Johann Nikuradse further quantified pipe flows by running extensive tests in pipes of different relative roughnesses. Nikuradse used sand lacquered to the inside surfaces of pipes to artificially build up roughness. He carefully sifted sand grains of different sizes to achieve different relative roughnesses [28]. In 1936, Hermann Schlichting followed this same "sand-grain equivalent roughness" methodology to perform further extensive testing on artificially roughened flat plates [29]. The results of both Nukuradse's and Schlichting's work showed that for low Reynolds number flows, the viscous sublayer region was thick enough that the roughness was fully enveloped in it, thereby not disturbing the rest of the boundary layer. However, high Reynolds number flows (i.e., high turbulence flows) compressed the boundary layer thickness such that roughness elements protruded through the viscous sublayer and created additional skin friction due to enhanced turbulent shear stress [29]. The theory behind the sand-grain equivalent roughness model was that any surface roughness could be modeled using an equivalent sand-grain size, k_s. The sand-grain equivalent model matches skin friction values very well, but is unable to account for material conductivity differences. As such, the model must be modified to predict heat transfer. Even so, it has been used in numerous studies over the years, with efforts centered on determining skin friction and heat transfer enhancement (compared to smooth surfaces). Some findings showed that roughness can enhance skin friction from 1.5x to 3.5x, and Stanton number from 1.1x to 1.6x [30,31].

Schlichting also proposed an alternate model, known as the discrete element model (DEM) [29]. This model discretizes roughness as the sum of individual roughness elements. The total drag on a rough surface is made up of the pressure drag from each individual roughness element, and the skin friction drag on the flat part of the surface. The DEM is a spatially averaged model in the directions parallel to the surface wall, so it is not fully resolved across the entire roughness span. However, the DEM has been extended to handle heat transfer by concluding that the total flux from a rough surface is the sum of the heat transfer from each individual roughness element and the heat transfer from the flat part of the surface. In this way, the DEM incorporates important aspects of fluid physics, and models realistic temperature changes inside roughness elements themselves. This is a distinct advantage over the sand-grain equivalent roughness model, even though the DEM is spatially averaged [32]. Furthermore, McClain et al. [33] proposed to improve the DEM by treating individual roughness elements as extended surfaces (i.e. fins). Each element is analyzed with respect to convection, conduction, and radiation along the entire protrusion, and material conductivity is taken into account. This improvement is known as the extended surface discrete element model (ES-DEM).

Surface roughness has also been modeled using grid-resolved computational simulations. Computational simulations of flows over roughness require adaptive grids for at least three different length scales which are each important in their own right. First, there is the largest scale, which is the length of the model. Then there is the much smaller scale for the roughness elements, which can be three or four orders of magnitude less than the length of the model. An even smaller scale must capture the thickness of the viscous sublayer, which can be five or six orders of magnitude less than the length of the model [34]. These adaptive grids require an enormous number of points. The grid-resolved simulations run by Bons et al. showed better agreement with previous experimental trials than the DEM, but required more computational time by an increase of two or three orders of magnitude [35].

Surface Roughness Measurement

Some of the earliest techniques for recording ice shapes are described by Reehorst and Richter [36]. Simple 2D tracings could be made by hand of the ice growth profile. First, a heated wire or aluminum block would be pressed against the ice, melting a slot. A cardboard square cut to fit the airfoil profile would be inserted into the slot, and a pencil is used to trace the ice shape onto the cardboard [37,38], as seen in Figure 2.5. To make 3D casts, ice accretions were dipped into molten beeswax multiple times to build up layers of wax, which was then opened to drain the remains of the ice. The wax mold could then be filled with some type of casting plaster, left to harden, and then the wax would be melted away leaving the final cast. [36]. In 1978, Wilder [39] took ice structures grown on airfoils in the IRT at set icing conditions and made plastic casts with current molding techniques, which he then used to draw correlations about ice accretion.

During the winters of 1982-83 and 83-84, Lee et al. [37], Hanson and Lee [40], and Lee et al. [41] all used similar techniques to record ice shapes accreted on the main rotor of a UH-1H Helicopter, which has a NACA 0012 profile [41]. The helicopter would hover several feet off the ground while another helicopter sprayed the UH-1H main rotor with water until sufficient ice had accreted. The UH-1H then landed, one of the rotor blades was removed and taken to a below-freezing temperature controlled van, and placed in plywood boxes. Dow-Corning silicon rubber was then used to create a mold of the ice accretions on the rotor. Epoxy castings could then be made from the molds and tested in the Fluidyne Engineering Coproration's wind tunnel [37,40,41]. Similar mold and casting methods continued to be used over the next several decades, with improvements on the materials and methodology [42,43,44].

Figure 2.5: Hand tracing an ice accretion profile [19]

Of course, these methods for reproducing ice formations all have drawbacks. Ice accretions, especially those which have only been allowed to accrete for a short time, frequently have very fine surface texture. If the ice is allowed to melt at all, details of the surface may be lost. 2D ice profile tracings require hot tools to melt a slot for the cardboard, which is destructive and affects the very profile that will be measured [38]. Creating a 3D mold using hot wax or an exothermically curing material will undoubtedly alter the ice accretion. All molding materials must instead be kept below freezing temperatures at all times, and the curing process must use specific compounds or techniques to ensure it won't be exothermic. Additionally, many casting materials are either too coarse to capture all surface texture, or are toxic and must be handled with safety tools. Some casting materials are brittle, and may break or be damaged while being removed from the mold [36]. Furthermore, tracing accretion profiles by hand tends to be very inaccurate, and identical shapes traced by two different people usually show discrepancies of several millimeters [38].

Ice accretions were first filmed and photographed at the NASA Glenn Research Center in 1986 by Olsen and Walker [4], but their photographs only provided qualitative data linked with 2D profile tracings and measurements. In 1994, basic quantitative photography techniques were used by Shin [45] to obtain non-destructive measurements of ice accretions. However Shin only used one camera to take plan view and profile view images of accretions. A ruler for scale was included in the photographs, and software was used to obtain the diameters and heights of roughness elements. This method was reproduced by Anderson et al. [46], although they admitted the method was fairly subjective. The plan view photographs had to be calibrated due to the airfoil curving away from the lens of the camera. Moreover, other subjective factors such as the location of roughness element edges or which small features to include as roughness elements were difficult to define.

Modern-day quantitative photography techniques have advanced enough to create detailed digital 3D surfaces, but the process requires multiple cameras or camera angles, static grid calibration, careful methodology, and complicated data reduction [19]. Instead of using photography, another non-destructive measurement technique which has been used involves lasers. One such method was developed in 1995 by Hovenac and Vargas [38] at NASA Lewis to accurately measure the thickness and profile of ice accretions. A laser line was projected onto the ice shape, and cameras were used to capture the light scattered by the ice. The method corrected for camera angle distortions, and resulted in a profile which showed good accuracy when compared with hand-drawn trials. More recently, Lee et al. [19] evaluated several commercial laser scanners which can record fully 3D ice accretion surfaces, and set up selection criteria to choose an option for further use. For the laser scanners to work properly, the ice accretions had to be painted with highly-reflective, diffuse, white paint, applied with an airbrush. Each laser scanner gathered point cloud data with a maximum resolution of 0.002” per scan line. The point cloud data had to be post-processed, but resulted in a highly resolved surface, as can be seen in Figure 2.6.

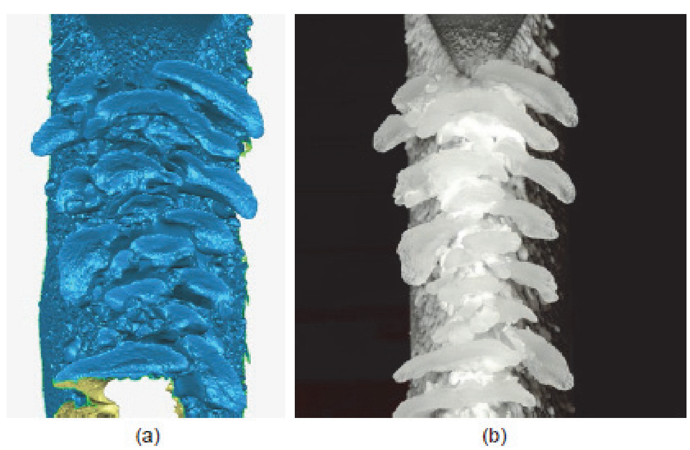

Figure 2.6: Ice accretion captured via (a) laser scan, and (b) photograph [19]

The accuracy of 3D ice accretion simulations generated from laser scan data was later validated by Broeren et al. [47]. Six ice accretion cases were first laser-scanned, and then a mold was made to create polyurethane casts. The laser scanned surfaces were used to fabricate ice shapes using rapid-prototype manufacturing (3D printing), and then aerodynamic tests were performed on each ice shape. Overall, there was excellent agreement between the two methods, with typical differences in maximum lift coefficients being less than 3%, and differences in stall angles of less than 1° [47].

Aircraft Icing

Terminology

Ice accretion on aircraft surfaces refers to the gradual buildup of layers of frozen water. Both water droplets and ice particles can impinge onto aircraft surfaces, although ice particles tend to ricochet off whereas water droplets can often adhere and freeze. The Federal Aviation Administration (FAA) defines two main parameters which describe hazardous icing conditions in clouds: liquid water content (LWC), and median volumetric diameter (MVD). LWC is the mass per unit volume of water in air, and the MVD represents a typical water droplet diameter a cloud where half the droplets are larger and half the droplets are smaller. The FAA notes that a cloud's LWC is proportional to how fast ice will accumulate, and MVD is proportional to the extent of icing [48].

The FAA also regulates how aircraft must be built or operated in compliance to airworthiness specifications. Since 1964, Appendix C of the Aeronautics and Space section of the U.S. Code of Federal Regulations has defined a set of icing conditions which aid in the design of ice-protection systems on aircraft. Variables such as LWC, MVD, temperature, altitude, and horizontal cloud extent are all used to estimate maximum ice accretion levels on unprotected surfaces. To be certified for flight in icing conditions, an aircraft must show compliance with Appendix C [8] regulations.

Further, in 2014, Appendix O was added to the Aeronautics and Space Section of the U.S. Code of Federal Regulations. Even if an aircraft is not intended for flight in all icing conditions, it must be certified to meet the requirements outlined in Appendix O, either to fly safely through, or to exit safely at the very least. Appendix O conditions are defined as "freezing rain" with supercooled large droplets (SLD) in or below stratiform clouds. Small aircraft with a takeoff weight less than 60,000 lbs. or with reversible flight controls must be able to detect and safely fly in Appendix O icing conditions in order to be certified [9].

Depending on the atmospheric conditions during an aircraft's flight, there are two classifications of ice which can form: glaze ice and rime ice. Glaze ice, also known as clear ice, is formed very slowly in temperatures which are close to freezing (32ºF). Only a fraction of impinging water droplets freeze immediately, and the rest form a thin film liquid layer which runs downstream along the surface until it freezes. It is hypothesized that the thin film liquid layer, while mostly smooth, might be slightly rough enough to trip incoming laminar airflow into turbulence. Large accretions of glaze ice can even form "horns", which can especially disrupt incoming airflow. Glaze ice is dense, hard, often transparent, and relatively difficult to remove [48]. See Figure 2.7 for examples of glaze ice.

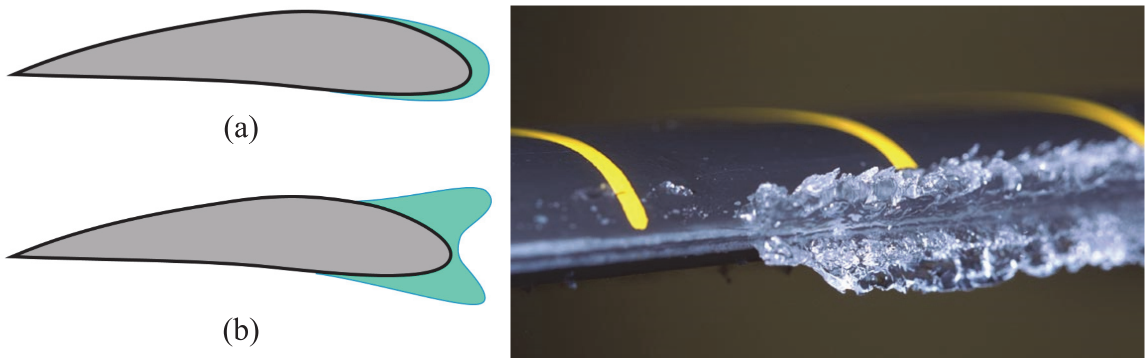

(a) (b) (c) [49]

Figure 2.7: Glaze ice (a) without horns, (b) with horns, and (c) photo of glaze ice with horns in a test environment

Rime ice occurs in temperatures much colder than freezing, typically around 0ºF. Because of the lower temperatures, every impinging droplet freezes directly on impact, leading to a much rougher accretion. Little pockets of air are left between the droplets, making rime ice opaque, porous, and brittle [48]. See Figure 2.8 for an example of rime ice.

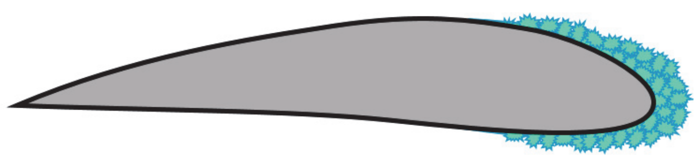

Figure 2.8: Rime ice on an airfoil

Ice Accretion Process

As was stated previously, Olsen and Walker [4] were the first to photograph and film the ice accretion process at the NASA Glenn Research Center in 1986 [50]. Although there were ice accretion models prior to their work, their studies changed the modern understanding of ice formation on airfoils. They used a high speed video camera to film the icing process on an airfoil mounted inside NASA Glenn's Icing Research

Tunnel (IRT). They found that as supercooled water droplets impinge on an airfoil, a fraction of them coalesce with one another into a thin film. As the thin film drops get large enough, aerodynamic drag eventually overcomes the surface tension keeping the drops stationary, and they are pulled downstream along the airfoil surface. The liquid thin film drops move aft until they freeze, becoming a layer of glaze ice.

As the liquid thin film droplets freeze, they undergo a phase change which is bounded by the Stefan Condition. This boundary condition means that the phase change must occur at an essentially constant temperature (0°C), and that the underlying surface must also exhibit this near-isothermal nature. The freezing process is exothermic, and energy must be transferred out of the liquid thin film layer. Ice acts as an insulator, and therefore the dominant modes by which energy leaves the liquid thin film layer are by convection and evaporative cooling into the airflow [51]. The frozen water beads form a zone of ice roughness which has significantly more surface roughness than the liquid thin film layer [49].

Ice roughness disturbs the boundary layer development on the surface, as well as increases the skin friction and convective heat transfer. This is because, even for ice roughness with as little as two minutes of exposure time, the surface roughness elements protrude well out of the boundary layer, causing enhanced convection [45]. Horned glaze ice, feathers, or rime ice shapes are all primarily caused by ice roughness which protrudes from the surface enough to affect the local airflow and have a larger surface area to collect more drops. However, these observations are not universal, and the icing process changes slightly depending on variables such as air properties, wing sweep, angle of attack, etc. For a sketch of ice accretion on a symmetric airfoil at zero angle of attack and no sweep, see Figure 2.9.

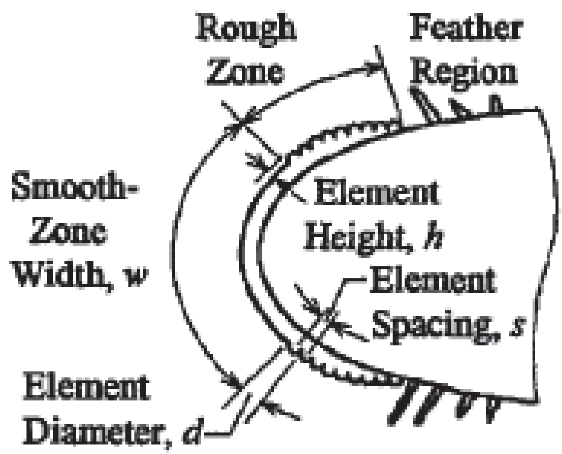

Figure 2.9: Early stage glaze ice accretion on airfoil leading edge [50]

Modeling Ice Accretion

The foundational model for aircraft icing was developed in 1953 by Messinger [52], and it is still in use today. Messinger's model used an energy balance at an unheated surface in icing conditions. Energy input is defined as a combination of the latent heat from fusion, frictional heating in the boundary layer, and the kinetic energy of impinging droplets. Energy losses were defined by the combination of convection, sublimation/evaporation (temperature dependent), and impinging supercooled droplets absorbing energy. All of these factors play a role in heat transfer, although convection is the most significant [51]. Figure 2.10 shows Messinger's model of the factors at work in heat transfer on an unheated airfoil.

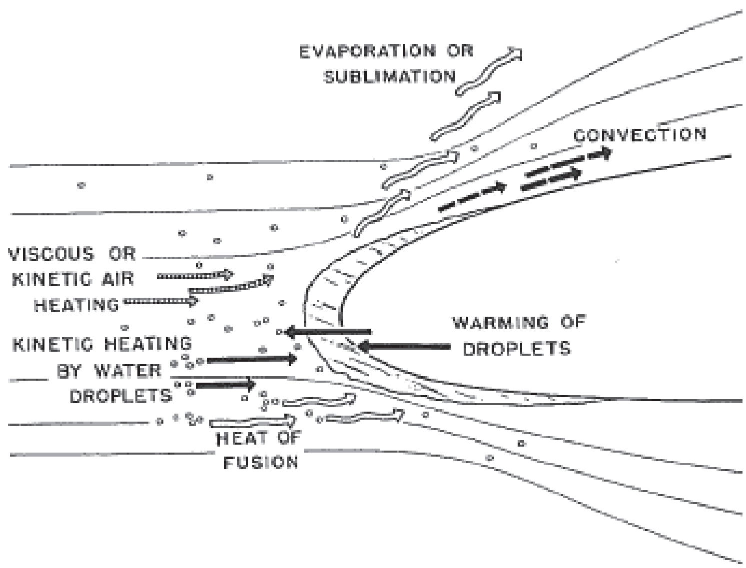

Figure 2.10: Modes of energy transfer for an unheated airfoil in icing conditions [52]

Messinger also noticed that not all impinging droplets freeze on impact, depending on the air properties. He introduced a new variable called the freezing fraction, which is the non-dimensional ratio of the number of droplets that freeze immediately upon impingement versus the total number of droplets. As such, this ratio is only a value from zero to one, with zero representing no droplets freezing on impact [52]. Rime ice forms when the freezing fraction is one, and any value less than one allows glaze ice to form. Messinger believed that when the freezing fraction was less than one, there would be a thin-film liquid layer continuously flowing over the ice surface. However, this was shown to be incorrect by Olsen and Walker [4].

Although the Messinger model is over 60 years old, it remains relevant, and his energy balance and freezing fraction concept have been modified for use in NASA's Lewis Ice Accretion Code, known as LEWICE. Additionally, LEWICE uses the sand-grain equivalent roughness model from Nukuradse [28] and Schlichting [29] to determine roughness heights [11]. The energy balance used by LEWICE is shown in Eq. (2.27) [11]

$$-\left(k_{\omega}\frac{\partial T}{\partial \varphi}\right)_{\varphi=0} = q''_{nc} + q''_{evap} - q''_{ke} - q''_{lat} \pm q''_{sens} \tag{2.27}$$

where k_{ω} is the thermal conductivity of the icing surface, $\frac{\partial T}{\partial \varphi}$ is the surface temperature distribution, and the q" terms are the net heat gains and losses from Messinger's model. The equivalent sand-grain roughness height is determined using the empirical correlation seen in Eq. (2.28) [11]

$$x_k = \frac{1}{2}\sqrt{0.15 + \frac{0.3}{N_{f,stag}}} \tag{2.28}$$

where $N_{f,stag}$ is the freezing fraction at the stagnation point. This equation is used for all icing conditions. There are many other equations incorporated into the LEWICE code, including models to find the convective heat transfer coefficient, the skin friction coefficient, and the mass flux of runback water on the surface.

The equations used in LEWICE are helpful, but many are overly simplistic and built on fundamentally flawed ideas. For example, the sand-grain equivalent roughness model is based on matching skin friction values and doesn't account for convective heat transfer effects [30, 31]. Furthermore, in 1994, Shin [45] used the IRT at NASA Glenn to grow ice accretions on an airfoil, which he then compared to the LEWICE sand-grain roughness predictions in matching conditions. He concluded that real ice accretions differ from sand-grain roughness in both size and distribution density. By varying icing parameters such as airspeed, temperature, and LWC, he showed that LEWICE is a poor predictor of realistic ice roughness trends [45]. Some of these results are shown in Figure 2.11.

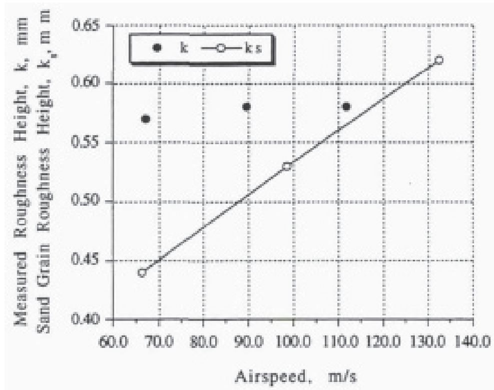

(a)

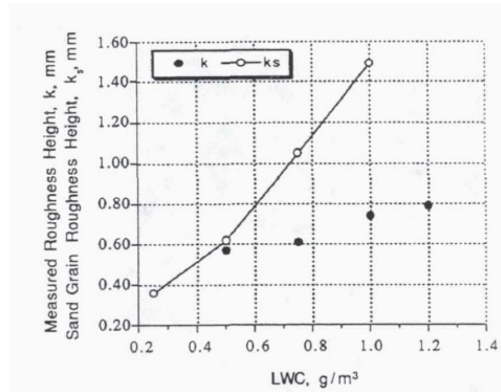

(b)

Figure 2.11: Comparison of measured roughness height *k* with the LEWICE predicted sand-grain roughness height k_s by varying (a) airspeed and (b) LWC [45]

Other studies have also shown that LEWICE handles liquid water runback poorly. When temperatures are well below freezing, LEWICE can predict ice accretions fairly well because each droplet freezes instantaneously and creates rime ice [5, 45]. However, mild freezing conditions mean droplets may run back and create glaze ice, which adds complexity due to the three-phase condition at the icing surface. Glaze ice also develops larger roughness elements than rime ice, enhancing the convective heat transfer. LEWICE can make approximate predictions of glaze ice shapes using Messinger's energy balance, but these predictions have been shown to frequently be inaccurate [5, 53].

Historical Investigations of Ice Accretion

Over the years, many researchers have sought to improve the current models of ice accretion. Much of the work has centered on determining skin friction and heat transfer enhancement using simulated ice accretions. The works of Schlichting [29] and Nikuradse [28] are still the most referenced and well-known data sets on rough surface effects in turbulent flow since the 1930s. However, in 1984, Coleman et al. [54]

presented a re-evaluation of Schlichting's roughness experiment. The study noted that Schlichting simplified his calculations by assuming that smooth surfaces in his tests had negligible shear stresses, and that the wall shift used in the calculation of roughness element volume was the same as the wall shift used in the velocity profile method of determining wall shear [54]. Coleman et al. recreated Schlichting's experiment using more precise assumptions and found that the original coefficients over-predicted skin friction coefficients by values ranging from 0.5 to 73 percent [54].

Van Fossen et al. [55] used the NASA Lewis IRT to investigate how surface roughness and freestream turbulence affects heat transfer. Ice structures were grown on a cylinder, cast in a mold, and then heated to obtain heat transfer coefficients. Their results showed that heat transfer increases due to boundary layer growth over surface roughness. Poinsatte et al. [51] recognized the importance that local convective heat transfer coefficients h have on ice accretion, and in 1990 performed a set of experiments to investigate how h is affected by surface roughness. Roughness was simulated using 2 mm diameter hemispheres attached to 21" chord NACA 0012 airfoils in four distinct patterns, similar to patterns used by Schlichting [29], as shown in Figure 2.12.

The airfoils with simulated surface roughness created by Poinsatte et al. [51] were tested both in the NASA Lewis Twin Otter Icing Research Aircraft and also in the NASA Lewis IRT. These airfoils were tested at various aircraft speeds, angles of attack, and simulated weather conditions. The tests performed in the research aircraft exhibited the same trends as those performed in the IRT. The leading edge roughness shown in Figure 2.10 (a) increased stagnation point heat transfer by roughly 10%, but did not significantly affect the heat transfer downstream.

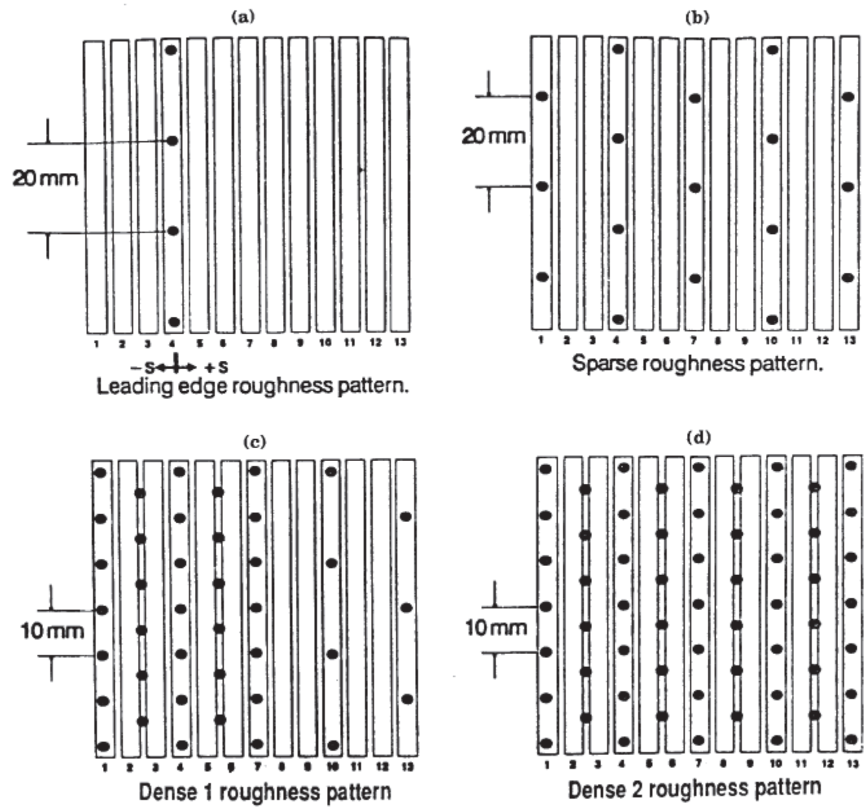

Figure 2.12: Ordered roughness distributions used by Poinsatte et al. [51]

The roughness cases in Figure 2.12 (b), (c), and (d) however, drastically increased the heat transfer compared to smooth surfaces. Their results also showed that increasing the density of the roughness elements yielded much higher heat transfer than the results from the sparsely placed elements. Poinsatte et al. also concluded that surface roughness magnified the effect that turbulence has of increasing heat transfer on a surface [51].

Bragg et al. [56, 49] continued the investigations into how surface roughness affects heat transfer, but focused specifically on leading edge roughness of 21” chord NACA 0012 airfoils. These experiments used systematically placed hemispheres much smaller than those used by Poinsatte et al. [51], sized at 0.5 mm [56] and a combination of 0.35 mm and 0.75 mm [49], respectively. Bragg et al. used IR heat lamps and an IR camera to measure local convective heat transfer coefficients [56], hot-wire anemometry to make velocity measurements, and fluorescent oil and a camera system to perform flow visualization [56]. Their results of convective heat transfer enhancement compared to a smooth surface can be seen in Figure 2.13, although the roughness model used in their experiments is organized systematically, not akin to realistic ice roughness.

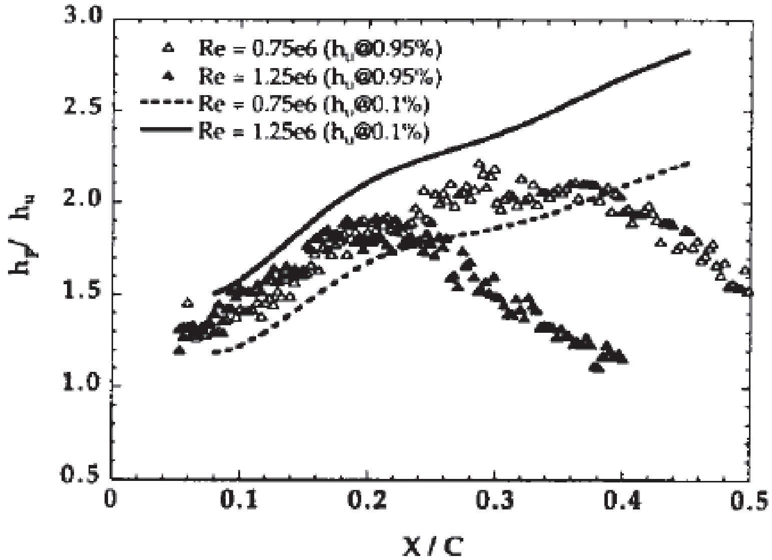

Figure 2.13: Heat transfer enhancement with varying freestream turbulence [49]

Flows with variable pressure gradients have also been studied by multiple researchers, usually in an effort to compare flat plate tests to airfoil tests. Coleman et al. [57] used a surface with roughness modeled by systematically placed densely packed spheres, and compared measured Stanton numbers in two flows. One flow had constant freestream acceleration, and the other began at the same freestream velocity as the first, but was followed by an accelerated zone (a favorable pressure gradient). Depending on the Reynolds number, their results showed that the favorable pressure gradient increased the measured Stanton number by 10-20% compared to the flow with negligible acceleration [57]. Chakroun and Taylor [58] performed a similar experiment using hemispheres for roughness elements instead of spheres, and found that the favorable pressure gradient again increased the measured Stanton number by 5-15% [58] compared to the flow with negligible acceleration. Turner et al. [59] followed suit with a similar study using elements shaped like pyramids and trapezoids of three different heights. Their results showed that favorable pressure gradients increased measured Stanton numbers by 2-3% compared to the flow with negligible acceleration. They also reported that their pyramidal elements showed heat transfer enhancement over 70% greater than previous spherical studies, although they admitted that their CFD code used for comparison tended to over-predict heat transfer rates by up to 10% [59].

In contrast to the studies done with simulated roughness placed systematically over a surface, much research has been done to capture and study real ice roughness. Many of the methods used to create profile drawings and molded castings of ice accretions were discussed earlier in this chapter. Ice accretions grown in wind tunnels were validated against ice accretions grown on helicopter rotors [37,40,41] or on airfoils extended from aircraft flying in icy weather [60]. Henry et al. [61] performed a study to characterize how ice roughness influences aerodynamic performance, and the ice shapes they used were simulated with different sandpaper grits. Protuberances were added to simulate larger ice feathers, but these surfaces were still simplified simulations [61]. In 2001, Bons et al. [62] used a linear contact stylus profilometer system to capture real turbine-blade surface roughness in a grid pattern on 25 different turbine blades. Once these grids were captured, they were converted into digital surfaces using a least-squares surface fit. Bons [31] then created six flat-plate “realistic” roughness models from these digital surfaces, which had been scaled for wind tunnel testing. Using these realistic roughness patterns allowed diverse element interaction to be captured in boundary layer and heat transfer tests, rather than the biased results found by using simplistic simulated patterns. The tests performed by Bons [31] showed St enhancement by factors of 1.1-1.5, and Cf enhancements by factors of 1.3-3.0 when compared to smooth surface results. Additionally, Bons and McClain [30] compared realistic roughness surfaces to simulated roughness surfaces in different pressure gradients. Compared to flows with negligible acceleration, the flows with favorable pressure gradients showed increased Stanton numbers. The simulated roughness surfaces showed increases of 7%, whereas the realistic roughness surfaces showed increases of up to 18%.

A series of experiments performed by Dukhan et al. [63] further confirmed the importance of realistic surface roughness tests. Investment casting was used to create two aluminum models from real ice accretions, shown below in Figure 2.14. These models were instrumented with thermofoil heaters and heat-flux gauges and used to gather heat transfer data [63]. The heat transfer values recorded were much higher than those found using ordered arrays of roughness elements like those found by Poinsatte et al. [51]. Han and Palacios [44] also used castings in a realistic ice roughness study to compare against NASA's LEWICE accretion code, and found that LEWICE over-predicted heat transfer coefficient values by 200% to 391% [44].

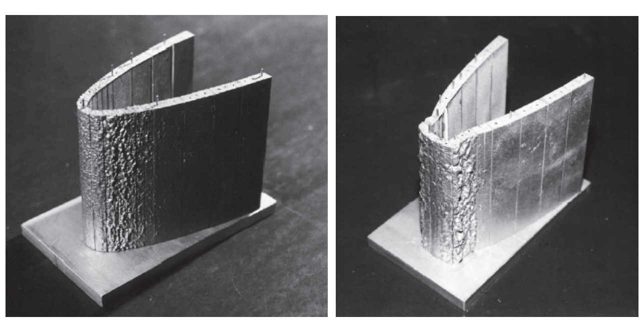

Figure 2.14: Aluminum castings of glaze ice accretions on a NACA 0012 airfoil [63]

In 2010, Croce et al. [64] developed a Lagrangian technique of roughness evaluation used by the FENSAP-ICE accretion code. Individual impinging droplets on airfoils were tracked in order to model the physics of realistic droplet coalescence patterns. A Lagrangian technique similar to that used by Croce et al. [64] was developed by Tecson and McClain [65,66] to generate simulated Appendix C roughness distributions. These patterns were originally used to match the roughness characteristics of the surfaces quantitatively photographed and studied by Shin [45] and Anderson et al. [46]. A solid model of the resulting surface (labeled 052996.04 to represent date and run number) is shown in Figure 2.15. Versions of this surface were studied in flows with negligible freestream acceleration by Tecson [13], as well as with imposed flux boundary conditions by Walker et al. [67].

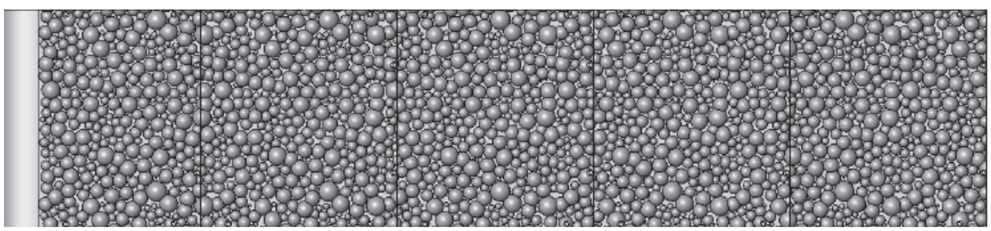

Figure 2.15: Surface model of 052996.04_x10 [13]

In 2011, McClain et al. [68] developed a new method to characterize laser scans of ice accretion surfaces using Self-Organizing Maps (SOM). This iterative neural network method used codebook vectors to represent 3D clumps of point cloud data. Codebook vectors are daisy-chained together with linear connections which follow the trends of clumps of data. In this way, the significant trends of 3D laser scanned surfaces could be captured in a 2D space. This method was further developed by McClain and Kreeger [15] by unwrapping the codebook vector chain links from around a known airfoil geometry. The local 99.9% roughness maximum height (RMH) based on a Gaussian distribution was then evaluated at each codebook vector using Eq. (2.29) [15].

$$RMH_{\mathbf{b}^{\mathbf{n}}} = 3.09R_q == 3.09\left[\frac{1}{J}\sum_{j=1}^{J} N_{\mathbf{x}^j}{}^2\right]^{\frac{1}{2}} \tag{2.29}$$

In this equation, R_q is the root-mean-square roughness height for a rough surface, J is the number of surface points for which $\mathbf{b}^{\mathbf{n}}$ is the closest codebook vector. The salient trends of ice accretions can then be reproduced on a flat surface. An X-Y projection of the SOM method applied to the laser scanned surface used in this study (designated 113012.04) is shown in Figure 2.16. An unwrapped RMH representation of the same roughness with respect to S-distance around the airfoil manifold is shown in Figure 2.17

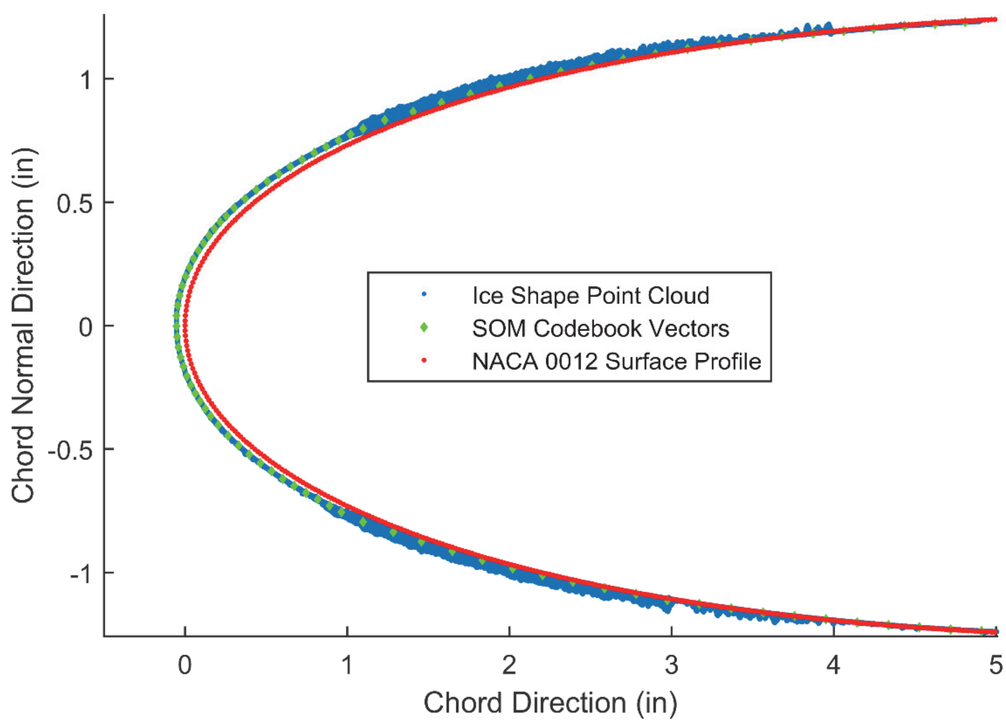

Figure 2.16: Self-Organized Map of 113012.04

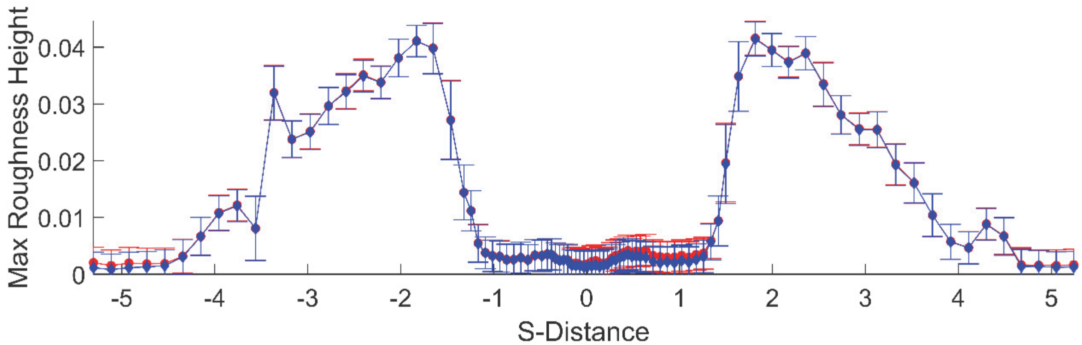

Figure 2.17: Unwrapped RMH representation of 113012.04

The Lagrangian droplet surfaces developed by Tecson and McClain [65,66] were based on the historical perspective on constant roughness properties from the Appendix C work done by Shin [45] and Anderson et al. [46]. However, these historical studies were performed using photographic image analysis. Laser-scanning technology has matured to the point where detailed measurement of ice roughness is now possible.

In addition to the drastic changes in roughness measurement technology, modern FAA regulations regarding Appendix O icing conditions warranted new ice accretion studies so that aircraft can be designed to meet the new standards. As mentioned previously, Appendix O conditions are defined by supercooled large droplets (SLD). McClain et al. [15] used a laser scanning system to record ice accretions which were formed in Appendix O (SLD) conditions. A similar study by McClain et al. [16] used the same laser scanning system to record ice accretions formed on 21” NACA 0012 airfoil in Appendix C conditions. Table 2.1 lists the airflow and cloud characteristics used in the roughness generation of both the 113012.04 case and the 052996.04 case (names based on date and run number) from Anderson et al. [46]. The table also lists A_c, the accumulation parameter defined by Eq. (2.30), where r_a is the leading-edge radius of curvature of the NACA 0012 airfoil, and ρ_{ice} is the density of ice at the freestream temperature [17].

$$A_c = \frac{LWC \cdot V \cdot \Delta t_s}{2 \cdot r_a \cdot \rho_{ice}} \tag{2.30}$$

Table 2.1: Airflow and cloud characteristics used to generate case roughness data [17]

Case Identifier	T (°C)	V (m/s)	MVD (μm)	LWC (gm/m^3)	Δt_s (s)	A_c	Freezing Fraction
052996.04 [46]	-4.2	66.7	29.7	0.6	94	0.245	0.217
113012.04 [16]	-2.4	66.7	150.0	0.6	75	0.195	0.217

The results from the Appendix O conditions investigation revealed that the smooth-to-rough transition does not occur as abruptly as had been historically thought. Instead, the smooth glaze ice gradually transitions to roughness, and then roughness slowly decays downstream [16]. Both investigations scanned multiple accretions at intervals, generating scanned models showing how the accretions changed over time. Using the SOM method developed by McClain et al. [68] and McClain and Kreeger [15], both Appendix O and Appendix C scans were evaluated to characterize the trends associated with the ice accretions. The resulting unwrapped RMH roughness trends are presented in Figure 2.18 and Figure 2.19, respectively.

Shannon and McClain [70] used this new information to scale the heights of the roughness elements from the simulated Lagrangian droplet surface to match the scans from the Appendix O ice accretion labeled 113012_04, seen in Figure 2.18. The resulting scaled surface was designed to model the leading 17.1% chord of a NACA 0012 airfoil in Appendix O ice accretions, and is shown below in Figure 2.20.

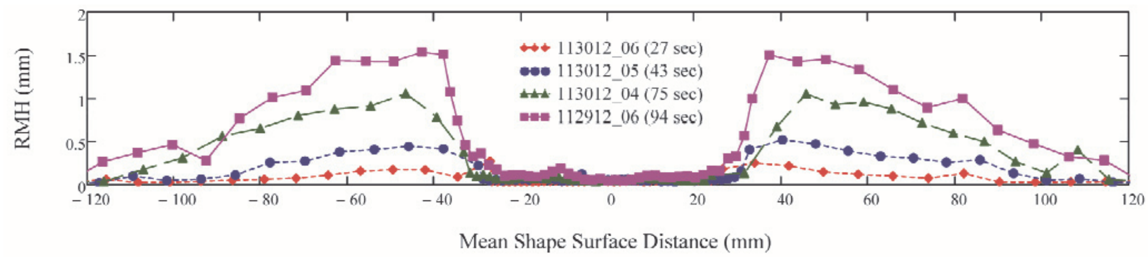

Figure 2.18: RMH ice trends on a NACA 0012 in Appendix O conditions [16]

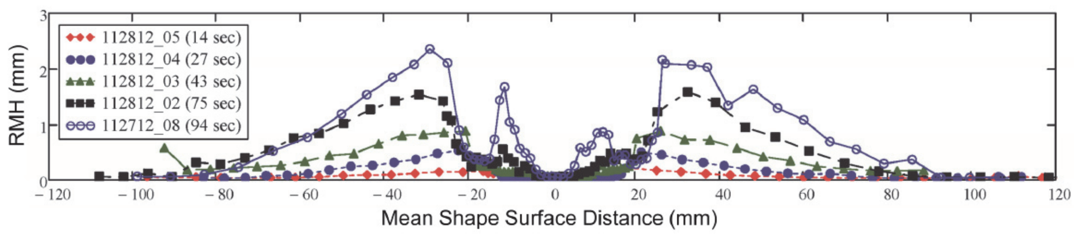

Figure 2.19: RMH ice trends on a NACA 0012 in Appendix C conditions [69]

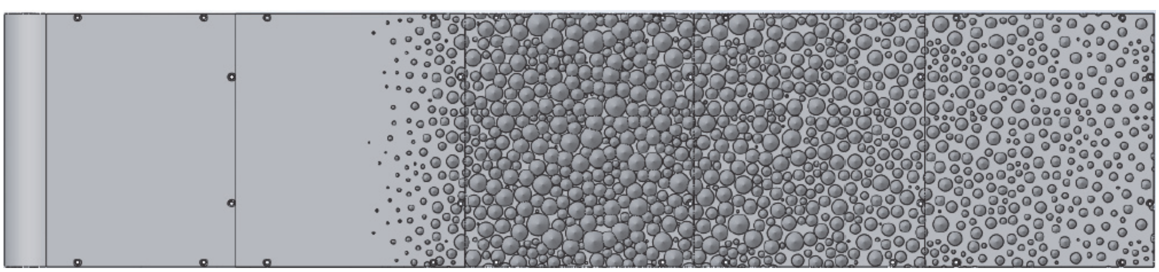

Figure 2.20: Surface model of 113012.04_IRT_cones [17]

The new 113012.04_IRT surface was retested against the old 052996.04_SSL surface which had abrupt smooth-to-rough transition and constant downstream roughness properties, seen previously in Figure 2.15. The surfaces were printed out of ABS plastic using rapid-prototyping manufacturing, as well as cut into aluminum plates using CNC methods. Plastic surfaces using both cones and hemispheres for the roughness elements were made, and aluminum surfaces used cones for roughness elements. Shannon and McClain [70,71] tested the surfaces in flows with favorable pressure gradients (accelerated). However, the leading 2% chord region of the plates were unable to be properly replicated or heated like an actual airfoil due to the shape of the ceiling insert which accelerated the flow.

Hughes et al. [18] expanded on the research of Shannon and McClain [70,71] by performing tests in the NASA Glenn Vertical Icing Wind Tunnel on new Lagrangian droplet surfaces specifically designed to model the leading 2% chord region of the NACA 0012 airfoil scans. This allowed a complete picture of the leading 17.1% of a simulated NACA 0012 airfoil modeled with Lagrangian droplet simulated roughness elements to be produced. Nevertheless, these surfaces were all still modeled using simulated roughness elements designed to imitate real ice accretions.

The objective of this investigation is to further expand the works of Tecson and McClain [65,66], Walker et al. [67], Shannon and McClain [70,71], and Hughes [18] by creating new flat-plate surfaces from unwrapped laser-scanned ice accretions. The "real ice" surfaces will be manufactured out of ABS plastic and aluminum as in previous studies, and will be tested both in flows with negligible acceleration and freestream acceleration. Convective heat transfer coefficients will be measured, as well as velocity boundary layer profiles, for comparison against the Lagrangian droplet simulated surfaces. This data and results from this study will add to the understanding of icing boundary layer development, and help to improve the LEWICE accretion code.

CHAPTER THREE

Materials and Methodology

To better understand how ice accretions on airfoils affect the surface convective heat transfer and velocity boundary layer of an airflow, a series of experiments were performed. The airfoil was modeled by a flat test plate in a wind tunnel with a ceiling insert, and multiple surfaces were used on the test plate to act as ice roughness. The main surface of note was made from a laser scan of a real ice accretion. A new sawtooth leading edge trip was also used in some tests to force turbulent flow downstream of the leading edge. This new leading edge trip was also used with Lagrangian droplet simulated roughness surfaces from previous experiments. Two sets of experiments were performed on each surface: one to measure the convective heat transfer coefficient and another to characterize the velocity boundary layer. This chapter is an overview of the design and construction of the apparatuses used in these experiments, as well as a description of the experimental procedures themselves.

Instrumented Test Plate

The test plate was designed to emulate the leading edge region of the 21” chord length NACA 0012 airfoil which was used in the experiments of Anderson et al. [46]. The significant region is the leading 17.1% (3.6”) immediately downstream of the stagnation point, as this was the predominant region where ice accreted. For reference, see Figure 1.3. This region was then geometrically scaled up by a factor of ten, and the test velocity reduced by a factor of ten in order to match the Reynolds number of the airfoil. For ease of manufacturability, the test plate was designed to be flat. However, a flat test plate does not experience the same flow as an airfoil, which accelerates flow downstream of the stagnation point. To replicate an airfoil's flow acceleration, a ceiling insert was designed for the wind tunnel test section. This insert is discussed later in this chapter.

The test plate was constructed by Tecson [13], and a thorough description can be found in that paper. For the purposes of this paper, a cursory description will be given. A model of the test plate is shown in Figure 3.1. The plate is mounted on a Plexiglas floor for installation in the wind tunnel test section. The top of the test plate is made up of interchangeable surface panels, eliminating the need to construct a new test plate for each surface. The test plate can be further categorized into four subdivisions which will be discussed in greater detail:

1. Plexiglas sub-plate
2. Instrumentation and wiring
3. Mylar film heaters
4. Aerodynamic features

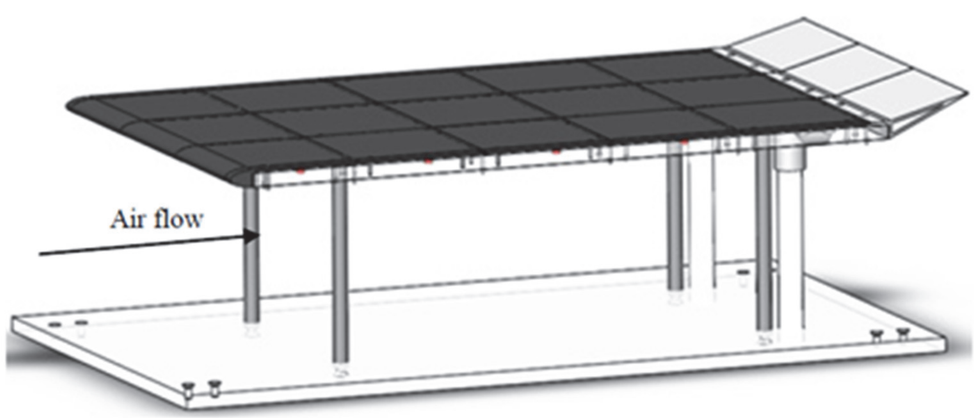

Figure 3.1: Solid model of test plate [13]

Plexiglas Sub-Plate

The surface panels were mounted to a Plexiglas plate measuring 24” x 36” x 0.75”. A high speed router with a 1/2" diameter straight bit was used to cut channels to a depth of 0.035” which allowed copper electrodes to sit flush with the surface. A 1/8” diameter straight bit was used to cut smaller channels for thermocouples to be placed on the top side of the plate. For wiring purposes, through-holes were drilled in the off-center ends of each of the thermocouple channels. The bare Plexiglas sub-plate after machining is shown in Figure 3.2.

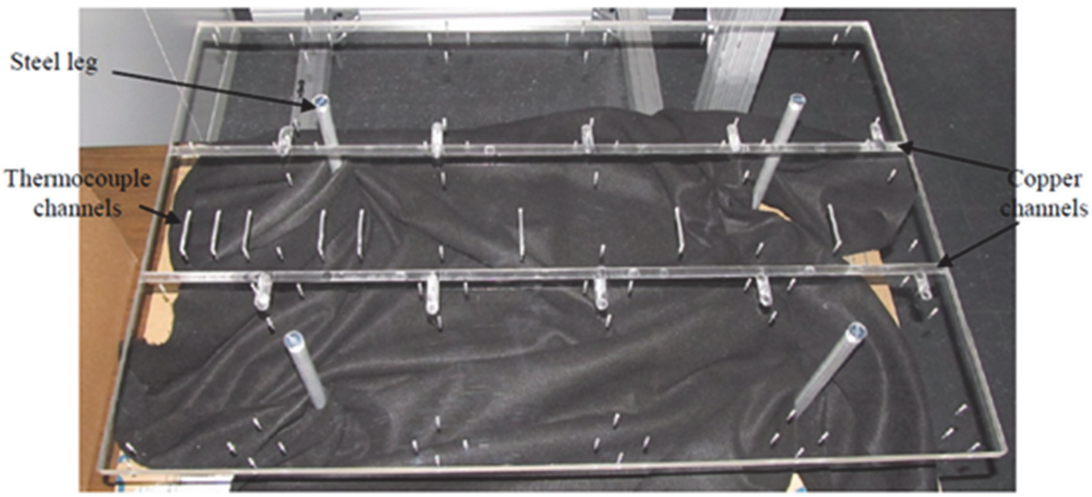

Figure 3.2: Plexiglas sub-plate [13]

Instrumentation and Wiring

To measure the subsurface temperature of the Plexiglas sub-plate, eight Type K thermocouples were embedded in the thermocouple channels (shown in Figure 3.2) and then covered in epoxy. The thermocouple beads were positioned at the longitudinal centerline of the plate, and the wires were routed through the holes at the other ends of each channel. The plate was designed to have five heated sections, so five of the thermocouples were located at the centers of the heated sections, two thermocouples were added to the first section (closest to the leading edge), and one thermocouple was added to the second section. The additional thermocouples were added in order to increase fidelity near the leading edge where gradients are the highest. To measure the temperature directly underneath the plate, eight more self-adhesive Type K thermocouples were fixed to the bottom of the test plate directly below the thermocouple channels.

Together, the eight thermocouple pairs account for the heat loss through the bottom of the test plate. The thermocouple pairs were numbered according to the heated sections, with letters designating multiple pairs in the first two sections. Figure 3.3 shows a side view of the test plate highlighting the locations of the thermocouple pairs. Dimensions are in inches, and are with respect to the leading edge of the Plexiglas subplate. To evaluate the surface distance from each thermocouple to the actual leading edge, add 1.7285" to the reported dimensions.

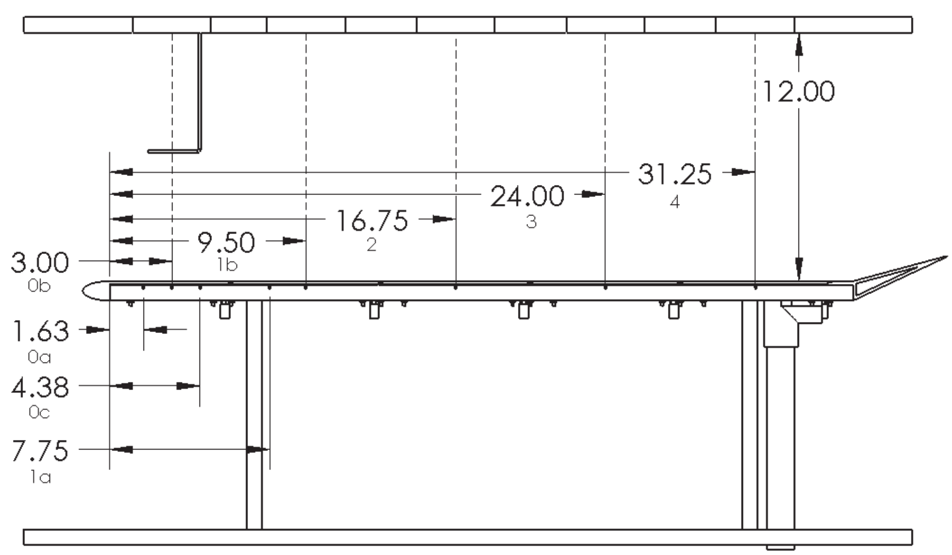

Figure 3.3: Side view of test plate showing thermocouple placement from the leading edge of the Plexiglas sub-plate (dimensions in inches, flow is from left to right) [13]

The copper electrodes in the Plexiglas channels were connected to terminal posts underneath the plate. Figure 3.4 shows another side view of the test plate highlighting the terminal posts and the electrical junction box where the wiring was routed. For a more detailed description of the terminal wiring, refer to Tecson [13].

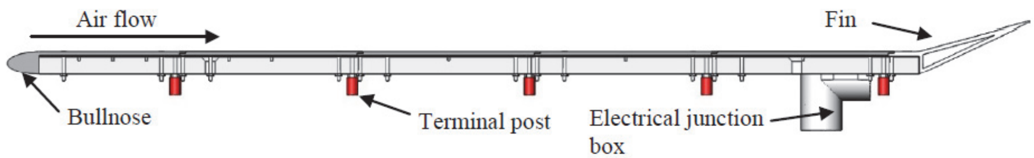

Figure 3.4: Side view of test plate [13]

Mylar Film Heaters

Gold-deposited Mylar film served as a heater in five different sections of the test plate. The heaters were used to provide a nominally constant flux boundary condition for each of the heated sections. Each heater was stretched between the copper electrodes set in the channels in the Plexiglas sub-plate. Conductive silver paint was used to connect each heater to the copper electrodes. The Mylar film has a significantly higher resistance than the copper electrodes and the silver paint, meaning that most of the heat loss occurs through the Mylar heaters themselves. The heaters were separated by 1/4" gaps which allowed screws to pass through the lap joints of the surface panels. These features can be seen in Figure 3.5, where the shaded regions represent the location of the Mylar film heaters. Figure 3.6 shows the copper electrodes, the terminal posts, and Mylar film installed in the second and third sections of the plate.

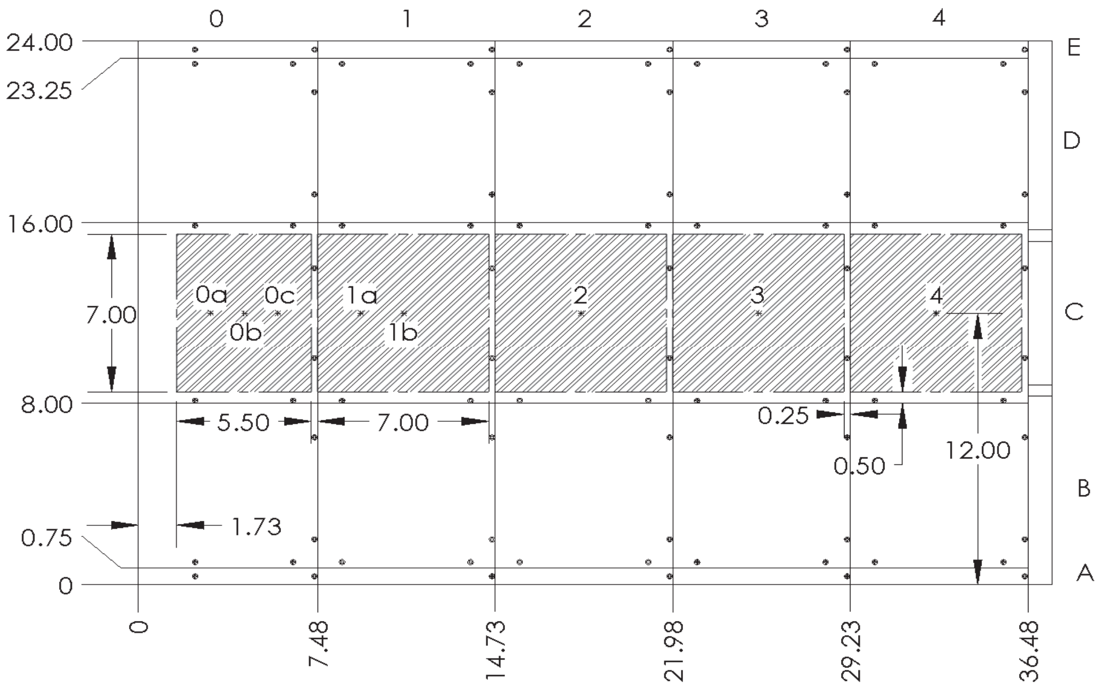

Figure 3.5: Layout of the heated sections on the Plexiglas sub-plate (dimensions in inches, flow is from left to right) [13]

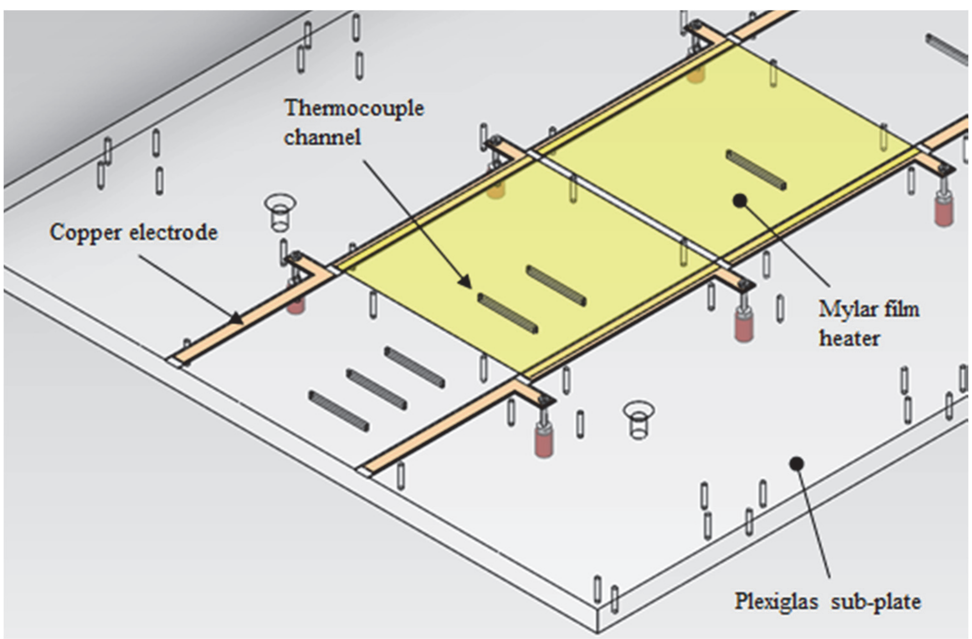

Figure 3.6: Isometric view of test plate with Mylar film heaters installed in the second and third heated sections [13]

Ceiling Insert for Flow Acceleration

Ceiling Insert Design

Since flow over an airfoil accelerates, a ceiling insert was designed to accelerate the flow over the flat plates. This accelerated flow needed to replicate the acceleration found over a 21” chord NACA 0012 airfoil at 0° AoA. The design needed to match the local Reynolds number variations for both the flat plate and the NACA 0012 airfoil, as shown in Eq. (3.4).

$$\left.\frac{\rho U_e x}{\mu}\right|_{Plate} = \left.\frac{\rho U_e s}{\mu}\right|_{\substack{NACA\\0012}} \tag{3.4}$$

Eq. (3.4) indicates that the geometry and velocity must be scaled as flow moves downstream in the x-direction from the stagnation point of the test plate. Also note that the local Reynolds number of the NACA 0012 airfoil is calculated based on the surface distance from the stagnation point of the airfoil along the surface direction (s).

The ceiling insert was designed and manufactured by Shannon [17], and a thorough description can be found in that paper. For the purposes of this paper, a cursory description will be given. A vortex-panel solver was used to generate the pressure coefficient variation along the surface of a NACA 0012 airfoil. This distribution along the surface of the NACA 0012 airfoil is shown in Figure 3.7. The region to the left of the vertical line in Figure 3.7 is the leading 17.1% of the NACA 0012 airfoil that was modeled.

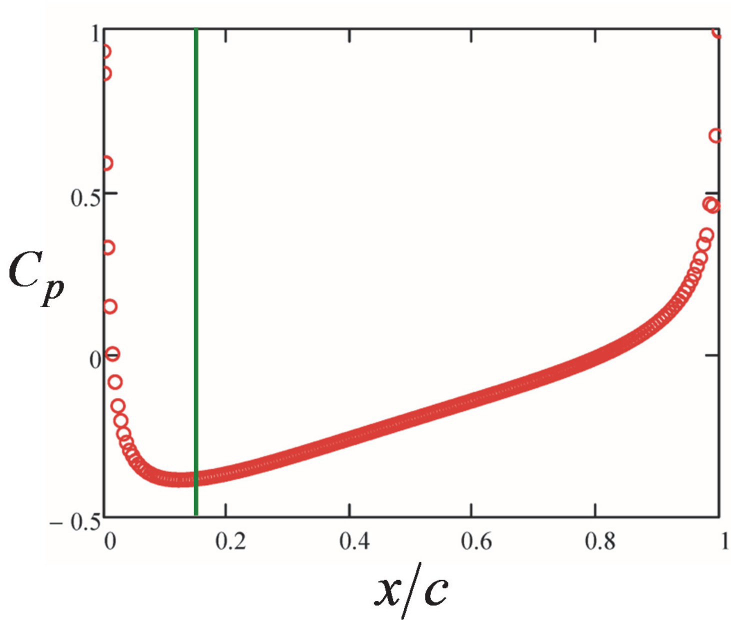

Figure 3.7: Pressure coefficient variation along a low speed NACA 0012 airfoil [17]

The pressure coefficient variation was then converted to a velocity variation using Eq. (3.5), where the surface geometry scaling factor is 10.

$$U_e(x) = \frac{U_{\infty,IRT}}{10}\left(1 - C_p\right)^{1/2} \tag{3.5}$$

Figure 3.8 shows the resulting velocity variation. The velocity variation was chosen to match the velocity variation over the surface of the NACA 0012 airfoil. Note that the acceleration in the first 0.02% of the airfoil near the stagnation region was not matched, and this region was studied by Hughes [18]. Flow stagnation cannot be easily achieved when using a flat plate and a ceiling insert, so a "cut-in" velocity U_{CI} , of 5 m/s was used. This means that the ceiling insert was designed to provide a flow velocity of 5 m/s. in the bullnose region, and the design velocity variation converged to the airstream velocity variation downstream of the bullnose.

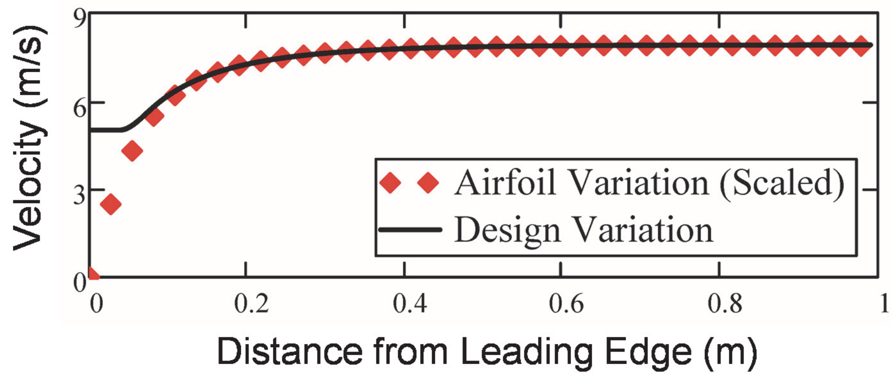

Figure 3:8: Scaled airfoil velocity variation and design velocity variation [17]

The velocity variation was then used in a boundary layer code which calculated the momentum thickness growth on both the test plate and the ceiling of the wind tunnel test section. The thickness profile of the ceiling insert was then calculated, and the ceiling insert could be constructed.

Ceiling Insert Construction

The ceiling insert consists of a wood mounting plate glued to a shaped foam profile with five cylindrical viewing ports cut down the center. Figure 3.9 shows a solid model of the completed insert.

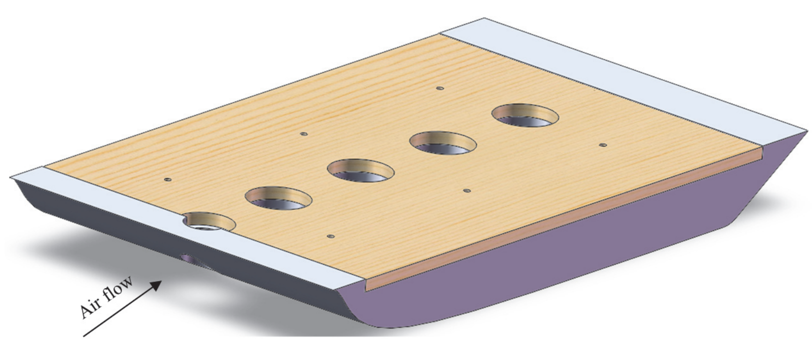

Figure 3.9: Solid model of ceiling insert [17]

The viewing ports in the ceiling insert are located directly above the center of each heated section of the test plate, and allow infrared measurements to be taken in the wind tunnel test section. The viewing port closest to the leading edge of the insert has a smaller diameter than the other ports, which was done in an effort to minimize the interference of the port with the curved profile of the insert.

Aerodynamic Features.

As mentioned in Tecson [13], two noteworthy aerodynamic features were also added to the test plate design: a bullnose on the leading edge and a tail fin at the trailing edge. The bullnose was added so that flow would not separate from the plate surface at the leading edge. The tail fin was added as a deterrent to preferential flow migration to the top side of the plate. The PVC pipes, test plate legs, electrical connectors, and other minutiae instrumentation cause flow to migrate over the top of the plate rather than the bottom. This would cause an unequal mass balance, and flow separation would occur more easily. The tail fin was added and designed so that its frontal cross-sectional area is approximately equal to the frontal cross-sectional area of the blockages underneath the plate. Both the bullnose and tail fin could be seen previously in Figure 3.1

Real Ice Roughness Surface

Building on the work done by Tecson [13], Walker [14], and Shannon [17], a new surface was built based on a laser scan done by McClain et al. [15], designated 113012.04. As mentioned in Chapter 2, Shannon [17] used this laser scan to scale a Lagrangian droplet simulated surface he designated 113012.04_IRT, seen previously in Figure 2.20. The new surface used in this study did not use simulated elements, but the actual surface ice roughness from the 113012.04 laser scan. With test panels representing an actual ice formation, it was possible to experimentally compare a real ice surface with simulated surface models. However, the laser scan data needed to be adjusted because of the shift from a curved airfoil to a flat plate. These next sections describe the process of generating flat panels with real ice roughness.

Generating Surface Model Using Laser Scan

The IRT at NASA Glenn was used to create an ice accretion on a 21" chord NACA 0012 airfoil at 0° AoA that spanned the whole 72" of the test section. After the ice had accreted on the airfoil, the wind tunnel velocity was reduced to approximately 5 m/s and the static temperature was held at approximately -4 °C to avoid ice thawing. The iced airfoil was painted with an alcohol-based titanium dioxide paint, and the leading 120-150 mm of both sides of the airfoil edge were laser scanned using a ROMER Absolute Arm. The scan was located at the center-span of the airfoil, and was approximately 100 cm wide in the spanwise direction. A picture of the laser scan can be seen in Figure 3.10.

The laser-scanned surface was then analyzed using the self-organizing map (SOM) method developed by McClain et al. [68] and McClain and Kreeger [15], and which was outlined in the previous chapter. The SOM method is a neural network approach which uses codebook vectors to represent clumps of data, and these codebook vectors are iteratively moved towards the local clump of points they are closest to. The codebook vectors represent the region of data they are near, and they are daisy-chained together with linear connections. The surface used in this study (113012.04) and the codebook vectors from the SOM method were shown previously in Figure 2.16.

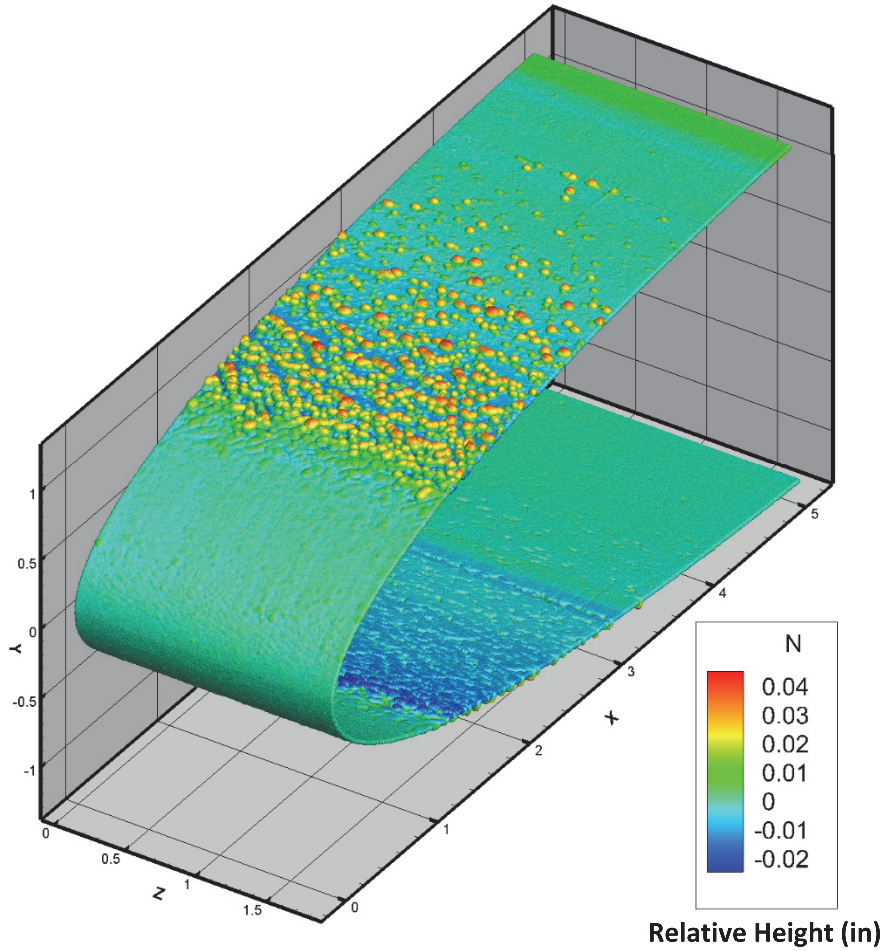

Figure 3.10: Height map of laser-scanned 113012.04 ice accretion case

The daisy-chain of codebook vectors represent the mean iced surface, also known as the ice manifold. The SOM approach assumes that the manifold is a first-order, two-dimensional shape with the characteristic that at each codebook vector the local slope of the manifold is assumed to be equal to the central finite-difference evaluated using the two closest surrounding codebook vectors. Further, deviations from the manifold are assumed to be normal to the manifold. This means that the deviation of a surface measurement normal to the line through its codebook vector with the local slope set by the neighboring codebook vectors is considered to be the "height" of the surface point.

The local 99.9% roughness maximum height (RMH) based on a Gaussian distribution for each codebook vector is calculated using Eq. (2.29), as seen in the previous chapter. The coordinate systems used to describe the airfoil surface, the mean ice manifold, and the X-Y (chord-chord normal) plane are shown in Figure 3.11.

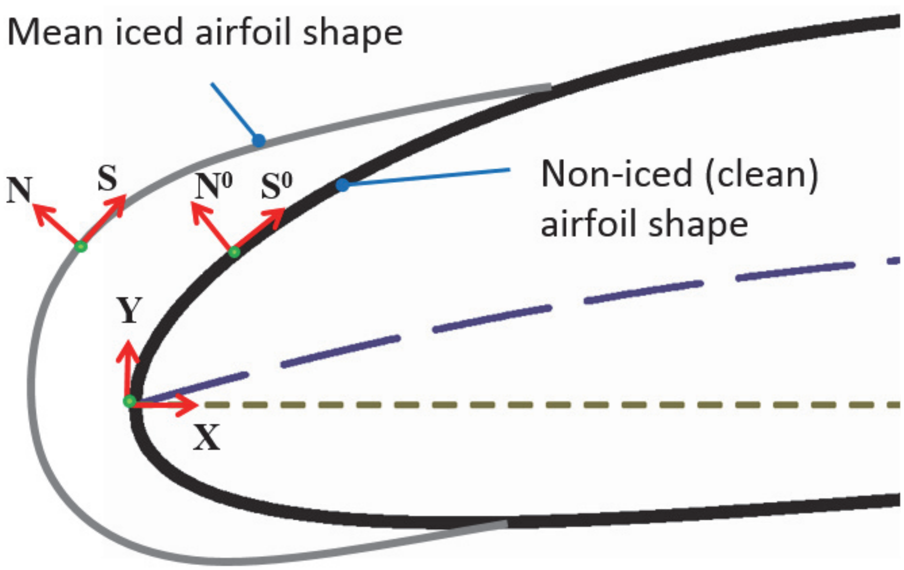

Figure 3.11: Coordinate systems used in the SOM method [72]

S represents the direction along the mean ice manifold surface in the direction of the flow, and N represents the direction normal to the ice manifold surface in the direction of the flow. S^0 and N^0 represent similar directions, respectively, but are applied at the airfoil surface itself. The laser-scanned surface of the real ice accretion shown in Figure 3.10 needed to be "unwrapped" for the ice roughness to be printed onto a flat surface. However, the codebook vectors must first be defined in terms of traditional airfoil coordinates. A discrete arc-length approach is used, using S and N coordinates. At one end of the daisy-chain of codebook vectors, the arc length is defined to be a known value (or zero) away from the stagnation point on the airfoil. Then, the surface distance of each codebook vector (and in turn, the surface distance of each point cloud measurement) can be calculated as an S-distance along the ice manifold. The RMH calculated at each codebook vector describes the statistical height away from the mean ice manifold surface in the N-direction normal to the surface.

To unwrap the ice roughness point cloud, however, merely converting S-distance from stagnation into x-distance from stagnation was not adequate. A few intermediate steps were necessary. The scan from the ROMER Absolute Arm yielded a point cloud of x-y-z-coordinates. Once the SOM method had been applied, resulting in codebook vectors and RMH values, the x-y-z points were converted into surface thickness projection S^0-N^0 coordinates as shown in Figure 3.12.

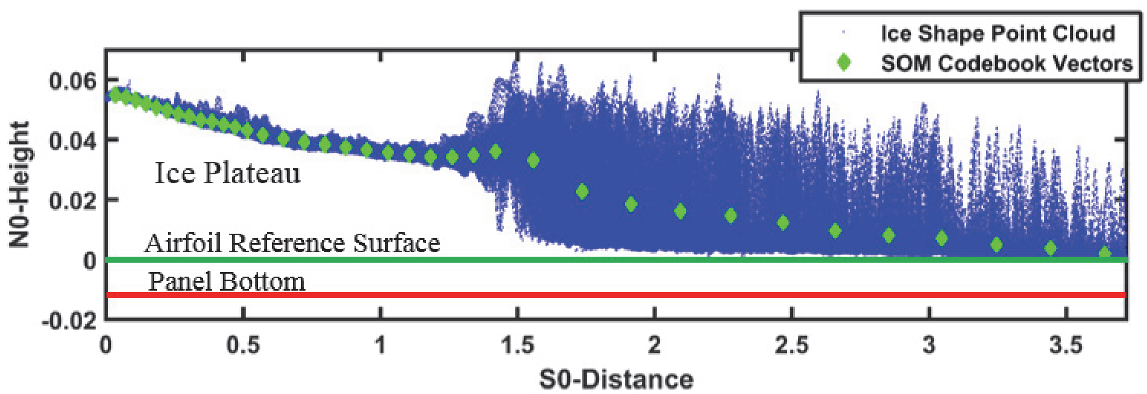

Figure 3.12: Surface thickness distribution of laser scanned ice roughness points

The lowest relative height of these coordinates correspond to the airfoil reference surface, as noted in the figure. However, the first ten to fifteen inches of scaled airfoil surface don’t actually have relevant roughness—the surface is made up of smooth glaze ice. The leading edge data points only represent surface thickness due to the glaze ice plateau which is formed from the thin film liquid layer freezing near the stagnation point. In this study, the glaze ice roughness is negligible compared to the roughness which builds up after about the ten-inch mark in scaled coordinates (the one-inch mark in real coordinates). Therefore, the next step in adjusting the S^0-N^0 laser-scanned points was to use a code to "level" the entire set of data points respective to the leading edge. Recall that the codebook vectors represent the mean ice manifold, which is at some mean thickness away from the airfoil surface. To focus specifically on roughness instead of thickness, the codebook vectors and their corresponding point cloud clumps were shifted into S-N coordinates. This makes thickness a negligible factor, and only the salient roughness on the mean ice manifold remains. The "leveled" data points can be seen in Figure 3.13.

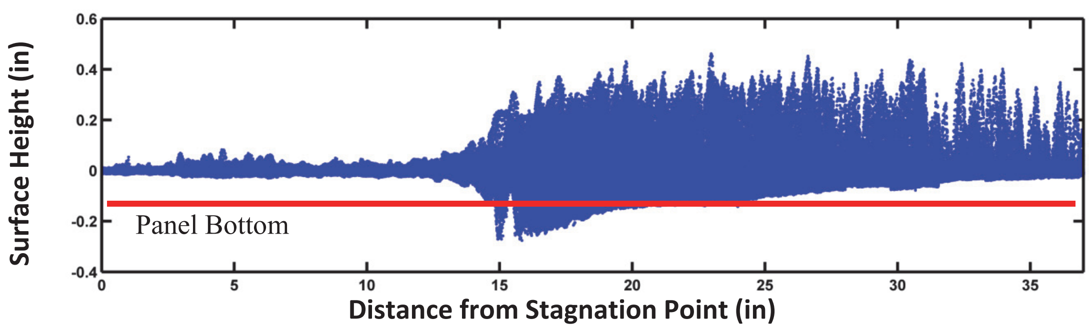

Figure 3.13: Leveled surface height distribution of laser scanned ice roughness points

The results of the surface "leveling" code represent surface roughness, but the roughness near the fifteen-inch mark had been lowered below the panel bottom, and the roughness near the trailing edge had been raised above the panel bottom. To accommodate the test panel form factor yet still maintain relative roughness features, the points were shifted once again to sit flush to the panel surface. Additionally, to match the previous test panels' smooth entry region, the leading 7.5 inches were removed. This finally yielded a point cloud which accurately modeled the unwrapped 113012.04 case on a flat surface. The points displayed in surface height per distance from stagnation point can be seen in Figure 3.14, and a 3D section of these points can be seen in Figure 3.15.

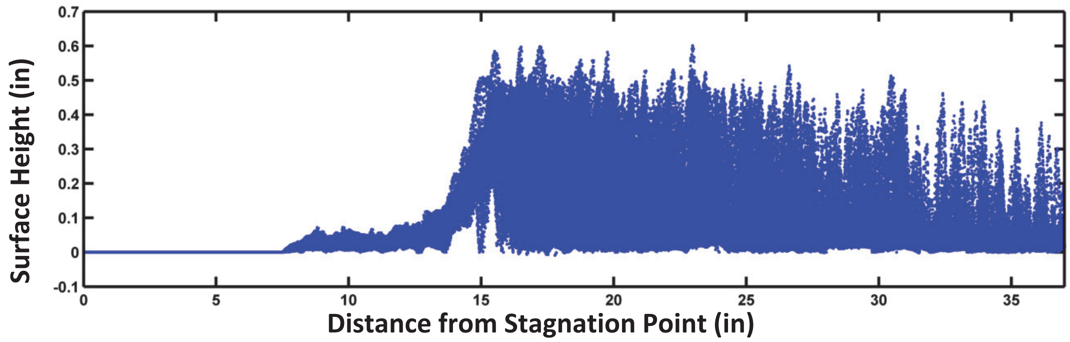

Figure 3.14: Surface height distribution of laser scanned ice roughness points

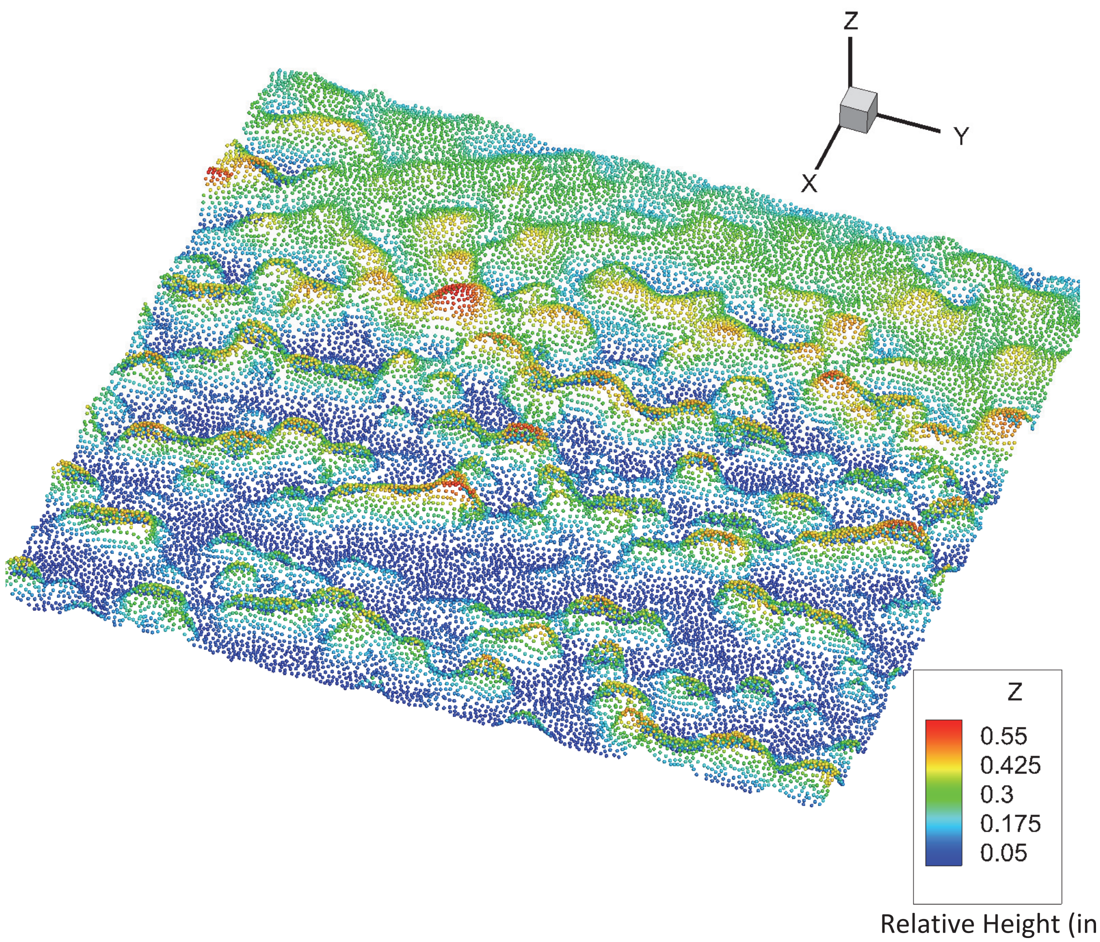

Figure 3.15: Plot of surface height map from a selection of the leveled laser-scanned points

To more easily transfer this new surface map from a point cloud to a 3D model for manufacture, it proved beneficial to interpolate the points and resample to generate a higher-quality surface. A quadratic interpolation code was used which generated a surface function to fit the raw point cloud. The surface function was resampled for new surface points with which to generate a STL file for use in 3D printing or CNC manufacturing. A section of the resampled surface can be seen in Figure 3.16, and the same section as an STL file can be seen in Figure 3.17.

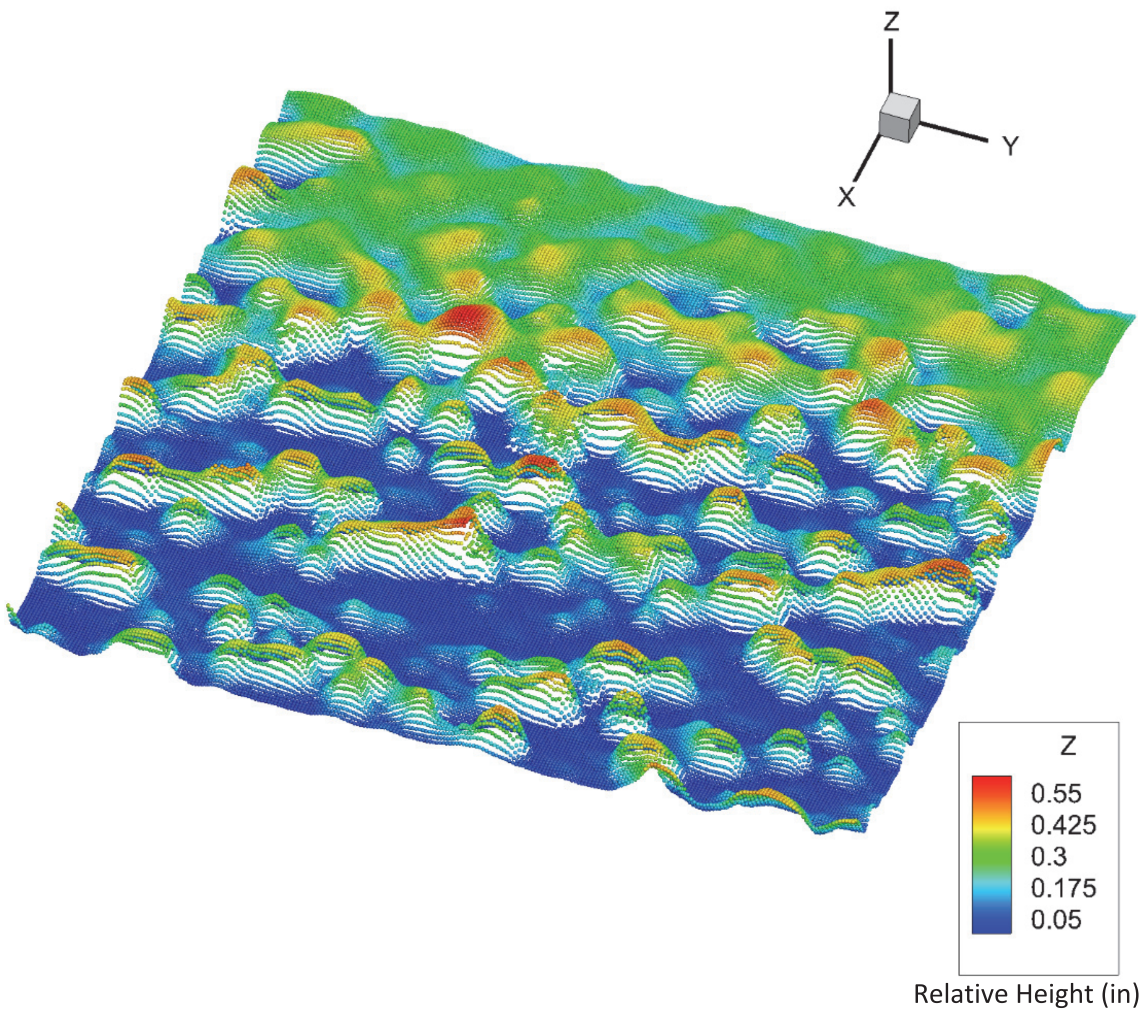

Figure 3.16: Resampled surface height map after quadratic interpolation

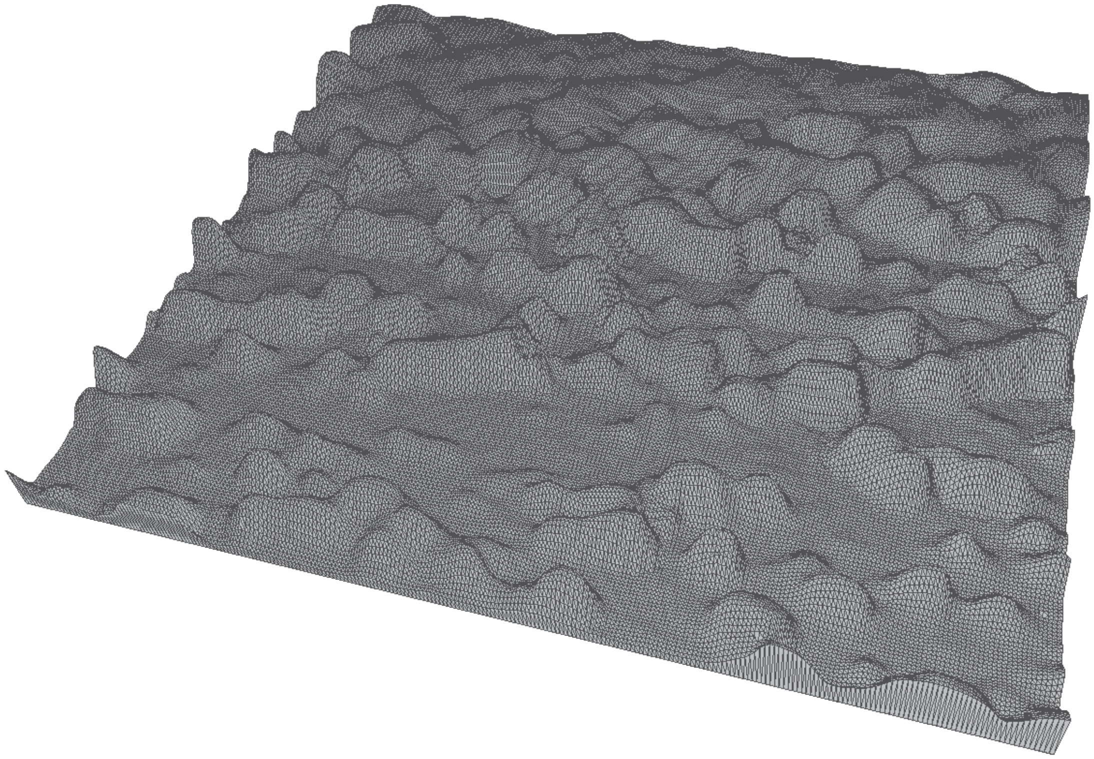

Figure 3.17: STL file generated from the resampled surface

Manufacturing Real Ice Surface Panels

Once the STL file of the roughness was generated, it was split into panel sections to be manufactured. A Dimension SST 1200es was used to print the ABS plastic panels, and secondary Row C sections were also machined out of a plate of aluminum 6061 using a Haas VF 1 vertical-axis CNC mill. The surface panels of the heated Row C section (see Figure 3.5 for the naming designation) were spray painted with a thin coat of matte black paint to provide a known surface emissivity of 0.95. A photo of the four unpainted aluminum panels in Row C are shown in Figure 3.18. The full test plate with finished surfaces used is shown in Figure 3.19.

Figure 3.18: Unpainted aluminum surface panels with real ice roughness

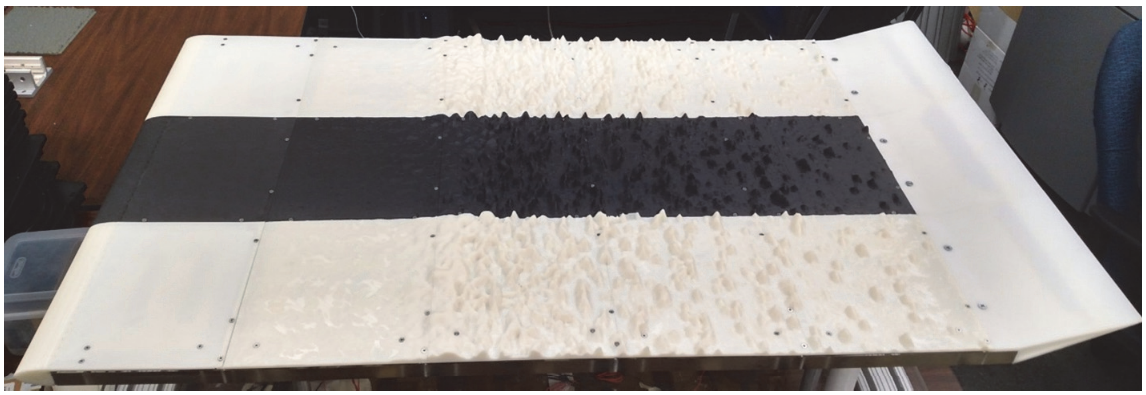

Figure 3.19: Finished surface panels with real ice roughness on the test plate

Leading Edge Trip

In addition to the realistic ice surface, a new leading edge was made to initiate turbulent flows over the test plate. The idea behind having optional panels with a leading edge trip was that the droplet interaction in the thin film liquid layer near the stagnation point might be enough to induce turbulent flow over the rest of the airfoil. The purpose of the leading edge trip is to test if early-induced turbulent flow creates a significant change in the convection downstream of the location of maximum ice roughness. A leading edge trip had been designed and used in previous studies, but a new model was made with a few improvements. The old turbulent leading edge, seen below in Figure 3.20, was a 2 mm square trip glued immediately downstream of the bullnose curvature.

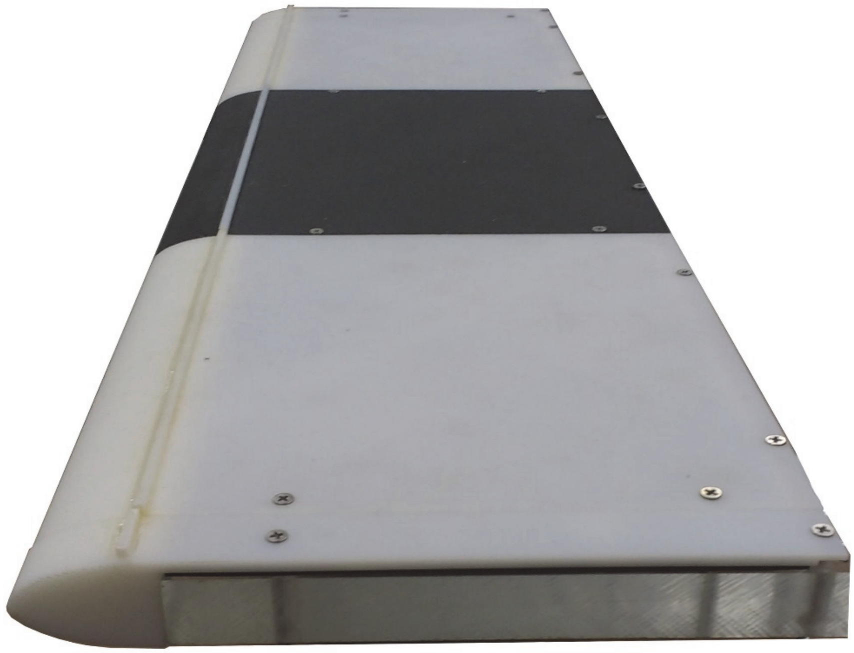

Figure 3.20: Old leading edge trip used to induce turbulent flow

The problem with the old leading edge was that the trip was so tall it created too much flow separation before the roughness. The separated flow would reconnect with the surface, but far enough downstream to shift the flow results noticeably. The new leading edge was designed to be less intrusive to the flow, creating much less separation, yet still inducing turbulence. This was accomplished by reducing the trip height to 1 mm, and by making it a sawtooth pattern instead of a solid beam. This can be seen in Figure 3.21. Additionally, the profile was changed from a square profile to a triangular profile, with backside of the trip angled down to the surface to discourage flow separation. The profile can be seen in the inset of Figure 3.21. The new leading edge panels were then saved as STL files and manufactured out of ABS plastic using a Dimension 768 SST.

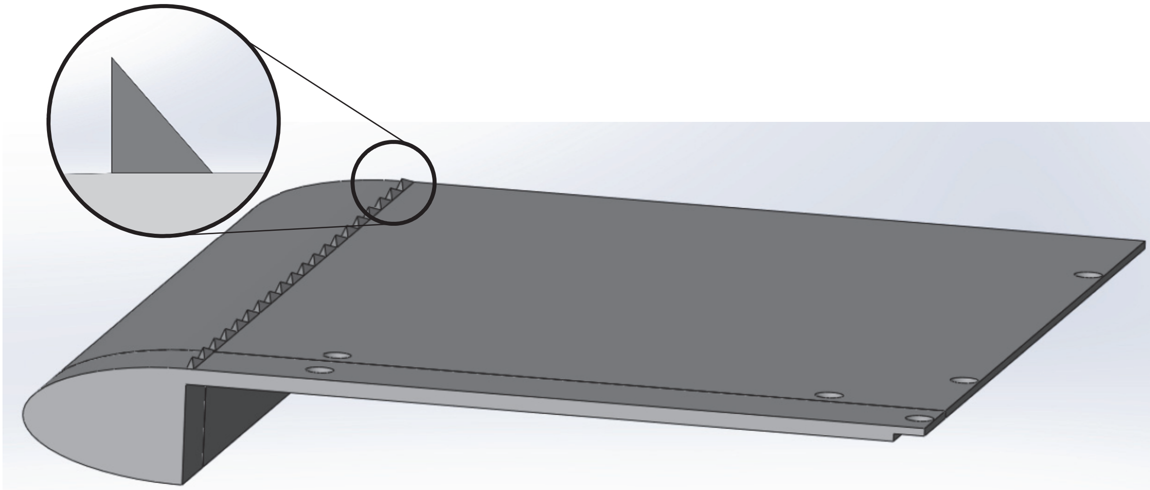

Figure 3.21: New sawtooth leading edge trip. The inset is the trip profile

Lagrangian Droplet Simulated Ice Roughness Surfaces

In addition to the realistic ice surfaces, several simulated ice roughness surfaces were used with a modified leading edge trip. The surfaces themselves were the same Lagrangian droplet simulated roughness surfaces developed by Tecson and McClain [13] and used in previous studies, although new tests were done with the heated panels made out of aluminum. The surface distribution of these simulated ice roughness panels was created using the historical description of an "Appendix C" roughness on a 21" chord NACA 0012 airfoil. Roughness elements spacing-to-diameter coefficients were determined based on data reported by Anderson et al. [46] and Shin [45]. The major experimental change was the modified leading edge trip. As stated before, the leading edge was designed to induce transition to turbulent flow before the flow even reached the ice roughness. The next few sections present an overview of how the surfaces were generated in previous studies, with additional details about aluminum manufacturing and the new leading edge.

Historical Ice Roughness

The run identifier 052996.04 corresponds to the historical description of ice roughness from the "Appendix C" experiments of Anderson et al. [46], and the run identifier 113012.04 corresponds to the contemporary ice roughness distribution from the experiments performed by Shannon [17], based on the laser-scanned accretion performed by McClain et al. [16] in "Appendix O" conditions. An image of the historical ice accretion run 052996.04 is shown in Figure 3.22.

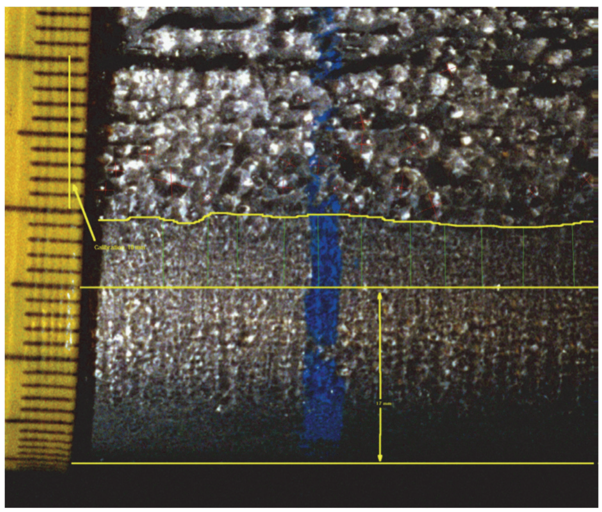

Figure 3.22: Ice accretion image for run 052996.04 from Anderson et al. [46]

The Lagrangian droplet simulator differed from the roughness parameters reported by Anderson et al. [46] in three ways: 1) overall average element diameter, 2) diameter standard deviation, and 3) element spacing-to-diameter values. Therefore, the simulator data was conditioned by truncating small diameters, stretching some roughness elements, and scaling roughness elements to match the parameters reported by Anderson et al. [46]. This data conditioning was performed by Tecson [13], and a detailed account of the procedure can be found there.

Scaled IRT Ice Roughness

Shannon [17] created a scaled surface of the simulated droplet roughness elements to match the laser scan of case 113012.04 seen in Figure 3.10. The roughness variations in the longitudinal direction along the surface of the NACA 0012 airfoil were characterized using the same self-organizing map approach of McClain and Kreeger [15]. This was the same process as before, using the local 99.9% RMH based on a Gaussian distribution for each codebook vector, calculated using Eq. (2.29). The points went through the same "leveling" process previously described, and the RMH values were organized by surface height per distance from stagnation point similarly to what was depicted in Figure 3.14.

Figure 3.23 shows that the 113012.04 case has a smooth region up to 30 mm from the stagnation point, where the roughness height rapidly increases to a maximum of approximately 1 mm just before the 50 mm mark. After this point, the roughness heights gradually decay. Eq. (3.3) represents the transition function used to model the variation in roughness height along the surface in the flow direction.

$$F_t(x) = 0.5 + 0.5\tanh\left(\frac{x - x_t}{l_t}\right) \tag{3.3}$$

where l_t is the transition length and x_t is the transition location. Eq. (3.3) is for x values much greater than x_t, and zero for x values much less than x_t. The transitions can be multiplied by either constants or functions to transition between constant values or functions. Three transition functions were combined linearly into a scaling function that modeled the RMH values of the measured 113012.04 case. Both the scaling function and the measured RMH values are shown in Figure 3.23.

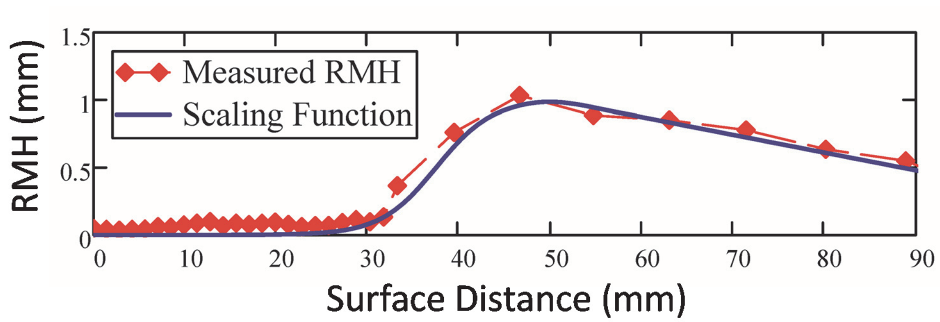

Figure 3.23: 99%-Gaussian maximum roughness height variation for the 113012.04 case point cloud [17]

Manufacturing Simulated Ice Surface Panels

As previously mentioned, the region downstream of the leading edge of the plate was geometrically scaled by a factor of ten. Therefore, the Lagrangian droplet surfaces were also scaled up by a factor of 10, were replicated in a 4x6 pattern to cover the surface of the instrumented test plate. The replication was done to prevent preferential flow in the spanwise direction. The real ice surface was scaled up by a factor of 10 and cut into a 3x4 pattern to also cover the surface of the instrumented test plate. Figure 3.24 shows the 052996.04 case as it was scaled 10x and replicated. This surface is the same surface as used by Shannon [17] and was designated 052996.04_x10_SSL because it had a smooth starting length.

The maximum RMH values (seen in Figure 3.23) of the 052996.04_x10 case and the 113012.04 case were roughly the same. Therefore, the same basic roughness pattern that was used for the 052996.04_x10 case was scaled and then used for the 113012.04 case. This was generated by multiplying the 052996.04_x10 surface by the scaling function shown in Figure 3.23 with the surface distance scaled by 10. The resulting surface was called the 113012.04_IRT surface.

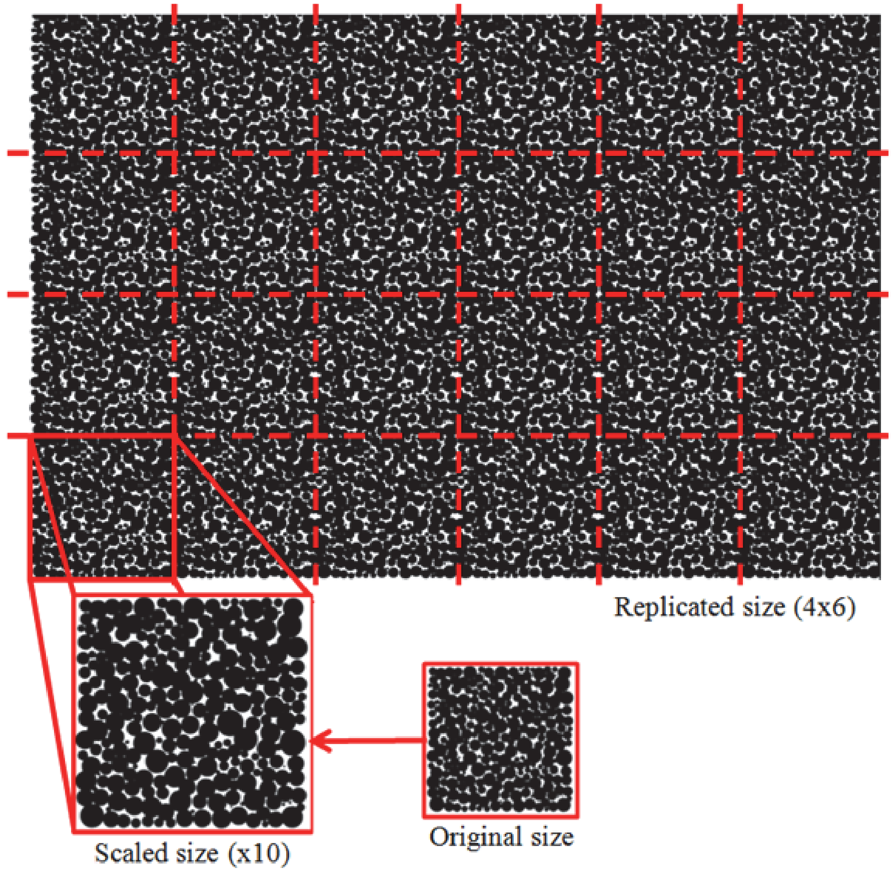

Figure 3.24: Scaled and replicated roughness distribution for the 052996.04 case (not to scale) [13]

The steps to manufacture the surface panels are summarized below:

1. Smooth surface panels, designed to fit on the 24" x 36" Plexiglas sub plate, were created in SolidWorks.
2. The roughness pattern was deconstructed into subsets, one for each surface panel.
3. A SolidWorks macro generated a solid model of the roughness distribution on each of the smooth surface panels.
4. The surface panels were manufactured using 3D printed ABS plastic in a Dimension 768 SST, and secondary Row C sections were also machined out of a plate of aluminum 6061 using a Haas VF 1 vertical-axis CNC mill.

5. The surface panels of the heated Row C section (see Figure 3.5 for the naming designation) were spray painted with a thin coat of matte black paint to provide a known surface emissivity of 0.95.
6. 1/16” neoprene gaskets were fixed to the bottom of the surface panels. This was done so that the heated sections had an even contact pressure between the Mylar film heaters and the surface panels.

The finished surfaces used are shown in Figure 3.25. The 052996.04_x10_SSL surface reflects the historical treatment of ice roughness, whereas the 113012.04_IRT surface is a more contemporary treatment of ice roughness, with a realistic variation in the roughness heights downstream of the leading edge. The unwrapped 113012.04 laser scanned surface is shown below the other two surfaces for comparison.

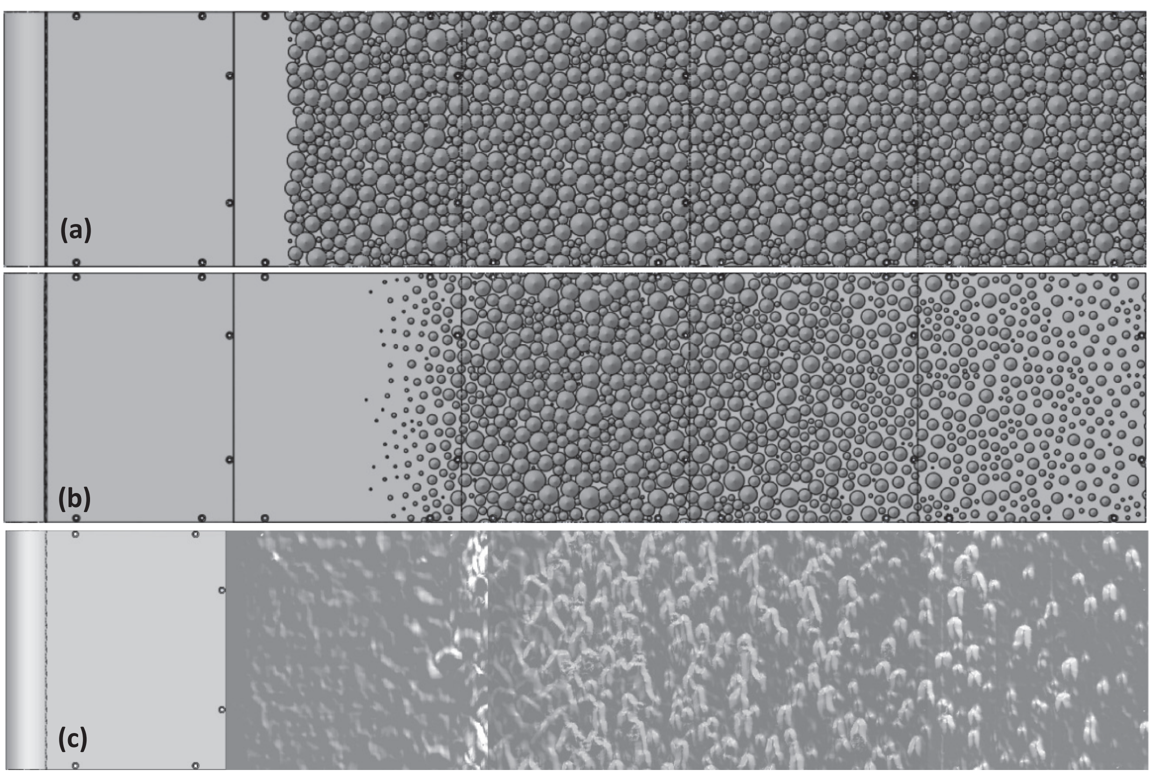

Figure 3.25: Row C surface panel assemblies of a) 053096.04_x10_SSL, b) 113012.04_IRT, and c) 113012.04_RealIce (flow is from left to right)

Experimental Setup and Procedure

The experiments were performed in the Baylor University Subsonic Wind Tunnel (BUSWT), which is a Model 406B manufactured by Engineering Laboratory Design, Inc. The flow is driven by a constant pitch fan powered by a 40 horsepower, variable speed electric motor. The test section is 24” x 24” x 48”. The tunnel uses a honeycomb inlet and three high-porosity screens to provide an inlet turbulence intensity of approximately 0.2%, and the fan is capable of producing airflows ranging from 0.1 m/s to 50 m/s with a velocity variation in the test section of less than ±1%.

Two different types of experiments were performed for each of the surfaces in this study: 1) steady-state convective heat transfer coefficient measurements, and 2) velocity boundary layer measurements. The convection measurements reveal information about the thermal properties of the rough surfaces, and the boundary layer measurements reveal information about how the flow moves over the rough surfaces. Figure 3.26 shows a sketch of the experimental setups for both of these experiments.

Convection Measurements

The convection tests gathered data to calculate the convective heat transfer coefficients across each of the five heated surface panels. A FLIR SC4000 ThermoVision infrared (IR) camera with a 25 mm lens was used, which has an indium-antimonide (InSb) detector capable of generating 320 by 256 pixel thermal maps across a surface. Based on the focal distance used in this experiment, the viewing area for each image was 6.4" in the flow direction and 5.12" in the span direction. The data from the IR camera was recorded using FLIR ExaminIR software.

The camera was mounted on a Velmex BiSlide one-dimensional traversing system on the wind tunnel ceiling and controlled by a Velmex VXM programmable stepping control motor. Five FLIR IRW-3C calcium-fluoride windows were installed to allow IR optical access to each of the heated sections on the test plate. The windows were set at an angle of 30° to eliminate reflections from the IR camera's internal cooling signature. A side view of the camera system, removable ceiling insert, and test plate is shown in Figure 3.27.

Also visible in Figure 3.27 is a 6" Pitot-static probe, which was used with an Omega PCL-2A pressure transducer with a PCL-MA-01WC pressure module to monitor the freestream velocity. The wind tunnel velocity was calibrated to match the appropriate Reynolds number using this Pitot-static probe, and the process was described by Shannon [17]. A Type K thermocouple was also attached to the Pitot-static probe to measure the freestream temperature. The ambient temperature, pressure, and relative humidity were measured at the inlet of the wind tunnel using an Omega zSeries-THPB-LCD atmospheric conditions monitor. Some tests were done with negligible freestream acceleration, so the ceiling insert was removed and the Pitot-static probe was mounted from the ceiling of the test section. The tests which accounted for freestream acceleration used the ceiling insert, and the Pitot-static probe was mounted on the floor of the test section to avoid interfering with the ceiling insert. A modified wooden rolling cart was made by Tecson [13], and housed the supplementary equipment necessary for the experiments. The equipment cart can be seen in Figure 3.28.

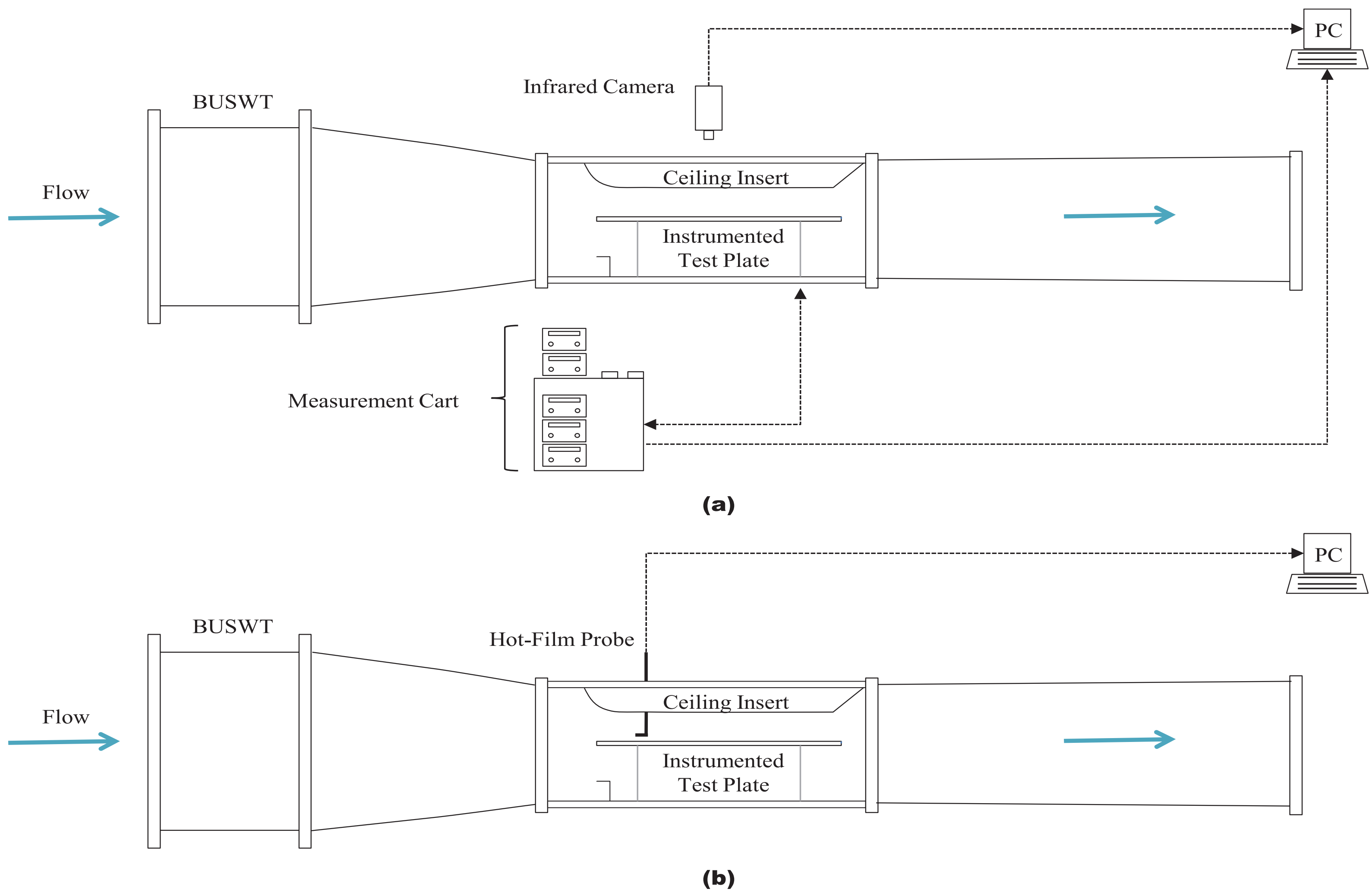

Figure 3.26: Side view of experimental setups for a) the convection tests and b) velocity boundary layer tests (not to scale) [17]

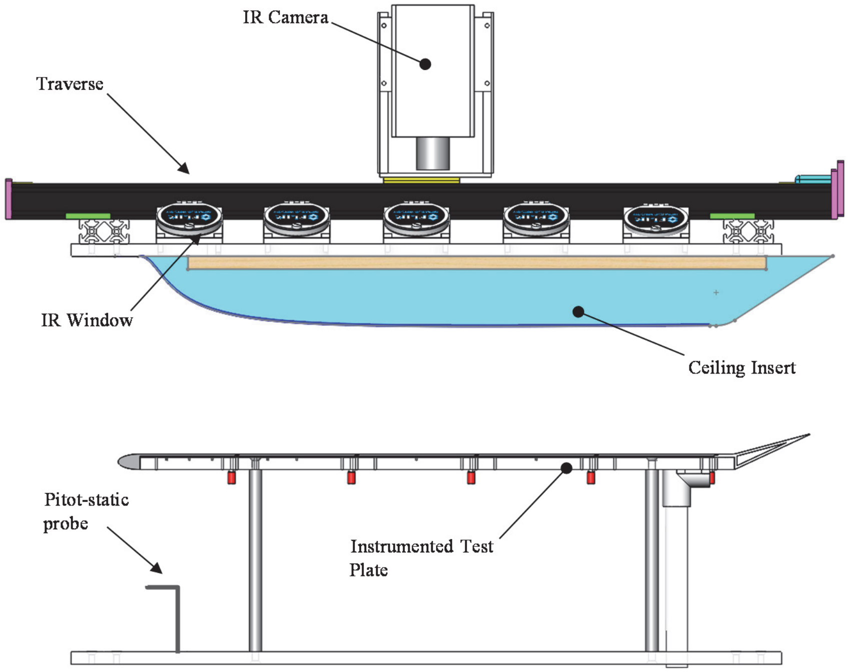

Figure 3.27: Side view of convection test section [17]

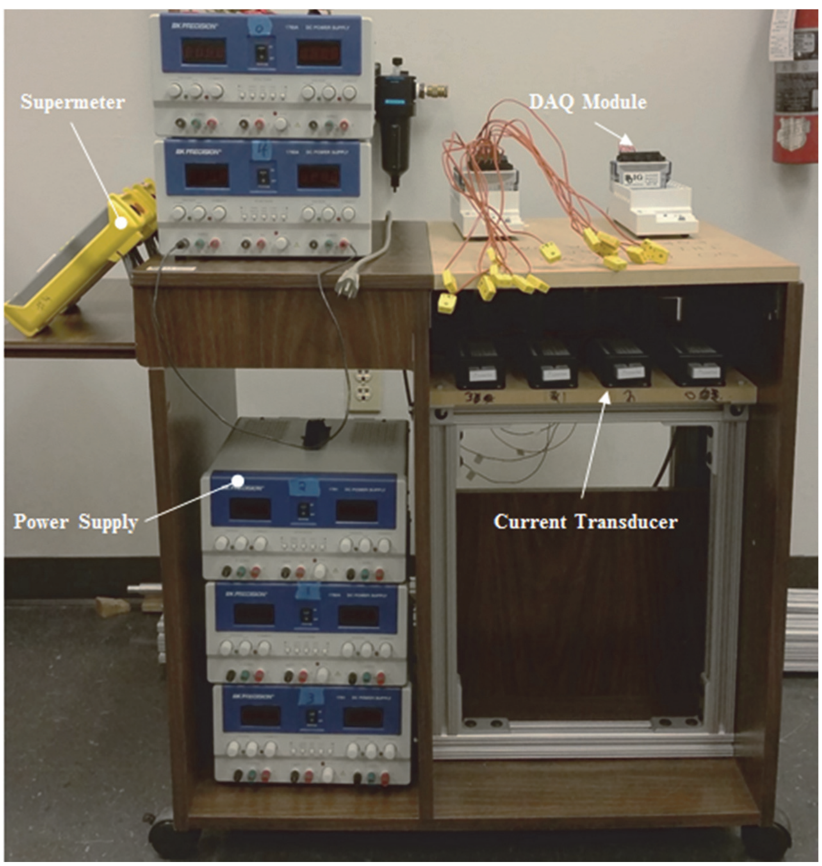

Figure 3.28: Modified wood cart outfitted with experimental equipment [17]

Five BK Precision power supplies, one for each heater, provided power to the Mylar film heaters. The voltage across heated sections 0-3 was measured using a National Instruments (NI) 9929 DAQ module. The current through heated section 0 was measured using a Powertek CTH/20A/TH/24Vdc Type 1 current transducer, and the current through heated sections 1-3 was measured using three Powertek CTH/10A/TH/24Vdc Type 1 current transducers. The transducers for sections 0-3 were read by a NI 9205 low voltage input module. Both NI modules were mounted on a NI cDAQ-9172 chassis. Due to equipment unavailability, the voltage and current through the heater in section 4 were monitored using two Newport TrueRMS HHM290/N Supermeters. A wiring diagram for the heated section measurements can be seen in Figure 3.29. The freestream thermocouple and eight thermocouple pairs were connected to five NI9211 DAQ modules, which were mounted in a second NI cDAQ-9172 chassis.

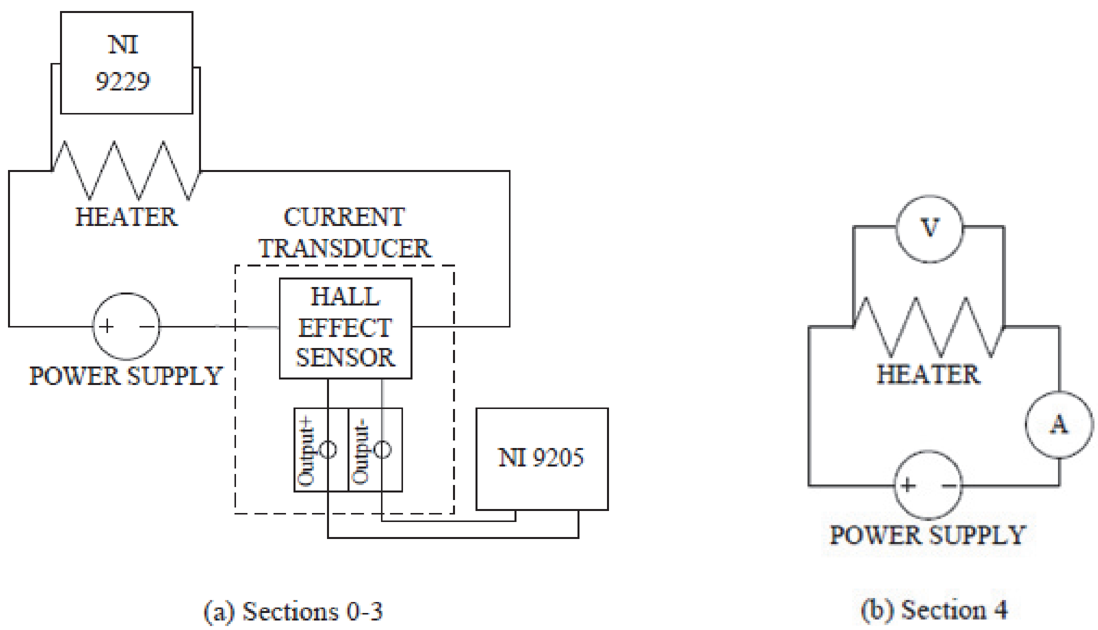

Figure 3.29: Wiring diagram for heated sections [13]

At least one day before performing a steady-state heat transfer convection test, the surface panels to be tested were attached to the instrumented test plate, and the plate was installed in the wind tunnel test section. The Pitot-static probe and IR equipment were also installed, and the camera was tested and focused. A black felt sheet was draped over the test section to minimize any light contamination or other radiative interference with the IR camera. The test section was left undisturbed overnight to ensure nominal temperature equilibrium in the test plate and ambient air.

The day of the convection tests, the following procedures were followed:

1. .The IR camera was powered on and given time to reach operating temperatures. This took at least fifteen minutes.
2. The PCL-2A pressure transducer, current transducers, DAQ systems, and Velmex motor controllers were all powered on.
3. The ExaminIR software and two LabVIEW programs were started. One LabVIEW program read the DAQ, zSeries, and PCL-2A pressure measurements, and the second program controlled the position of the IR camera using the Velmex traversing system.
4. The PCL-2A pressure transducer was zeroed. As described by Shannon [17], the velocity in the wind tunnel was set to a calibrated dynamic pressure of 0.1595 inH_2O by the floor Pitot-static probe.
5. Once steady-state temperatures were reached, calibration images were taken at each of the five positions above the heated sections. The IR camera recorded seven frames per second for ten seconds for a total of seventy frames per heated section.

6. After calibration, the wind tunnel was started. The velocity in the test section was set according to a PCL-2A transducer reading of 0.1595 inH20, as calibrated by Shannon [17].
7. The five power supplies were turned on and each set to provide a nominal flux of 500 W/m^2. The temperatures read by the eight thermocouple pairs on the test plate were monitored using LabVIEW until steady-state was reached. This usually took two hours.
8. Once steady-state was reached, The IR camera was used again to capture images at each of the five heated sections. Again, seventy frames at seven frames per second for each section.
9. At section 4, the voltage and current were manually recorded from the Supermeters at the same time that the IR images were captured at that section.
10. If an aluminum surface was being tested the power supplies were adjusted to provide an increased flux of 600 W/m^2. The temperatures were monitored again until they reached steady-state, usually taking another two hours. New IR images were captured for each section, just like before.
11. The equipment was powered down.

Velocity Boundary Layer Measurements

When performing convection measurements, it's helpful to understand the nature of the fluid flow. Velocity boundary layer profiles can indicate that the flow is not detaching, that boundary layers are developing properly, and that flow is accelerating properly. The velocity boundary layer measurements were characterized using hotwire anemometry. These tests required much less instrumentation, as the surface was no longer heated. The same Pitot-static probe, PCL-2A pressure transducer, and zSeries atmospheric conditions monitor used in the convection measurements were used again. The test section ceiling was modified to incorporate a VelMex two-dimensional traversing system so that vertical movement was possible, as seen in Figure 3.30.

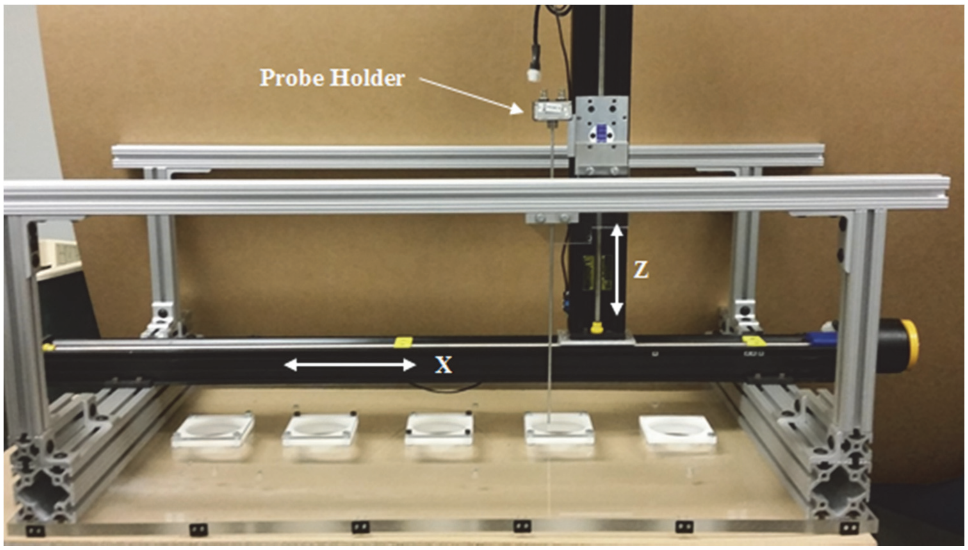

Figure 3.30: Wind tunnel ceiling with two-dimensional traversing system [17]

A model 1246-20 x-array hot-film probe was used to capture velocity boundary layer data. The probe was powered by a TSI Inc., IFA300 constant temperature anemometry system, and ThermalPro software was used with the IFA300 to assign channels to the x-array probe. The probe was mounted in a probe holder, which was initially calibrated using a Velmex B487TS rotary table. A LabVIEW program was used to rotate the probe in 5° increments over a range of ±20°, and a velocity sweep ranging from 0-20 m/s was performed at each increment. A NI 9223 DAQ module in a NI cDAQ-9178 chassis captured the velocity data from each wire.

After calibration, the velocity of the wind tunnel was set using the same procedure as the convective heat transfer tests. The hot-film probe was lowered through each of the ports in the test section ceiling and positioned directly over the center of each test plate. Additional velocity data was taken one centimeter upstream and one centimeter downstream of the center of each plate. The hot-film probe was lowered to the surface of the test plate as close as possible (within 1/64”). Special foam guards were used, along with packaging tape, to seal up the measurement ports. A LabVIEW program was used to raise the probe in the z-direction over a 6”, 101 station, geometrically expanding grid. The grid’s expansion factor was 1.07. Again, a NI 9223 DAQ module in a NI cDAQ-9178 chassis captured the velocity data from each wire. At each of the 101 stations, 300,000 samples were taken from each wire at a rate of 200,000 samples per second.

CHAPTER FOUR

Data Reduction and Uncertainty Analysis

The previous chapter outlined the experimental setup of both the convection and boundary layer tests. The data reduction process is derived in this chapter for both the convection and boundary layer tests. Further, the uncertainty of the measured and reduced variables is also quantified and discussed.

Convection Measurements

Energy Balance Equation

To track how the convective heat transfer coefficient changes with flow over roughness, the energy dissipated must be modeled. Steady-state heat experiments hinge on keeping track of heat loss, because the energy into a system must equal the energy out. Following the same methodology used by Shannon [17] and in previous studies, a one-dimensional energy balance was applied to the instrumented test plate system shown in Figure 4.1. The power supplied energy to the system via the Mylar film heater ($\dot{Q}_{GEN}$). Heat conduction through the Plexiglas sub-plate was considered heat loss ($\dot{Q}_{HL}$). The rest of the heat was conducted up through the Neoprene and surface roughness panels, where it was convected ($\dot{Q}_{CONV}$) or radiated ($\dot{Q}_{RAD}$) away from the surface. The resulting energy balance equation is given by Eq. (4.1).

$$\dot{Q}_{GEN} = \dot{Q}_{HL} + \dot{Q}_{RAD} + \dot{Q}_{CONV} \tag{4.1}$$

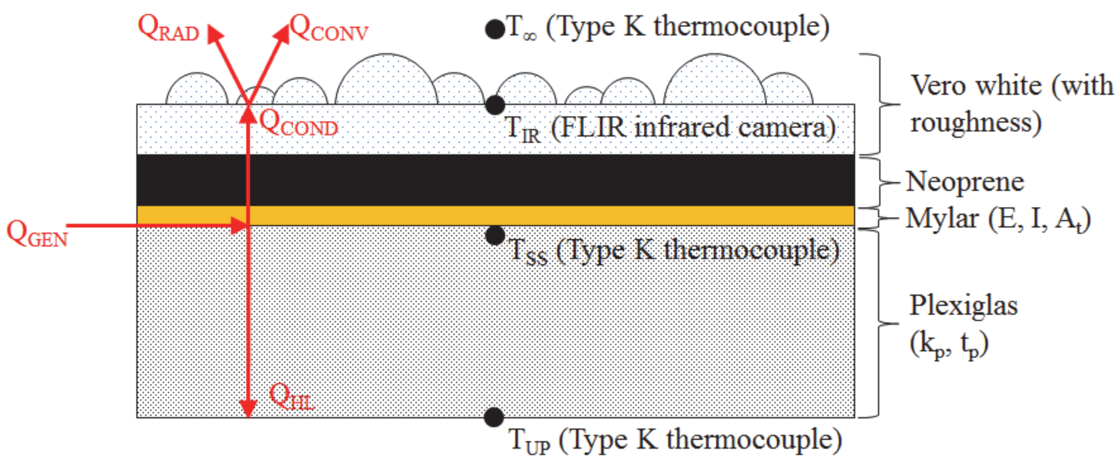

Figure 4.1: Heated section heat flow schematic (not to scale) [17]

Substituting Fourier's law of conduction for $\dot{Q}_{HL}$, Stefan-Boltzmann's law of radiation for $\dot{Q}_{RAD}$, Newton's law of cooling for $\dot{Q}_{CONV}$, and Ohm's law for power for $\dot{Q}_{GEN}$, dividing by pixel area, and solving for the convective heat transfer coefficient h, the resulting equation as derived by Shannon [17] is given by Eq. (4.2)).

$$h = \frac{\frac{EI}{A_t} - C_k \frac{k_p\left(T_{SS} - T_{UP}\right)}{t_p} - \varepsilon\sigma\left(T_{IR}^4 - T_\infty^4\right)}{T_{IR} - T_\infty} \tag{4.2}$$

Several assumptions were made during the derivation of Eq. (4.2). First, that lateral conduction in the spanwise direction was negligible. Second, that the Mylar film heaters generated a uniform heat flux [13]. And third, that the heat loss through the Plexiglas sub-plate was constant across each heated section, as measured by the middle thermocouple.

Eq. (4.2) shows a variable for the calibrated conduction parameters (C_k) from Walker [14]. This variable was added to adjust the term representing Fourier's law of conduction for each plate. When Walker obtained data for smooth-laminar and smooth-turbulent cases, the convective heat transfer coefficients for each case differed from the theoretical coefficients. Walker hypothesized that the embedded thermocouples, encased in epoxy, were affecting the Plexiglas thermal conductivity. Walker used a correction parameter for each test plate to match experimental results to theoretical predictions. Refer to Walker [14] for a more detailed description of how the conduction parameters were found. The values for the C_k parameter for each heated section are given in Table 4.1.

Table 4.1: Conduction parameter values [17]

Heated Section Number	C_k
0	0.90
1	0.90
2	1.05
3	1.10
4	1.05

Air Properties

The air properties affect measured convection coefficients, and multiple data sets cannot be directly compared unless atmospheric conditions are taken into account. Since data in these experiments was collected over multiple weeks, the air properties for each set were analyzed. This allowed the results to be directly compared using non-dimensional Stanton numbers. As mentioned in Chapter Three, an Omega zSeries zED-THPB-LCD atmospheric conditions monitor was used to track the air temperature, pressure, and relative humidity at the inlet of the wind tunnel. Using the same method for obtaining air properties as Tecson [13], Walker [14], and Shannon [17], a Mathcad program was used to calculate the air density, dynamic viscosity, specific heat, thermal conductivity, and Prandtl number for each data set. The Mathcad program was based on the International Association for the Properties of Water and Steam guidelines [73], Sutherland's law [23], and Wilke's equation for gas mixtures [74].

Thermocouple Calibration

The thermocouples were calibrated *in situ*. Based on the transmissivity experiments done by Walker [14], the IR camera measurements were considered accurate, and the thermocouples were calibrated to an averaged grouping of IR pixel temperatures. The equation for this is shown in Eq. (4.3).

$$T_{TC,calibrated} = T_{TC,test} - \left(T_{TC,cal} - \overline{T}_{IR,cal}\right) \tag{4.3}$$

To obtain the average temperature $\overline{T}_{IR,cal}$, a square group of pixels centered on each of the eight thermocouple pairs were averaged. Initially, the averaged center pixel groupings were the same 50x50 size as in Shannon [17] and Walker [14]. However, since the RealIce surface was not based on a repeating droplet pattern like the previous surfaces, it was hypothesized that the averaged pixel groupings needed to be expanded. Therefore, multiple pixel groupings of 50x50 (1" square), 100x100 (2" square), 150x150 (3" square), and the full 320x265 were all averaged to calibrate the thermocouples in each heated section. Each thermocouple was calibrated to the IR camera reading for that respective section. For example, the first three thermocouples in Section 0 were calibrated to the IR camera reading at Section 0.

The freestream thermocouple on the Pitot-static probe was sampled when data was taken at each of the heated sections, but the temperature changes were very small.

Following the methodology set by Walker [14], the freestream temperature was averaged at each of the five sections, as shown in Eq. (4.4)

$$T_{\infty} = \frac{T_{FS_0} + T_{FS_1} + T_{FS_2} + T_{FS_3} + T_{FS_4}}{5} \tag{4.4}$$

Smooth Surface Validation

To validate the derived convective heat transfer equation, Eq. (4.2), the heat transfer coefficients of smooth surface panels were compared to theoretical values of flat plate flow. Un-accelerated laminar and turbulent flows were validated by Walker [14], and accelerated laminar and turbulent flows were validated by Shannon [17]. The primary setup of this paper's experiments did not differ from the setup of Walker [14] or Shannon [17], except the new sawtooth leading-edge trip to initiate turbulent flow.

Uncertainty Analysis

Different roughness surfaces are compared using area averaged convective heat transfer coefficients. In previous experiments, an averaged 50x50 pixel area directly above each thermocouple pair was used for the temperature term required to calculate each convective heat transfer coefficient. However, this experiment compared coefficients which were calculated using averaged temperatures of not only 50x50 pixels (1" square), but also 100x100 (2" square), 150x150 (3" square), and the full 320x265. Again, this was done because the RealIce surface was the first surface studied at Baylor not based on a repeating droplet pattern, and is based on an ice accretion with varying thickness along the airfoil. Heat flux varies through different thicknesses, meaning that for a non-repeating droplet pattern the average temperatures in a 1" square might be significantly different from the average temperatures in a 3" square.

The uncertainties of each convective heat transfer coefficient were quantified in the same manner as Walker [14] and Shannon [17], by using the large sample size method of Coleman and Steele [75], which is built on the work of Kline and McClintock [76]. Table 4.2 lists a summary of the total uncertainty for each measured parameter used in the convective heat transfer equation, Eq. (4.2). The Plexiglas sub-plate thickness was accounted for with correction parameters in the conductive term, and so the uncertainty parameters were not assessed. Refer to Walker [14] for more details. The random uncertainty was found using Eq. (4.5).

$$U_{random} = \frac{t \cdot S}{\sqrt{N}} \tag{4.5}$$

In this equation, t is the statistical term known as the Student's t-value, S is the standard deviation, and N is the sample size. Refer to Shannon [17] for more details.

Table 4.2: Convective Heat Transfer Coefficient Measurement Uncertainty [17]

Variable	Total Uncertainty	Uncertainty Components
E	$\sqrt{U_{E,fixed}^2 + \left(\frac{tS_E}{\sqrt{N}}\right)^2}$	$U_{E,fixed} = 0.03\%\ E$ (sections 0 - 3) $U_{E,fixed} = 0.25\%\ E$ (section 4)
I	$\sqrt{U_{I,fixed}^2 + \left(\frac{tS_I}{\sqrt{N}}\right)^2}$	$U_{I,fixed} = 0.1$ A (section 0) $U_{I,fixed} = 0.05$ A (sections 1 - 3) $U_{I,fixed} = 2.5\%\ I$ (section 4)
A_t	$\sqrt{\left(U_{d,fixed} W_{ha}\right)^2 + \left(U_{d,fixed} L_{ha}\right)^2}$	$U_{d,fixed} = 1/32$ "
T_{IR}	$\sqrt{B_T^2 + \left(\frac{tS_{T_{IR}}}{\sqrt{N}}\right)^2}$	$B_T = 1.4$K

T_{SS}	$\sqrt{B_T^2 + \left(\frac{tS_{T_{IR}}}{\sqrt{N}}\right)_{cal}^2 + \left(\frac{tS_{T_{SS}}}{\sqrt{N}}\right)_{cal}^2 + \left(\frac{tS_{T_{SS}}}{\sqrt{N}}\right)_{test}^2}$	$B_T = 1.4\text{K}$
T_{UP}	$\sqrt{B_T^2 + \left(\frac{tS_{T_{IR}}}{\sqrt{N}}\right)_{cal}^2 + \left(\frac{tS_{T_{UP}}}{\sqrt{N}}\right)_{cal}^2 + \left(\frac{tS_{T_{UP}}}{\sqrt{N}}\right)_{test}^2}$	$B_T = 1.4\text{K}$
T_{∞}	$\sqrt{B_T^2 + \left(\frac{tS_{T_{IR}}}{\sqrt{N}}\right)_{cal}^2 + \left(\frac{tS_{T_{\infty}}}{\sqrt{N}}\right)_{test}^2}$	$B_T = 1.4\text{K}$

Velocity Boundary Layer Measurements

Probe Calibration

As mentioned in Chapter 3, the probe was calibrated by sampling multiple velocities at different angles in a rotary holder. Each wire of the x-array probe yielded a voltage corresponding to the pressures measured by the PCL-2A Pitot-static probe. The pressures were then converted to velocities using Bernoulli's principle, and labeled V_{meas}. The effective velocity experienced by each wire of the x-array probe was calculated using Eqs. (4.6) and (4.7)

$$V_{eff,1} = \sqrt{(V_{meas}\cos\alpha_1)^2 + \kappa^2 (V_{meas}\sin\alpha_1)^2} \tag{4.6}$$

$$V_{eff,2} = \sqrt{(V_{meas}\sin\alpha_2)^2 + \kappa^2 (V_{meas}\sin\alpha_2)^2} \tag{4.7}$$

In these equations, α is angle of the wire relative to the flow direction, and κ is the tangential velocity attenuation factor, which was 0.115 according to the manufacturer. The effective velocity was then plotted with the measured voltages of each wire, and each data set was curve fit with a fourth-order polynomial, as shown in Figure 4.2.

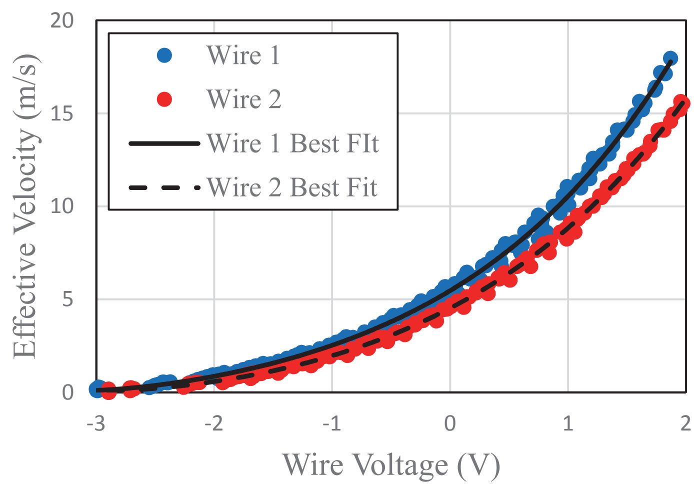

Figure 4.2: Hot-film probe calibration plot

Velocity Component Equations

Once each wire of the x-array probe was calibrated, the flow velocity components experienced by the probe were determined using the same method as Shannon [17], although with added calibration data points in the rotary probe holder every 5° instead of every 10°. First, the velocity flow normal and tangential to Wire 1 of the probe was determined using Eqs (4.8) and (4.9), respectively.

$$V_{N1} = \left(\frac{V_{eff,1}^2 - \kappa^2 V_{eff,2}^2}{1-\kappa^4} \right)^{1/2} \tag{4.8}$$

$$V_{T1} = \left(\frac{V_{eff,2}^2 - \kappa^2 V_{eff,1}^2}{1-\kappa^4} \right)^{1/2} \tag{4.9}$$

These velocities were then broken up into their x- and z-components relative to the probe using Eqs. (4.10) and (4.11), respectively.

$$u_i = \frac{V_{T1} + V_{N1}}{\sqrt{2}} \tag{4.10}$$

$$w_i = \frac{V_{T1} - V_{N1}}{\sqrt{2}} \tag{4.11}$$

At each of the 101 measurement stations, the 300,000 velocity component samples are averaged with Eqs. (4.12)-(4.13).

$$\bar{u} = \frac{1}{N}\sum_{i=1}^{N} u_i \tag{4.12}$$

$$\bar{w} = \frac{1}{N}\sum_{i=1}^{N} w_i \tag{4.13}$$

Additionally, the root-mean-square turbulent fluctuating velocity components are calculated using Eqs. (4.14)-(4.15).

$$u'_{RMS} = \sqrt{\frac{1}{N-1}\sum_{i=1}^{N}\left(u_i - \bar{u}\right)^2} \tag{4.14}$$

$$w'_{RMS} = \sqrt{\frac{1}{N-1}\sum_{i=1}^{N}\left(w_i - \bar{w}\right)^2} \tag{4.15}$$

CHAPTER FIVE

Results and Discussion

An evaluation of the laser-scanned RealIce surface using convective heat transfer tests and velocity boundary layer tests is presented here. Several of the older IRT and SSL surfaces are retested using the new sawtooth leading-edge trip, and the results are also presented. The results from the prior tests are helpful in validating several assertions about ice accretion on airfoils. The first hypothesis is that the RealIce surface correlates with the previous models, and the second is the hypothesis that the thin film liquid layer on the leading edge of the airfoil forces turbulent flow over the rest of the surface, causing some heat transfer enhancement. The heat transfer convection test results are presented first, followed by the results from the velocity boundary layer tests.

The data for the smooth laminar and smooth turbulent cases used in the Stanton number plots are taken from Walker [14] for the negligible freestream acceleration cases (i.e. without the ceiling insert) and from Shannon [17] for the accelerated cases (i.e. with the ceiling insert). The data for the 052996.04_x10_SSL and 113012.04_IRT cases, both with negligible freestream acceleration and with accelerated flow, were taken from Shannon [17], and are replicated here for comparison.

Convective Heat Transfer Results

Using the data reduction methods described in Chapter Four, the raw temperature readings from the IR camera were converted into convective heat transfer coefficient maps across each of the heated sections. Figures 5.1 and 5.2 display a comparison of two of the simulated roughness surfaces alongside the laser-scanned RealIce surface. The flow is accelerated using the ceiling insert, and forced turbulent using the new sawtooth trip. Figure 5.1 shows the results using plastic plates, whereas Figure 5.2 is of aluminum plates. However, Section 4 of both the 052996.04_x10_SSL and 113012.04_IRT surfaces is plastic in both figures, because an aluminum plate for that section was not made.

The 052996.04_x10_SSL surface exhibits much higher convection heat transfer coefficients than the other two surfaces due to the abrupt starting roughness in Section 1. The RealIce surface seems to match the 113012.04_IRT surface fairly closely, although the convection coefficients in Section 3 are slightly larger.

In addition to surface comparisons, three flow comparisons were done using the RealIce surface. Flow with negligible freestream acceleration was tested without the wind tunnel ceiling insert. Accelerated flow was created using the ceiling insert, and turbulent accelerated flow was created using both the ceiling insert and the new sawtooth leading-edge trip. Again, both plastic and aluminum surface panels were tested, and can be seen in both Figure 3 and Figure 4, respectively. Note that Figure 5.3 (c) and 5.4 (c) have been duplicated from Figure 5.1 (c) and 5.2 (c) respectively, for comparison purposes.

As expected, accelerating the air flow using the ceiling insert creates higher convective heat transfer values than flow with negligible acceleration. Accordingly, forcing turbulent flow using the sawtooth leading-edge trip creates even higher values. The local convective heat transfer coefficients and uncertainties for each test are presented in Table 5.1. For a complete set of all parameters and test data for each experimental case, see Appendix A.

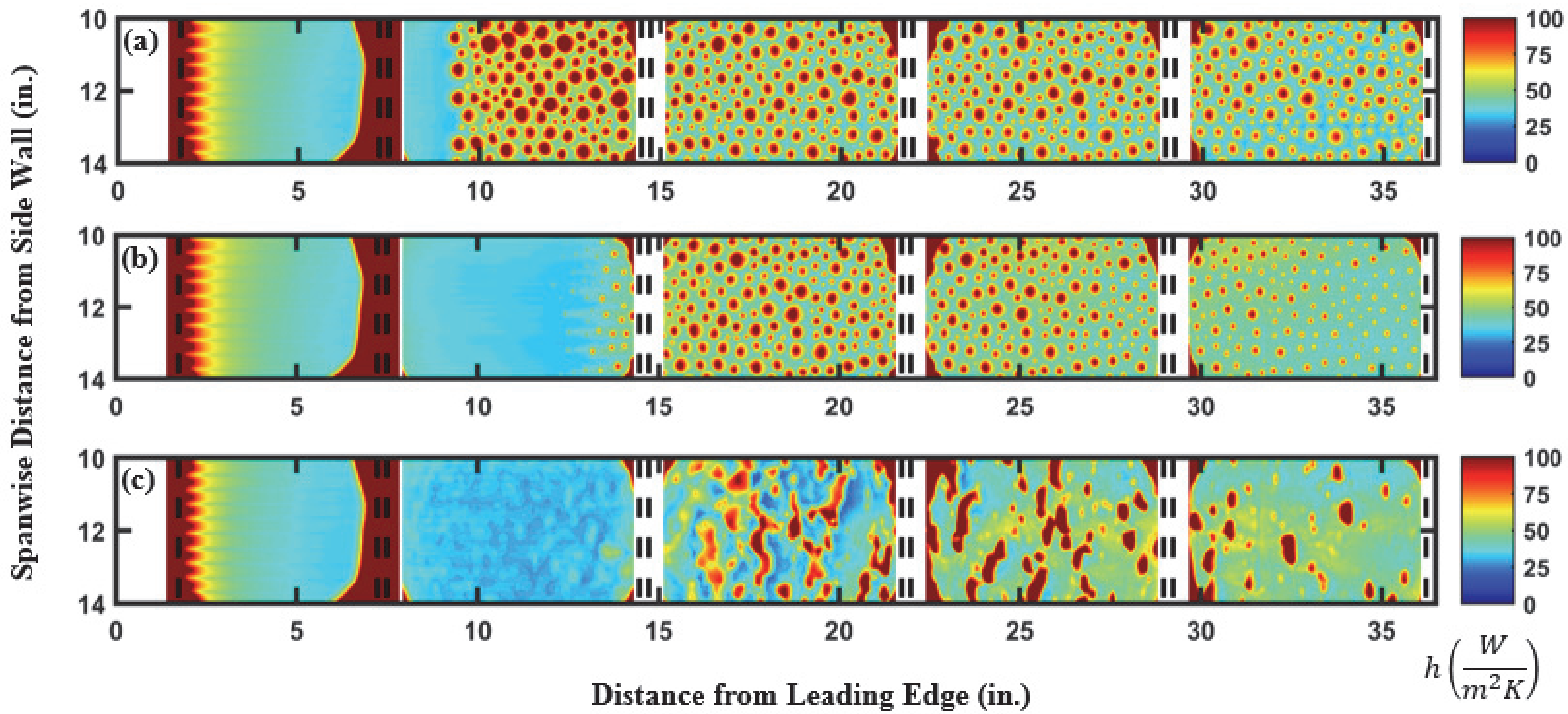

Figure 5.1: Convection coefficient contour maps of turbulent, accelerated flow over plastic surfaces of a) 052996.04_x10_SSL_cones, b) 113012.04_IRT_cones, and c) 113012.04_RealIce (flow is from left to right)

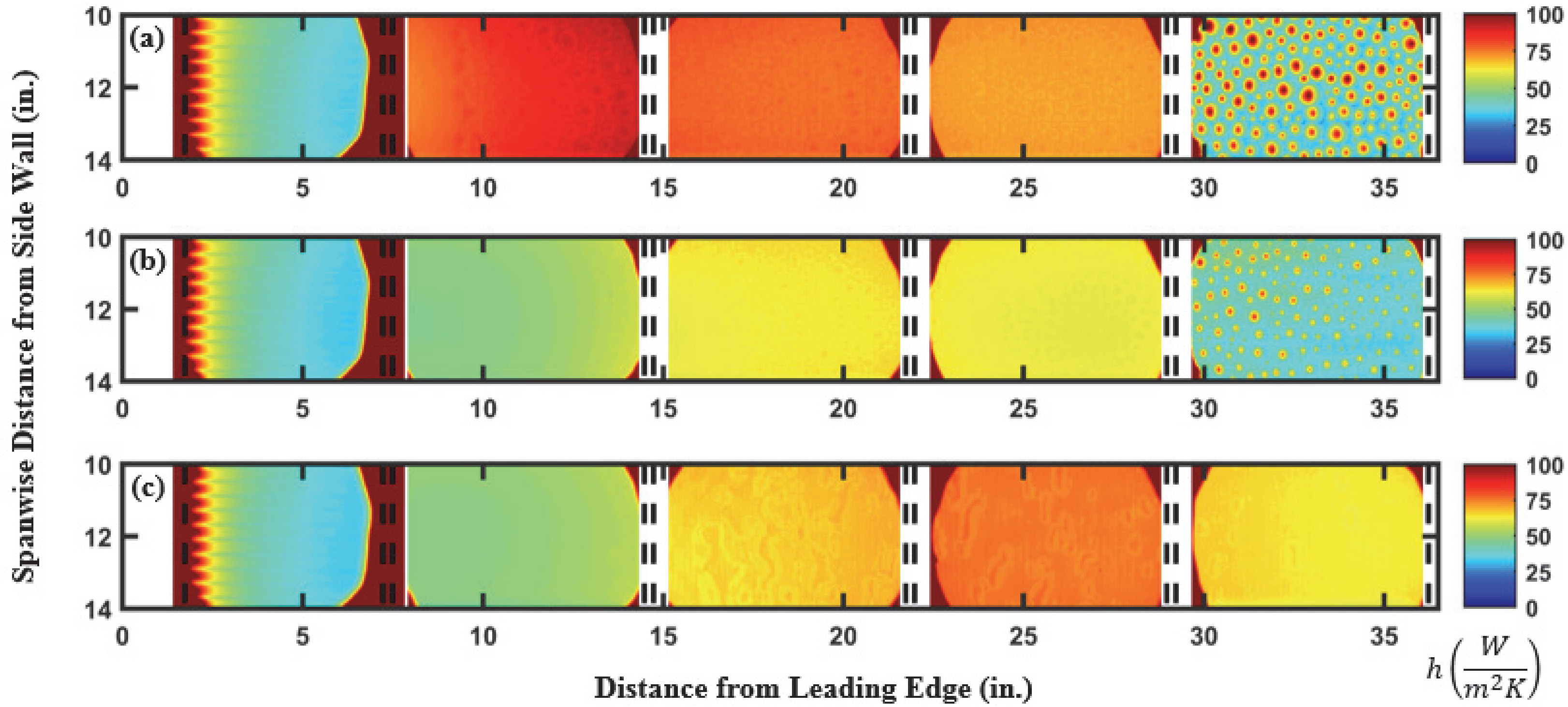

Figure 5.2: Convection coefficient contour maps of turbulent, accelerated flow over aluminum surfaces of a) 052996.04_x10_SSL_cones, b) 113012.04_IRT_cones, and c) 113012.04_RealIce (flow is from left to right) (note that Section 4 of (a) and (b) are both plastic)

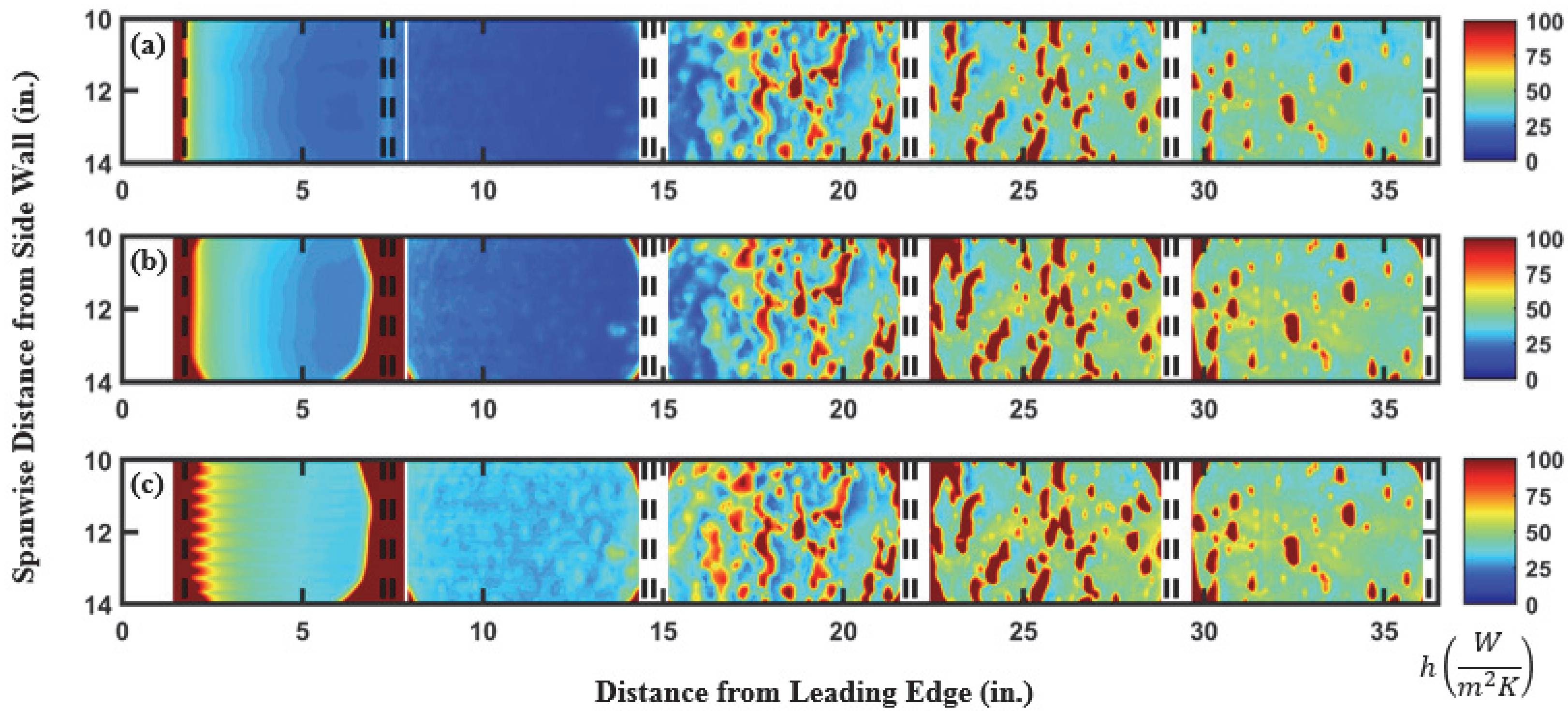

Figure 5.3: Convection coefficient contour maps of plastic 113012.04_RealIce surfaces in a) flow with negligible freestream acceleration, b) accelerated flow, and c) turbulent accelerated flow (flow is from left to right)

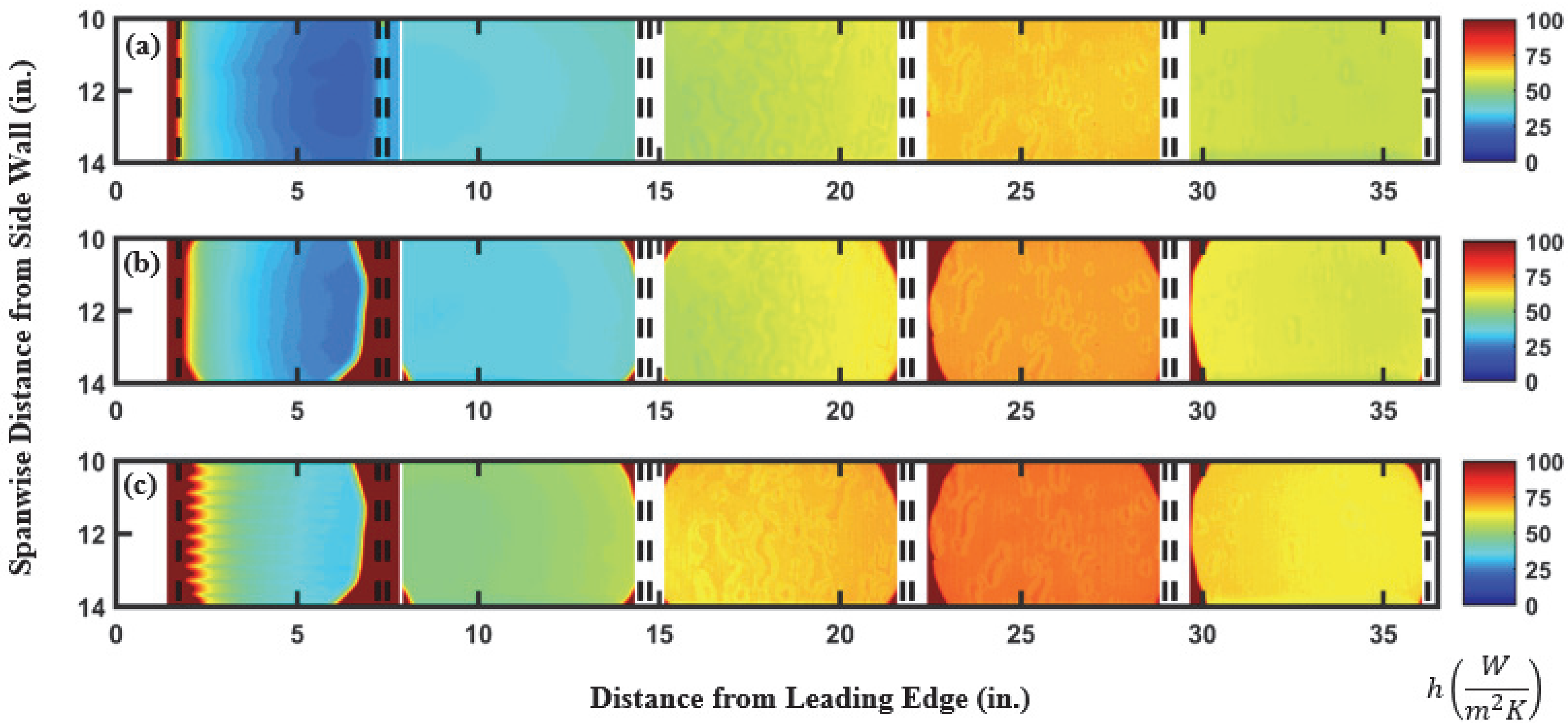

Figure 5.4: Convection coefficient contour maps of aluminum 113012.04_RealIce surfaces in a) flow with negligible freestream acceleration, b) accelerated flow, and c) turbulent accelerated flow (flow is from left to right)

Table 5.1: Convective heat transfer coefficients for reported cases (units of $W/m^2 \cdot K$)

Case	0a	0b	0c	1a	1b	2	3	4
052996.04_x10_SSL								
Accelerated, Tripped								
Plastic	51.75 ± 1.70	40.45 ± 2.12	35.00 ± 2.13	41.03 ± 2.48	62.27 ± 5.84	58.51 ± 3.98	55.73 ± 4.57	50.41 ± 3.20
Aluminum	51.32 ± 1.66	40.21 ± 2.11	35.11 ± 2.12	73.09 ± 3.13	77.07 ± 3.81	76.10 ± 3.48	70.64 ± 3.84	49.25 ± 3.17
113012.04_IRT								
Accelerated, Tripped								
Plastic	54.32 ± 1.28	42.39 ± 2.04	36.67 ± 2.12	32.37 ± 1.48	29.18 ± 1.36	59.07 ± 3.92	54.87 ± 4.70	46.34 ± 2.71
Aluminum	48.22 ± 1.92	38.30 ± 2.13	33.54 ± 2.10	43.05 ± 1.28	43.92 ± 1.43	62.90 ± 2.77	61.00 ± 3.35	41.45 ± 2.44
113012.04_RealIce								
Un-accelerated								
Plastic	30.37 ± 2.10	24.31 ± 1.88	21.88 ± 1.77	17.67 ± 0.21	13.99 ± 0.20	47.32 ± 3.51	55.67 ± 4.23	47.21 ± 3.09
Aluminum	30.06 ± 2.08	24.23 ± 1.87	21.64 ± 1.74	33.39 ± 0.64	32.64 ± 0.81	56.46 ± 2.50	66.64 ± 3.36	56.81 ± 2.69
Accelerated								
Plastic	37.04 ± 2.20	29.05 ± 2.03	25.33 ± 1.91	20.92 ± 0.45	17.62 ± 0.28	46.91 ± 3.34	57.77 ± 4.25	53.54 ± 3.51
Aluminum	36.04 ± 2.18	28.37 ± 2.03	24.90 ± 1.90	32.05 ± 0.64	31.22 ± 0.75	58.69 ± 2.61	70.56 ± 3.65	59.68 ± 2.84
Accelerated, Tripped								
Plastic	48.34 ± 2.03	38.05 ± 2.18	33.69 ± 2.14	29.05 ± 0.99	26.70 ± 0.91	50.51 ± 3.72	60.42 ± 4.56	54.03 ± 3.54
Aluminum	48.77 ± 1.95	38.43 ± 2.16	34.01 ± 2.13	44.79 ± 1.36	44.10 ± 1.56	66.21 ± 3.09	74.88 ± 4.00	63.45 ± 3.04
Smooth Laminar								
Accelerated [17]	37.75 ± 2.00	30.48 ± 2.05	26.54 ± 1.97	21.06 ± 0.59	18.49 ± 0.50	14.05 ± 0.84	12.01 ± 0.84	7.92 ± 0.79
Un-accelerated [14]	26.67 ± 1.98	22.10 ± 1.87	19.70 ± 1.78	15.38 ± 0.50	14.01 ± 0.40	11.03 ± 0.83	9.34 ± 0.85	8.98 ± 0.83
Smooth Turbulent								
Accelerated [17]	92.39 ± 7.30	57.60 ± 0.41	47.36 ± 1.84	37.34 ± 1.97	34.00 ± 1.82	33.35 ± 1.76	31.78 ± 2.05	29.94 ± 1.92
Un-accelerated [14]	86.79 ± 5.14	66.13 ± 2.66	54.22 ± 1.16	40.59 ± 2.21	36.58 ± 2.07	30.23 ± 1.54	28.25 ± 1.86	25.35 ± 1.63

It is difficult to make specific comparisons using the color maps of the heated sections, so following the example of Walker [14] and Shannon [17], Stanton number plots were generated.

Localized Stanton numbers were evaluated using the average convective heat transfer coefficient of a 1” square (50x50 pixels) area centered on each of the eight thermocouple pairs in the Plexiglas sub-plate. This allowed for easier comparison between surfaces and flow conditions. The Stanton numbers are plotted against Reynolds numbers. Because the flow is steady and the fluid properties are taken into account for each test, the only significantly changing variable in Reynolds number is the length down the streamline. Using dimensionless variables like the Stanton number and Reynolds number allows for generality and scalability.

Each Stanton number chart includes the theoretical laminar and turbulent correlations mentioned in Chapter Two. Eqs. (2.15) and (2.16), respectively, were used for the theoretical laminar and turbulent correlations in flow with negligible acceleration. Eqs. (2.17) and (2.18), respectively, were used for the theoretical laminar and turbulent correlations in accelerating flow. Following the example from Tecson [13], the unheated bullnose at the leading edge of Section 0 necessitated that Eqs (2.15)-(2.18) be evaluated using ξ = 1.7285". In Figure 5.5, smooth laminar data points from Walker [14] are shown for reference, although the validity of the smooth laminar sections has already been shown in previous work [14]. Figure 5.5 displays the results for flow with negligible acceleration, Figure 5.6 shows the accelerated results, including tests using the new leading edge trip.

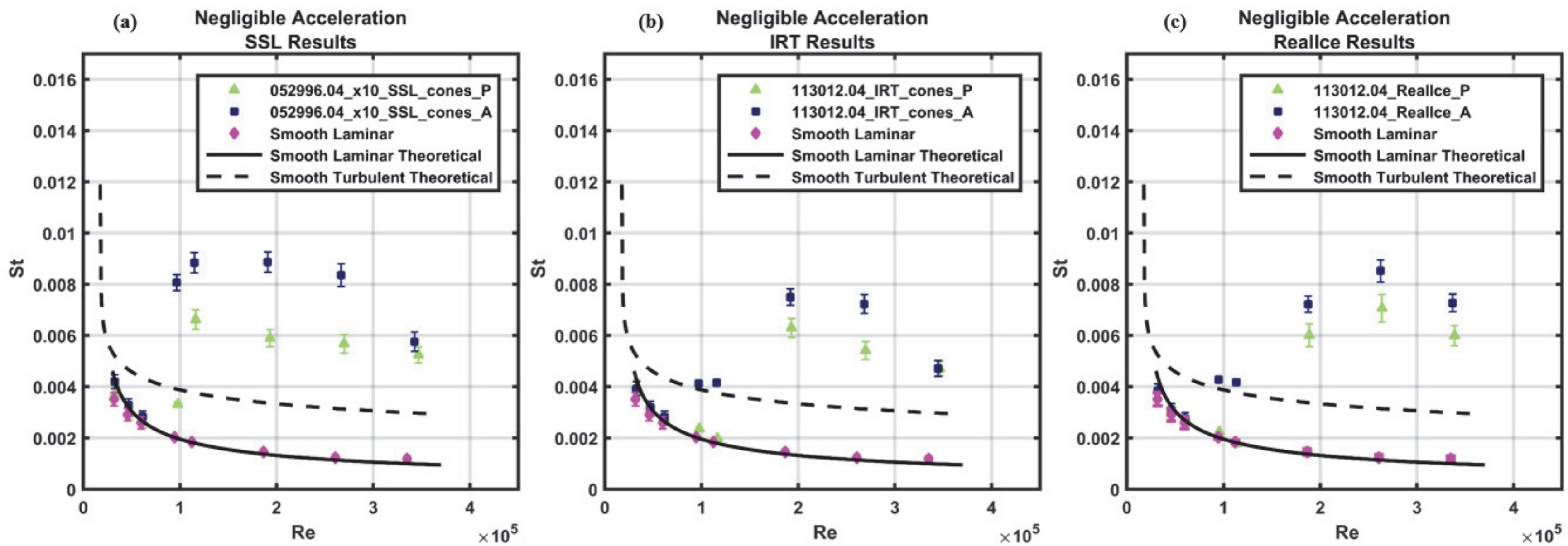

Figure 5.5: Local Stanton number measurements for flow with negligible acceleration over a) 052996.04_x10_SSL surfaces, b) 113012.04_IRT surfaces, and c) 113012.04_RealIce surfaces (flow is from left to right). Note that both the SSL and IRT data sets here were taken from Shannon [17], and are replicated here for comparison alongside the RealIce surface.

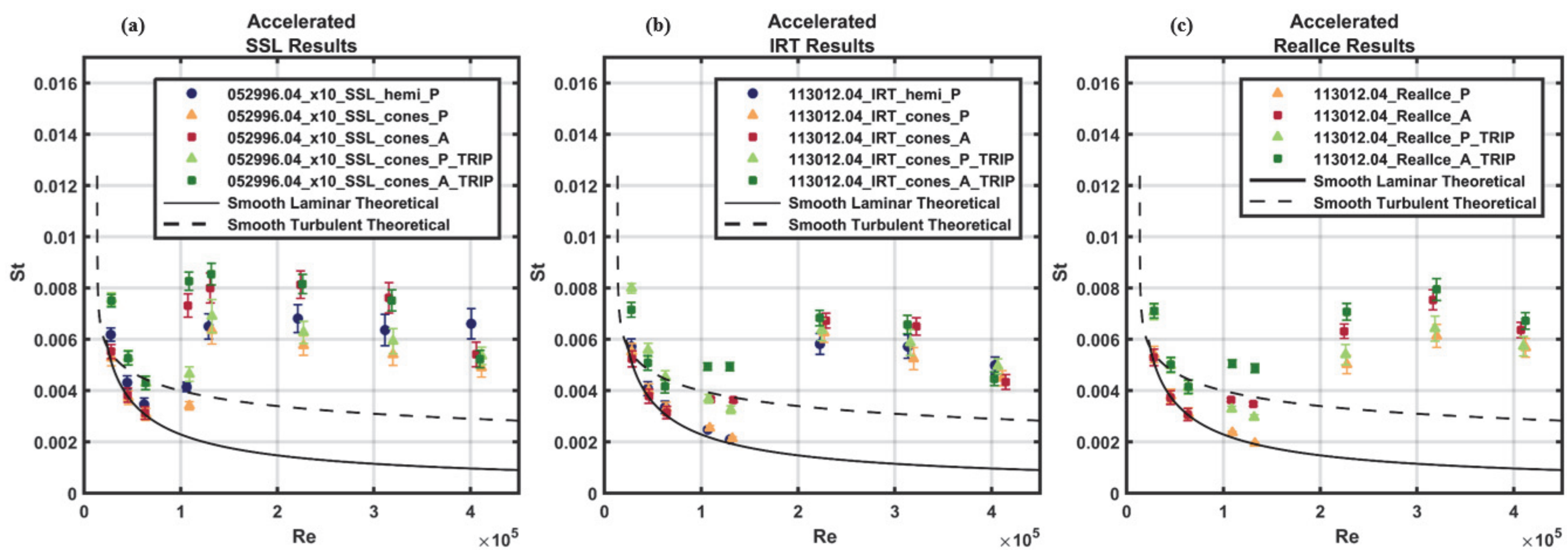

Figure 5.6: Local Stanton number measurements for accelerated flow over a) 052996.04_x10_SSL surfaces, b) 113012.04_IRT surfaces, and c) 113012.04_RealIce surfaces (flow is from left to right). Note that both hemisphere data sets, as well as both untripped SSL and IRT data sets were taken from Shannon [17], and are replicated here for comparison alongside the RealIce surface.

Figure 5.5 (a) and (b) displays the flow with negligible acceleration over the 052996.04_x10_SSL and 113012.04_IRT data sets from Shannon [17], and the main difference between the two is in the smooth-to-rough transition region between Heated Sections 0 and 1. The surfaces share very similar characteristics downstream of Section 1. The RealIce surface in Figure 5.5 (c), on the other hand, is only similar to the 113012.04_IRT surface up to Section 1. The measured Stanton numbers increase in Section 2, continue increasing to Section 3, and decrease in Section 4. The 113012.04_IRT surface has its maximum Stanton number in Section 2. Of course, in all cases, the aluminum plates exhibit higher Stanton numbers than the plastic due to the increased thermal conductivity of the material. In the turbulent section after roughness starts, the aluminum RealIce surface shows Stanton numbers which are up to 20% higher than the plastic Realice surface.

Figure 5.6 (a) and (b) displays accelerated flow data sets from Shannon [17], not only of the plastic and aluminum cones, but also the plastic hemispheres. These are compared with the newer surface tests using the leading edge trip, as well as the RealIce surface tests in Figure 5.6 (c). Comparing Figure 5.6 to Figure 5.5 confirms previous assertions that accelerating flow over these rough surfaces yields marginally lower Stanton numbers than flows with negligible acceleration. This is explained by the fact that a favorable pressure gradient and gradual increase in roughness properties does not create as much turbulence near the roughness, resulting in lower Stanton numbers. Even though the actual convective heat transfer enhancement might increase, the velocity in the denominator of the Stanton number equation has also increased, and the net result is a slightly lower Stanton number.

The first heated section of each surface shown in Figure 5.6 tend to follow either the theoretical smooth laminar or smooth turbulent curves, until the flow reaches the roughness which begins in the Heated Section 1. In these figures, it is apparent that when the flow is forced turbulent by the leading edge trip, the flow over the smooth heated sections results in higher Stanton numbers. However, once the flow reaches the roughness in the third heated section, there is no statistical difference between the measured Stanton numbers for the untripped and tripped flows. The only exception to this is in the aluminum RealIce case, where the third heated section yields a measurably higher Stanton number in the tripped flow case. The uncertainty bars at the location for the aluminum RealIce and the tripped aluminum RealIce cases do not overlap. Although this is measurable and statistically different, the uncertainty bars are close enough that this difference is not deemed substantial due to the fact that the untripped flow is likely still transitioning to turbulence. Because of the minimal differences in Stanton numbers between tripped and untripped cases, these results suggest that forcing turbulent flow near the stagnation point will not significantly change the Stanton number once the flow reaches surface roughness.

Figure 5.6 also allows visual comparison between the RealIce, cones, and hemispheres cases for both SSL and IRT surfaces. Of course, the RealIce case more closely matches the IRT surface because of the gradually increasing roughness. However, both the SSL and IRT cases follow a trend of increased Stanton numbers upon reaching surface roughness, followed by a slow decrease in Stanton numbers. The RealIce case differs from this trend. The Stanton numbers increase upon reaching surface roughness, and then continue with a slight increase in Section 3 before finally decreasing in the final heated section. A possible explanation for this tendency is due to the roughness element dispersion. The upstream roughness elements are very large and tightly packed together. Downstream, roughness elements gradually spread out before diminishing. There is an optimal sparseness which allows air flow to interact with large roughness elements while at the same time the roughness elements are not so tightly packed as to inhibit surface-level flow between elements. This sparseness between elements, which isn't as pronounced in the SSL or IRT surfaces, is suspected to enhance the Stanton number in the Section 3 of the RealIce surface.

For a side-by-side comparison of two IRT cases (both hemisphere and cone) and the untripped RealIce cases, see Figure 5.7. The aluminum RealIce surface is also included, although the higher thermal conductivity results in larger Stanton numbers.

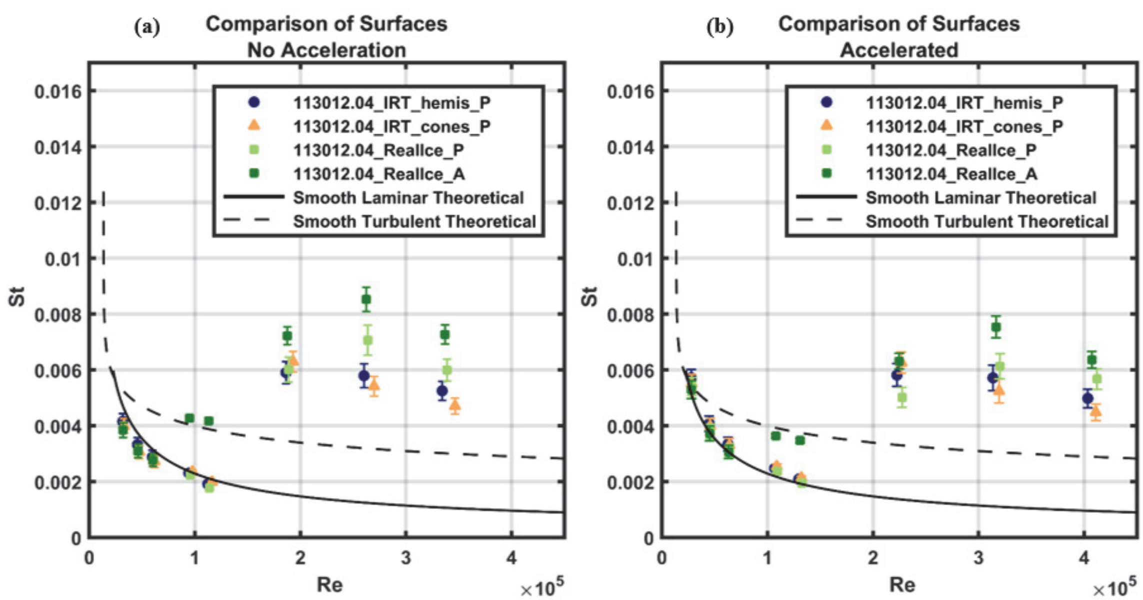

Figure 5.7: Local Stanton number measurements presented for surface comparison in a) flow with negligible acceleration, and b) accelerated flow (flow is from left to right). Note that both the 113012.04_IRT hemisphere and cone data sets were taken from Shannon [17], and are replicated here for comparison alongside the RealIce surface.

These comparisons show that in both flow cases, plastic hemispheres are not statistically different from plastic cones because the uncertainty bars for each of the measured Stanton numbers overlap. However, the plastic RealIce surface displays different enhancement trends than the two IRT cases. In Figure 5.7 (a), the plastic RealIce surface is similar to the two IRT surfaces until Section 3, where the Stanton number is significantly higher than the other two surfaces, likely due to the sparseness between the RealIce roughness elements. . In Figure 5.7 (b), the plastic RealIce surface is only similar to the two IRT surfaces until Section 1. Heated Section 2 shows a lower Stanton number than the IRT surfaces, Section 3 shows the three surfaces are statistically similar, and Section 4 shows the RealIce surface has a significantly larger Stanton number than the other surfaces.

One further comparison was made regarding the Stanton number plots. As previously mentioned in Chapter 4, the Stanton numbers are calculated using area averaged convective heat transfer coefficients. Prior experiments used a 50x50 pixels grid (1" square) centered directly above each thermocouple pair. Because the RealIce surface was not based on a repeating droplet pattern, it was not initially obvious whether or not the size of the area averaged heat transfer coefficients would significantly affect the data. Therefore, the coefficients were recalculated using 100x100 pixels (2" square), 150x150 pixels (3" square), and the full range of the IR camera's 320x265 pixels. These recalculated Stanton numbers are presented in Figure 5.8 (a) through (d).

The results from this comparison show that the data from the plastic surfaces shifts slightly in each case. However, the aluminum surface data in (a) through (c) is almost completely unchanged, and only increases marginally when the full 320x265 set is averaged. This means that for the aluminum test surfaces changing the size of the area averaged grid of heat transfer coefficients is largely not a factor in the Stanton number results. The plastic test surfaces might shift slightly, but will not be statistically different.

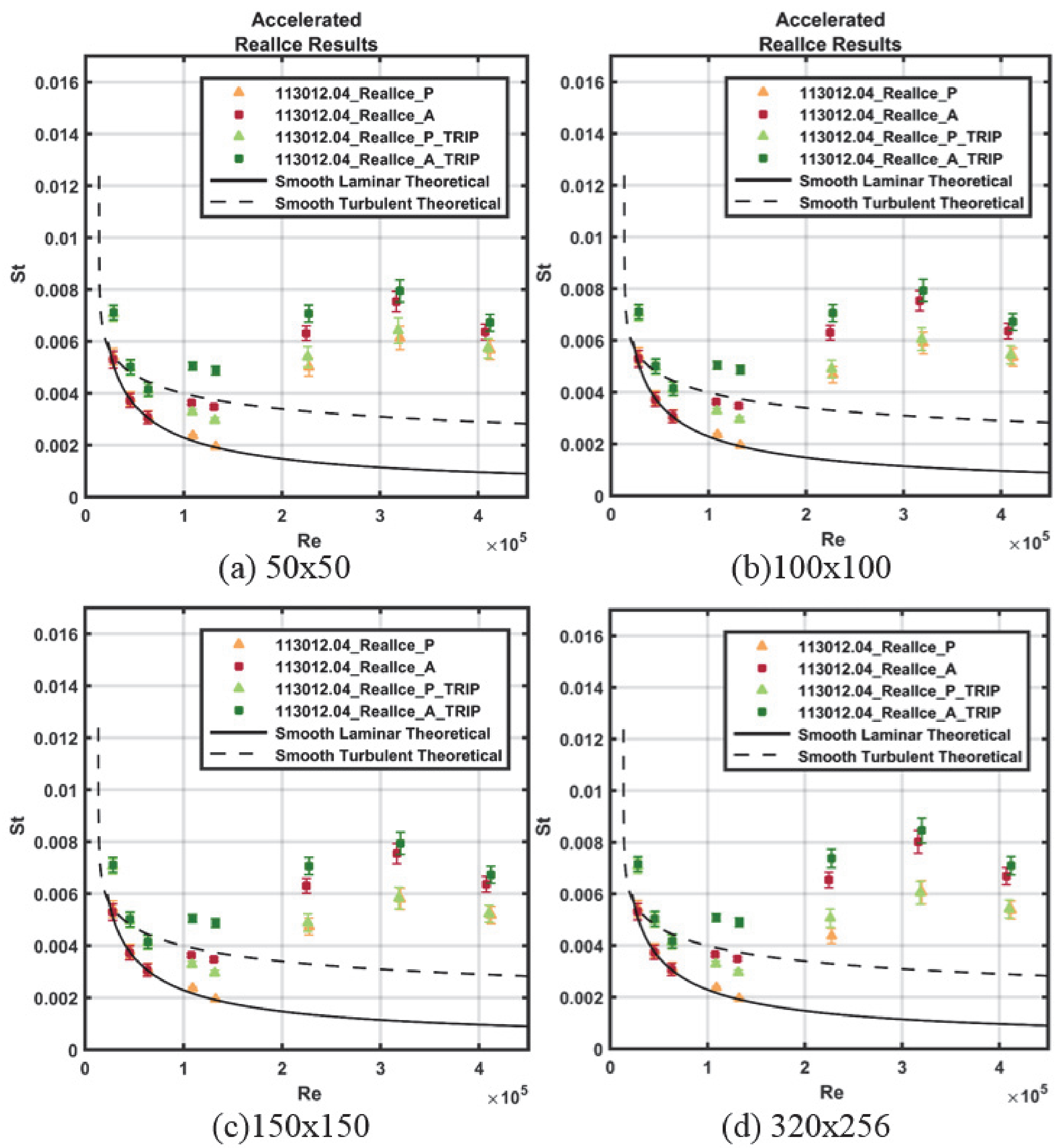

Figure 5.8: Local Stanton number measurements for accelerated and tripped flow over 113012.04_RealIce surfaces, where the locally averaged convection coefficients were taken from a centered group of a) 50x50 pixels, b) 100x100 pixels, c) 150x150 pixels, and d) 320x256 pixels, which is the entire field of the IR camera (flow is from left to right)

Velocity Boundary Layer Results

At the center of each surface panel along the heated sections, velocity boundary layer measurements were taken. Five cases were tested: tripped IRT cones, tripped IRT hemispheres, and three flow cases for the RealIce surface. These can be seen in Figures 5.9 and 5.10, respectively. In most of these cases, the boundary layers were observable and developed as expected. However, in Figure 5.10, due to elements preventing the hotwire probe from reaching the actual surface of the test plate in Heated Sections 2 and 3, the boundary layers were not fully measurable.

Figure 5.9 compares the accelerated flow cases of the IRT cones and IRT hemisphere surfaces, respectively. The velocity profiles show minor disturbances caused by the roughness elements, although there are also disturbances at Section 0 and Section 1, which are both upstream of the beginning of surface roughness. These disturbances are also evident with the RealIce surfaces, except in the negligible flow acceleration case in Figure 5.10 (a). These figures are comparable to the negligible flow acceleration cases and the accelerated flow results from Shannon [17], and shows that the RealIce boundary layer formation does not differ significantly from the other surfaces, even when the leading edge trip forces early turbulent flow.

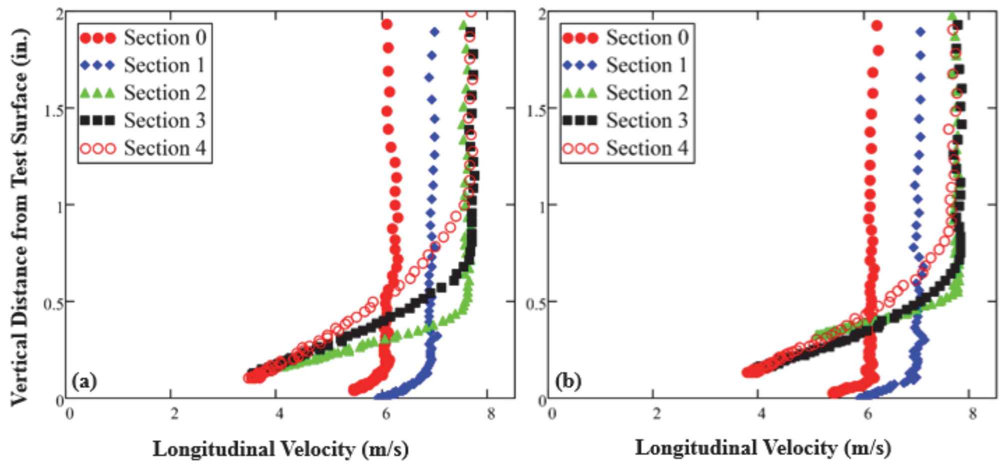

Figure 5.9: Velocity profiles at the center of the heated sections with accelerated flow and a leading edge trip for a) 113012.04_IRT cones and b) 113012.04_IRT hemispheres.

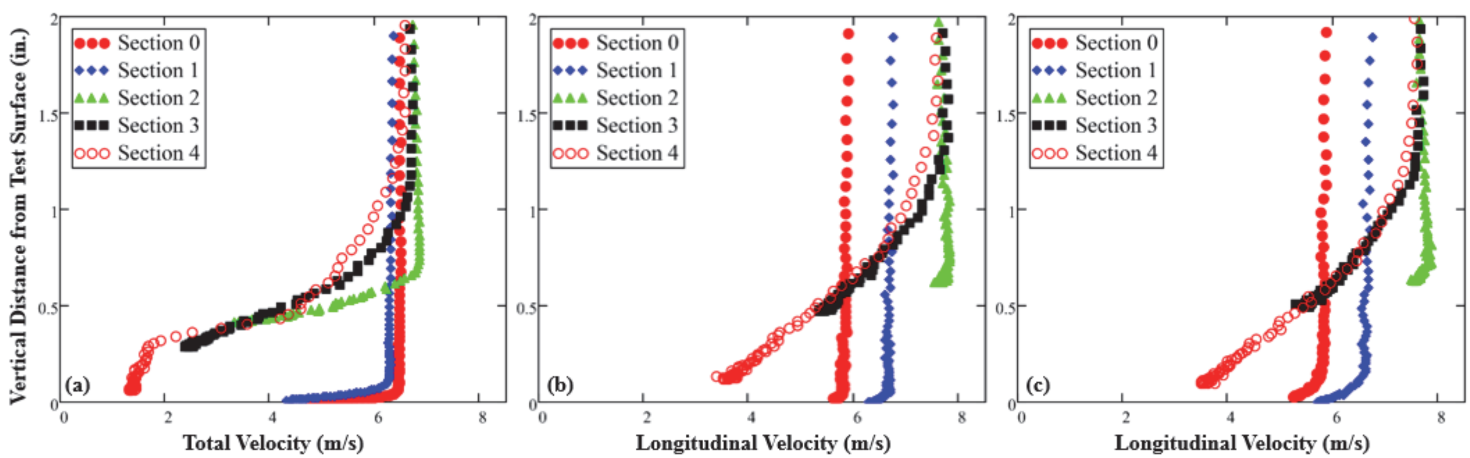

Figure 5.10: Velocity profiles at the center of the heated sections for the 113012.04_RealIce surface in the a) negligible flow acceleration case, b) accelerated flow case, and c) accelerated and tripped flow case

CHAPTER SIX

Conclusions

Summary of Work

This study investigated a new surface of laser scanned real ice roughness. Two materials were used to manufacture the surface so that data for two thermal conductivities could be obtained. Convective heat transfer measurements were obtained for the two surface scenarios. The resulting convection measurements were compared to previously measured convection coefficients from surfaces with simulated roughness elements. A new sawtooth leading edge trip was made to force turbulent flow downstream, and this trip was tested with the real ice surface, as well as with two surfaces with Langrangian droplet simulated elements used in previous studies. The primary findings were:

- The 103012.04_RealIce surfaces differed from the previous 052996.04_x10_SSL surface and the 113012.04_IRT surfaces in all flow cases. The main difference being that for the 103012.04_RealIce surface, the Stanton number continued to increase after the smooth-to-rough transition to a point, and then decreased downstream. The increased in enhancement of the real ice roughness is likely caused by the lower roughness element density of the real ice surface compared to the surfaces with simulated roughness elements.
- The differences in convection measurements between ABS plastic and machined aluminum 103012.04_RealIce surfaces were measurable, with the aluminum

showing roughly 20% higher Stanton numbers than the plastic in the last three heated sections

- The tripped cases for all surfaces showed no statistical differences compared to the untripped cases once roughness had induced turbulence. In the heated sections where the untripped cases were transitioning to turbulence, the Stanton numbers for the tripped cases were only slightly larger than the untripped cases. The small changes in convective heat transfer suggest that the effects of the liquid film or droplet interactions at the leading edge are not significant in affecting the convection downstream of the location of maximum ice roughness.

Future Work

Future research efforts will continue the effort to gather data about real ice accretions on aircraft surfaces. Gathering more data will allow more cases for LEWICE to draw from, and thus the characterization of convective enhancement will be improved. The efforts of this investigation focused on one specific set of flow conditions on a straight, NACA 0012, with zero angle of attack at a set ice accretion exposure time. Improvements in LEWICE may be achieved by 1) testing more surfaces of ice roughness acquired in different icing conditions, 2) testing surfaces with ice accretion roughness from airfoils at different angles of attack, and 3) testing surfaces with ice accretion roughness from tests of various lengths of ice accretion exposure.

APPENDIX

APPENDIX A

Test Data

This appendix provides the test data for the all of the 113012.04_RealIce cases, as well as the accelerated and tripped 113012.04_IRT_cones and 052996.04_x10_SSL_cones cases.

Table A.1: Un-accelerated 113012.04_RealIce plastic case

Parameter	0a	0b	0c	1a	1b	2	3	4
x (in)	3.10	4.48	5.85	9.23	10.98	18.23	25.48	32.73
A_t (in^2)	35.06	35.06	35.06	44.62	44.62	44.62	44.62	44.62
ε	0.95	0.95	0.95	0.95	0.95	0.95	0.95	0.95
σ (W/m^2K^4)	5.67e-8	5.67e-8	5.67e-8	5.67e-8	5.67e-8	5.67e-8	5.67e-8	5.67e-8
t_p (in)	0.72	0.72	0.72	0.72	0.72	0.72	0.72	0.72
C_k	0.90	0.90	0.90	0.90	0.90	1.05	1.10	1.05
E (V)	5.98	5.98	5.98	5.89	5.89	5.86	6.26	6.18
I (A)	2.06	2.06	2.06	2.61	2.61	2.60	2.72	2.55
k_p (W/mK)	0.205	0.205	0.205	0.205	0.205	0.205	0.205	0.205
T_{SS} (K)	316.92	317.24	318.03	320.02	322.27	318.31	316.40	316.26
T_{UP} (K)	300.12	300.53	301.23	301.00	300.98	301.50	301.59	301.50
T_∞ (K)	295.45	295.45	295.45	295.45	295.45	295.45	295.45	295.45
T_{IR} (K)	305.83	307.92	308.96	309.92	311.40	301.69	302.10	302.52
h (W/m^2K)	30.37 ± 2.10	24.31 ± 1.88	21.88 ± 1.77	17.67 ± 0.21	13.99 ± 0.20	47.32 ± 3.51	55.67 ± 4.23	47.21 ± 3.09

Table A.2: Accelerated 113012.04_RealIce plastic case

Parameter	0a	0b	0c	1a	1b	2	3	4
x (in)	3.10	4.48	5.85	9.23	10.98	18.23	25.48	32.73
A_t (in^2)	35.06	35.06	35.06	44.62	44.62	44.62	44.62	44.62
ε	0.95	0.95	0.95	0.95	0.95	0.95	0.95	0.95
σ (W/m^2K^4)	5.67E-08	5.67E-08	5.67E-08	5.67E-08	5.67E-08	5.67E-08	5.67E-08	5.67E-08
t_p (in)	0.72	0.72	0.72	0.72	0.72	0.72	0.72	0.72
C_k	0.90	0.90	0.90	0.90	0.90	1.05	1.10	1.05
E (V)	6.00	6.00	6.00	5.87	5.87	5.88	6.27	6.14
I (A)	2.09	2.09	2.09	2.63	2.63	2.59	2.72	2.57
k_p (W/mK)	0.205	0.205	0.205	0.205	0.205	0.205	0.205	0.205
T_{SS} (K)	314.31	315.30	316.45	317.92	320.03	317.41	315.09	314.67
T_{UP} (K)	297.53	298.31	298.91	299.71	300.23	301.10	300.98	300.83
T_∞ (K)	295.32	295.32	295.32	295.32	295.32	295.32	295.32	295.32
T_{IR} (K)	304.30	306.28	307.40	308.47	309.61	301.73	301.90	301.81
h (W/m^2K)	37.04 ± 2.20	29.05 ± 2.03	25.33 ± 1.91	20.92 ± 0.45	17.62 ± 0.28	46.91 ± 3.34	57.77 ± 4.25	53.54 ± 3.51

Table A.3: Accelerated and tripped 113012.04_RealIce plastic case

Parameter	0a	0b	0c	1a	1b	2	3	4
x (in)	3.10	4.48	5.85	9.23	10.98	18.23	25.48	32.73
A_t (in^2)	35.06	35.06	35.06	44.62	44.62	44.62	44.62	44.62
ε	0.95	0.95	0.95	0.95	0.95	0.95	0.95	0.95
σ (W/m^{2}K^4)	5.67E-08	5.67E-08	5.67E-08	5.67E-08	5.67E-08	5.67E-08	5.67E-08	5.67E-08
t_p (in)	0.72	0.72	0.72	0.72	0.72	0.72	0.72	0.72
C_k	0.90	0.90	0.90	0.90	0.90	1.05	1.10	1.05
E (V)	5.97	5.97	5.97	5.87	5.87	5.89	6.28	6.15
I (A)	2.09	2.09	2.09	2.64	2.64	2.60	2.72	2.57
k_p (W/mK)	0.205	0.205	0.205	0.205	0.205	0.205	0.205	0.205
T_{SS} (K)	313.01	314.72	315.82	315.97	317.37	317.24	315.06	314.71
T_{UP} (K)	297.07	297.85	298.58	299.36	299.62	300.80	300.87	300.85
T_∞ (K)	295.26	295.26	295.26	295.26	295.26	295.26	295.26	295.26
T_{IR} (K)	302.47	303.94	304.80	305.89	306.30	301.27	301.61	301.72
h (W/m^{2}K)	48.34 ± 2.03	38.05 ± 2.18	33.69 ± 2.14	29.05 ± 0.99	26.70 ± 0.91	50.51 ± 3.72	60.42 ± 4.56	54.03 ± 3.54

Table A.4: Un-accelerated 113012.04_RealIce aluminum case

Parameter	0a	0b	0c	1a	1b	2	3	4
x (in)	3.10	4.48	5.85	9.23	10.98	18.23	25.48	32.73
A_t (in^2)	35.06	35.06	35.06	44.62	44.62	44.62	44.62	44.62
ε	0.95	0.95	0.95	0.95	0.95	0.95	0.95	0.95
σ (W/m^2K^4)	5.67E-08	5.67E-08	5.67E-08	5.67E-08	5.67E-08	5.67E-08	5.67E-08	5.67E-08
t_p (in)	0.72	0.72	0.72	0.72	0.72	0.72	0.72	0.72
C_k	0.90	0.90	0.90	0.90	0.90	1.05	1.10	1.05
E (V)	6.00	6.00	6.00	5.87	5.87	5.85	6.20	6.09
I (A)	2.06	2.06	2.06	2.65	2.65	2.60	2.75	2.61
k_p (W/mK)	0.205	0.205	0.205	0.205	0.205	0.205	0.205	0.205
T_{SS} (K)	316.84	317.13	317.47	309.97	311.61	307.31	306.95	307.32
T_{UP} (K)	300.13	300.51	301.10	299.10	299.05	298.54	298.71	298.77
T_∞ (K)	295.09	295.09	295.09	295.09	295.09	295.09	295.09	295.09
T_{IR} (K)	305.64	307.69	308.95	306.05	305.83	301.93	301.88	302.29
h (W/m^2K)	30.06 ± 2.08	24.23 ± 1.87	21.64 ± 1.74	33.39 ± 0.64	32.64 ± 0.81	56.46 ± 2.50	66.64 ± 3.36	56.81 ± 2.69

Table A.5: Accelerated 113012.04_RealIce aluminum case

Parameter	0a	0b	0c	1a	1b	2	3	4
x (in)	3.10	4.48	5.85	9.23	10.98	18.23	25.48	32.73
A_t (in^2)	35.06	35.06	35.06	44.62	44.62	44.62	44.62	44.62
ε	0.95	0.95	0.95	0.95	0.95	0.95	0.95	0.95
σ (W/m^{2}K^4)	5.67E-08	5.67E-08	5.67E-08	5.67E-08	5.67E-08	5.67E-08	5.67E-08	5.67E-08
t_p (in)	0.72	0.72	0.72	0.72	0.72	0.72	0.72	0.72
C_k	0.90	0.90	0.90	0.90	0.90	1.05	1.10	1.05
E (V)	6.00	6.00	6.00	5.87	5.87	5.87	6.19	6.05
I (A)	2.07	2.07	2.07	2.64	2.64	2.61	2.75	2.60
k_p (W/mK)	0.205	0.205	0.205	0.205	0.205	0.205	0.205	0.205
T_{SS} (K)	314.70	315.69	316.23	310.44	311.91	307.47	307.01	307.37
T_{UP} (K)	297.71	298.56	299.15	298.92	299.05	298.78	298.94	299.11
T_∞ (K)	295.47	295.47	295.47	295.47	295.47	295.47	295.47	295.47
T_{IR} (K)	304.48	306.44	307.67	306.61	306.50	302.15	301.92	302.35
h (W/m^{2}K)	36.04 ± 2.18	28.37 ± 2.03	24.90 ± 1.90	32.05 ± 0.64	31.22 ± 0.75	58.69 ± 2.61	70.56 ± 3.65	59.68 ± 2.84

Table A.6: Accelerated and tripped 113012.04_RealIce aluminum case

Parameter	0a	0b	0c	1a	1b	2	3	4
x (in)	3.10	4.48	5.85	9.23	10.98	18.23	25.48	32.73
A_t (in^2)	35.06	35.06	35.06	44.62	44.62	44.62	44.62	44.62
ε	0.95	0.95	0.95	0.95	0.95	0.95	0.95	0.95
σ (W/m^{2}K^4)	5.67E-08	5.67E-08	5.67E-08	5.67E-08	5.67E-08	5.67E-08	5.67E-08	5.67E-08
t_p (in)	0.72	0.72	0.72	0.72	0.72	0.72	0.72	0.72
C_k	0.90	0.90	0.90	0.90	0.90	1.05	1.10	1.05
E (V)	5.97	5.97	5.97	5.86	5.86	5.87	6.18	6.05
I (A)	2.09	2.09	2.09	2.65	2.65	2.61	2.75	2.63
k_p (W/mK)	0.205	0.205	0.205	0.205	0.205	0.205	0.205	0.205
T_{SS} (K)	312.80	314.48	315.06	308.04	309.53	306.58	306.28	306.88
T_{UP} (K)	296.85	297.69	298.42	297.96	297.99	298.06	298.29	298.58
T_∞ (K)	295.07	295.07	295.07	295.07	295.07	295.07	295.07	295.07
T_{IR} (K)	302.22	303.69	304.68	303.72	303.54	301.06	301.18	301.65
h (W/m^{2}K)	48.77 ± 1.95	38.43 ± 2.16	34.01 ± 2.13	44.79 ± 1.36	44.10 ± 1.56	66.21 ± 3.09	74.88 ± 4.00	63.45 ± 3.04

Table A.7: Accelerated and tripped 113012.04_IRT_cones plastic case

Parameter	0a	0b	0c	1a	1b	2	3	4
x (in)	3.10	4.48	5.85	9.23	10.98	18.23	25.48	32.73
A_t (in^2)	35.06	35.06	35.06	44.62	44.62	44.62	44.62	44.62
ε	0.95	0.95	0.95	0.95	0.95	0.95	0.95	0.95
σ (W/m^{2}K^4)	5.67E-08	5.67E-08	5.67E-08	5.67E-08	5.67E-08	5.67E-08	5.67E-08	5.67E-08
t_p (in)	0.72	0.72	0.72	0.72	0.72	0.72	0.72	0.72
C_k	0.90	0.90	0.90	0.90	0.90	1.05	1.10	1.05
E (V)	5.93	5.93	5.93	5.90	5.90	5.88	6.25	6.00
I (A)	2.11	2.11	2.11	2.64	2.64	2.61	2.74	2.63
k_p (W/mK)	0.205	0.205	0.205	0.205	0.205	0.205	0.205	0.205
T_{SS} (K)	311.81	313.77	314.68	316.29	317.99	312.54	317.11	312.54
T_{UP} (K)	295.61	296.44	297.20	298.14	298.26	298.47	299.94	299.27
T_∞ (K)	294.27	294.27	294.27	294.27	294.27	294.27	294.27	294.27
T_{IR} (K)	300.76	302.12	303.14	303.65	304.04	299.96	300.61	301.79
h (W/m^{2}K)	54.32 ± 1.28	42.39 ± 2.04	36.67 ± 2.12	32.37 ± 1.48	29.18 ± 1.36	59.07 ± 3.92	54.87 ± 4.70	46.34 ± 2.71

Table A.8: Accelerated and tripped 113012.04_IRT_cones aluminum case

Parameter	0a	0b	0c	1a	1b	2	3	4
x (in)	3.10	4.48	5.85	9.23	10.98	18.23	25.48	32.73
A_t (in^2)	35.06	35.06	35.06	44.62	44.62	44.62	44.62	44.62
ε	0.95	0.95	0.95	0.95	0.95	0.95	0.95	0.95
σ (W/m^2K^4)	5.67E-08	5.67E-08	5.67E-08	5.67E-08	5.67E-08	5.67E-08	5.67E-08	5.67E-08
t_p (in)	0.72	0.72	0.72	0.72	0.72	0.72	0.72	0.72
C_k	0.90	0.90	0.90	0.90	0.90	1.05	1.10	1.05
E (V)	5.94	5.94	5.94	5.85	5.85	5.80	6.12	5.98
I (A)	2.10	2.10	2.10	2.66	2.66	2.63	2.78	2.61
k_p (W/mK)	0.205	0.205	0.205	0.205	0.205	0.205	0.205	0.205
T_{SS} (K)	314.13	315.69	316.35	309.22	309.94	307.01	309.66	314.60
T_{UP} (K)	298.00	298.68	299.30	298.74	298.97	298.92	299.70	300.99
T_∞ (K)	296.03	296.03	296.03	296.03	296.03	296.03	296.03	296.03
T_{IR} (K)	303.24	304.65	305.67	304.95	304.69	302.37	303.04	304.11
h (W/m^2K)	48.22 ± 1.92	38.30 ± 2.13	33.54 ± 2.10	43.05 ± 1.28	43.92 ± 1.43	62.90 ± 2.77	61.00 ± 3.35	41.45 ± 2.44

Table A.9: Accelerated and tripped 052996.04_x10_SSL_cones plastic case

Parameter	0a	0b	0c	1a	1b	2	3	4
x (in)	3.10	4.48	5.85	9.23	10.98	18.23	25.48	32.73
A_t (in^2)	35.06	35.06	35.06	44.62	44.62	44.62	44.62	44.62
ε	0.95	0.95	0.95	0.95	0.95	0.95	0.95	0.95
σ (W/m^2K^4)	5.67E-08	5.67E-08	5.67E-08	5.67E-08	5.67E-08	5.67E-08	5.67E-08	5.67E-08
t_p (in)	0.72	0.72	0.72	0.72	0.72	0.72	0.72	0.72
C_k	0.90	0.90	0.90	0.90	0.90	1.05	1.10	1.05
E (V)	5.96	5.96	5.96	5.90	5.90	5.90	6.32	5.97
I (A)	2.11	2.11	2.11	2.65	2.65	2.61	2.74	2.62
k_p (W/mK)	0.205	0.205	0.205	0.205	0.205	0.205	0.205	0.205
T_{SS} (K)	312.03	313.89	314.74	317.36	317.37	313.39	316.79	313.35
T_{UP} (K)	295.74	296.62	297.45	298.61	298.46	298.86	300.17	299.79
T_∞ (K)	294.28	294.28	294.28	294.28	294.28	294.28	294.28	294.28
T_{IR} (K)	301.08	302.52	303.62	301.83	299.45	299.95	300.75	301.09
h (W/m^2K)	51.75 ± 1.70	40.45 ± 2.12	35.00 ± 2.13	41.03 ± 2.48	62.27 ± 5.84	58.51 ± 3.98	55.73 ± 4.57	50.41 ± 3.20

Table A.10: Accelerated and tripped 052996.04_x10_SSL_cones aluminum case

Parameter	0a	0b	0c	1a	1b	2	3	4
x (in)	3.10	4.48	5.85	9.23	10.98	18.23	25.48	32.73
A_t (in^2)	35.06	35.06	35.06	44.62	44.62	44.62	44.62	44.62
ε	0.95	0.95	0.95	0.95	0.95	0.95	0.95	0.95
σ (W/m^{2}K^4)	5.67E-08	5.67E-08	5.67E-08	5.67E-08	5.67E-08	5.67E-08	5.67E-08	5.67E-08
t_p (in)	0.72	0.72	0.72	0.72	0.72	0.72	0.72	0.72
C_k	0.90	0.90	0.90	0.90	0.90	1.05	1.10	1.05
E (V)	5.95	5.95	5.95	5.85	5.85	5.89	6.16	5.97
I (A)	2.11	2.11	2.11	2.68	2.68	2.63	2.77	2.63
k_p (W/mK)	0.205	0.205	0.205	0.205	0.205	0.205	0.205	0.205
T_{SS} (K)	312.10	313.71	314.29	304.09	304.77	303.71	305.65	312.90
T_{UP} (K)	295.66	296.42	297.08	296.14	296.10	296.30	296.95	298.73
T_∞ (K)	293.99	293.99	293.99	293.99	293.99	293.99	293.99	293.99
T_{IR} (K)	300.82	302.27	303.32	299.87	299.50	299.50	300.36	300.88
h (W/m^{2}K)	51.32 ± 1.66	40.21 ± 2.11	35.11 ± 2.12	73.09 ± 3.13	77.07 ± 3.81	76.10 ± 3.48	70.64 ± 3.84	49.25 ± 3.17

REFERENCES

[1] Leary, W. M., 2002, *We Freeze to Please: A History of NASA's Icing Research Tunnel and the Quest for Flight Safety*, No. NAS 1.21: 4226

[2] Petty, K. R., and Floyd, C. D. J., 2004, *A Statistical Review of Aviation Airframe Icing Accidents in the U.S.*, 11th American Society for Microbiology Conference on Aviation, Range, and Aerospace, Hyannis, MA.

[3] Addy, H. E., 2000, "Ice Accretions and Icing Effects for Modern Airfoil," NASA/TP-2000-210031.

[4] Olsen, W., Walker, E., 1986, "Experimental Evidence for Modifying the Current Physical Model for Ice Accretion on Aircraft Surfaces," NASA TM-87184.

[5] Vargas, M., 2007, "Current Experimental Basis for Modeling Ice Accretions on Swept Wings," *Journal of Aircraft* **44**(1), pp. 274-290.

[6] Goraj, Z., 2004, "An Overview of the Deicing and Antiicing Technologies with Prospects for the Future," *24th International Congress of the Aeronautical Sciences* (ICAS), Yokohama.

[7] Gent, R. W., Dart, N. P., and Cansdale, J.T., 2000, "Aircraft Icing," *Philosophical Transactions: Mathematical, Physical, and Engineering Sciences*, **358**(1776), pp. 2873-2911.

[8] "14 CFR Part 25: Airworthiness Standards: Transport Category Airplanes - Appendix C, Part I: Atmospheric Icing Conditions," 2012, *Code of Federal Regulations*.

[9] "14 CFR Part 25: Airworthiness Standards: Transport Category Airplanes - Appendix O, Part I: Meteorology," 2014, *Code of Federal Regulations*.

[10] Cebeci, T., and Kafyeke, F., 2003, "Aircraft Icing," *Annual Review of Fluid Mechanics*, **35**, pp. 11-21.

[11] Wright, W.B., 2002, "User Manual for the NASA Glenn Ice Accretion Code LEWICE," NASA/CR-2002-211793.

[12] Wright W. B., Rutkowski, A., 1999, "Validation Results for LEWICE 2.0," NASA, NASA/CR-1999-208690, Cleveland, OH.

[13] Tecson, L., 2013, “Convective Heat Transfer from Realistic Ice Roughness Distributions,” MS thesis, Department of Mechanical Engineering, Baylor University.

[14] Walker, C. W., 2014, “Convection from Manufactured Ice Roughness with Varying Flux Boundary Conditions,” MS thesis, Department of Mechanical Engineering, Baylor University.

[15] McClain, S.T. and Kreeger, R.E., 2013, “Assessment of Ice Shape Roughness Using a Self-Organizing Map Approach,” Presented at the 5th AIAA Atmospheric and Space Environments Conference, June 24-27, 2013, San Diego, CA, AIAA-2013-2546.

[16] McClain, S.T., Reed, D., Vargas, M., Kreeger, R.E., and Tsao, J.-C., 2014, “Ice roughness in Short Duration SLD Icing Events,” 6th AIAA Atmospheric and Space Environments Conference, 16-20 June, Atlanta, GA, AIAA-2014-2330.

[17] Shannon, T. A., 2015, “Convection from Realistic Ice Roughness on a Simulated NACA 0012 Airfoil,” MS thesis, Department of Mechanical Engineering, Baylor University.

[18] Hughes, M. T., 2015, “Convective Enhancement on Airfoils Due to Ice Roughness Elements in Stagnation Region Flows,” MS thesis, Department of Mechanical Engineering, Baylor University.

[19] Lee, S., Broeren, A. P., Addy, H. E. Jr., Sills, R., and Pifer, E. M., 2012, “Development of 3-D Ice Accretion Measurement Method,” NASA/TM-2012-217702, Cleveland, OH, AIAA-2012-2938.

[20] Anderson, J. D. Jr., 2005, “Ludwig Prandtl’s Boundary Layer,” Physics Today, American Institute of Physics, S-0031-9228-0512-020-1

[21] Munson, B. R., Okiishi, T.H., Huebsch, W.W., and Rothmayer, A.P., 2013, *Fundamentals of Fluid Mechanics*, 7th ed., John Wiley & Sons, Inc., Hoboken, NJ.

[22] Bejan, A., 2004, *Convection Heat Transfer*, 3rd ed., John Wiley & Sons, Inc., Hoboken, NJ.

[23] White, F. M., 2006, *Viscous Fluid Flow*, 3rd Ed, Boston, McGraw-Hill, Inc., New York, NY.

[24] Moran, M. J., and Shapiro, H. N., 2008, *Fundamentals of Engineering Thermodynamics*, 6th ed., John Wiley & Sons, Inc., Hoboken, NJ.

[25] Smith, A.G., and Spaulding, D.B., (1958), “Heat Transfer in a Laminar Boundary Layer with Constant Fluid Properties and Constant Wall Temperature,” *J. Roy. Aero. Soc.*, Vol. 62, pg 60-64.

[26] Ambrok, G. S., (1957), “Approximate Solutions of the Equations for the Thermal Boundary Layer with Variations in the Boundary Layer Structure,” *Soviet Phys.-Tech. Phys.*, Vol. 2, No. 9, pg 1979-1986.

[27] Von Mises, R., 1914, “Elemente der Technischen Hydrodynamik,” Leipzig, B. G. Teubner.

[28] Nikuradse, J., 1933, “Laws for Flows in Rough Pipes,” *VDI-Forschungsheft*, **4**, pp. 361.

[29] Schlichting, H., 1936, “Experimental Investigation of the Problem of Surface Roughness,” TM-832, National Advisory Committee on Aeronautics.

[30] Bons, J. P., and McClain, S. T., 2004, “The Effect of Real Turbine Roughness with Pressure Gradient on Heat Transfer,” *Journal of Turbomachinery*, Vol. 126, No. 3, pg 385-394.

[31] Bons, J. P., 2002, “St and Cf Augmentation for Real Turbine Roughness With Elevated Freestream Turbulence,” *Journal of Turbomachinery*, **124**, pp. 632–644.

[32] McClain, S. T., Hodge, B. K., and Bons, J. P., 2011, “The Effect of Element Thermal Conductivity on Turbulent Conductive Heat Transfer from Rough Surfaces,” *Journal of Turbomachinery*, Vol. 133, pp 021024.

[33] McClain, S. T., Vargas, M., Kreeger, R. E., and Tsao, J. C., 2007, “Heat Transfer from Protuberances”, *Journal of Thermophysics and Heat Transfer*, **21**(2), pp. 337-345.

[34] Wang, Z.J., Chi, X.K., Shih, T., and Bons, J.P., 2004, “Direct Simulation of Surface Roughness Effects with RANS and DES Approaches on Viscous Adaptive Cartesian Grids,” AIAA-2004-2420.

[35] Bons, J. P., McClain, S. T., Wang, Z. J., Chi, X., Shih, T. I., 2005, “A Comparison of approximate vs. Exact Geometrical Representations of Roughness for CFD Calculations of C_f and St,” ASME International Mechanical Engineering Congress and Exposition.

[36] Reehorst, A. L., and Richter, G. P., 1987, “New Methods for Molding and Casting Ice Formations,” NASA Technical Memorandum 100126.

[37] Lee, J. D., Harding, R., and Palko, R. L., 1984, "Documentation of Ice Shapes on the Main Rotor of a UH-1H Helicopter in Hover," NASA Contractor Report 168332.

[38] Hovenac, E. A., Vargas, M., 1995, "A Laser-Based Shape Profilometer for Use in Icing Wind Tunnels," NASA Technical Memorandum 106936.

[39] Wilder, R. W., 1978, "A Theoretical and Experimental Means to Predict Ice Accretion Shapes for Evaluating Aircraft Handling and Performance Characteristics," AGARD Advisory Report No. 127, Aircraft Icing.

[40] Hanson, M. K., and Lee, J. D., 1986, "Documentation of Ice Shapes Accreted on the Main Rotor of a UH-1H Helicopter in Level Flight," NASA Contractor Report 175088

[41] Lee, J. D., Berger, J. H., and McDonald, T. J., 1986, "Wind Tunnel Tests of Rotor Blade Sections with Replications of Ice Formations Accreted in Hover," NASA Contractor Report 175089.

[42] Kind, R. J., Potapczuk, M. G., Feo, A., Golia, C., and Shah, A. D., 1998, *Experimental and Computational Simulation of In-Flight Icing Phenomena*, Elsevier Science Ltd., 0376-0421/98

[43] Vannuyen, T., 1998, *Process Developed for Forming Urethane Ice Models*, Technical Report, NASA Lewis Research Center, 20050181946.

[44] Han, Y. and Palacios, J., (2014), "Transient Heat Transfer Measurements of Surface Roughnes due to Ice Accretion," 6th AIAA Atmospheric and Space Environments Conference, 16-20 June, Atlanta, GA, AIAA-2014-2464.

[45] Shin, J., 1994, "Characteristics of Surface Roughness Associated With Leading Edge Ice Accretion," NASA TM-106459.

[46] Anderson, D. N., Hentschel, D. B., and Ruff, G. A., 1998, "Measurement and Correlation of Ice Accretion Roughness," NASA CR-2003-211823.

[47] Broeren, A. P., Addy, H. E. Jr., Lee, S., and Monastero, M. C., "Validation of 3-D Ice Accretion Methodology for Experimental Aerodynamic Simulation," NASA/TM-2015-218724, Cleveland, OH, AIAA-2014-2614.

[48] Barbagallo, J., 2015, Deputy Director, Flight Standards Service, "Pilot Guide: Flight in Icing Conditions," Advisory Circular, U.S. Department of Transportation, AC No: 91-74B.

[49] Bragg, M. B., Cummings, M. J., Lee, S., Henze, C. M., 1996, “Boundary-Layer and Heat-Transfer Measurements on an Airfoil with Simulated Ice Roughness,” AIAA Paper 96-0866.

[50] Anderson, D. N., and Shin, J., 1997, “Characterization of Ice Roughness from Simulated Icing Encounters,” NASA TM-107400.

[51] Poinsatte, P.E., Van Fossen, G.J., and DeWitt, K.J., 1990, “Convective Heat Transfer Measurements from a NACA 0012 Airfoil in Flight and in the NASA Lewis Icing Research Tunnel,” NASA TM-102448.

[52] Messinger, B.L., 1953, “Equilibrium Temperature of an Unheated Icing Surface as a Function of Air Speed,” *Journal of Aeronautical Sciences*, pp. 29-42.

[53] Myers, T.G., and Hammond, D.W., 1999, “Ice and Water Film Growth from Incoming Supercooled Droplets,” *International Journal of Heat and Mass Transfer*, **42**, pp. 2233-2242.

[54] Coleman, H. W., Hodge, B. K., Taylor, R. P., 1984, “A Re-Evaluation of Schlichting’s Surface Roughness Experiment,” *Transactions of the ASME*, **60**/Vol. 106.

[55] Van Fossen, G. J., Simoneau, R. J., Olsen, W. A., Shaw, K. J., 1984, “Heat Transfer Distributions around Nominal Ice Accretion Shapes Formed on a Cylinder in the NASA Lewis Icing Research Tunnel,” NASA TM 83557.

[56] Bragg, M. B., Kerho, M. F., and Cummings, M. J., 1994, “Effect of Initial Ice Roughness on Airfoil Aerodynamics,” AIAA-94-0800.

[57] Coleman, H. W., Moffat, R. J., and Kays, W. M., 1981, “Heat Transfer in the Accelerated Fully Rough Turbulent Boundary Layer,” *Journal of Heat Transfer*, Vol. 103, No. 1, pp. 153-158.

[58] Chakroun, W., and Taylor, R. P., 1993, “The Effects of Moderately Strong Acceleration on Heat Transfer in the Turbulent Rough-Wall Boundary Layer,” *Journal of Heat Transfer*, Vol. 115, No. 3, pp. 1187-1201.

[59] Turner, A. B., Hubbe-Walker, S. E., and Bayley, F. J., 2000, “Fluid Flow and Heat Transfer Over Straight and Curved Rough Surfaces,” *Int. Journal of Heat Transfer*, Vol. 43, pp. 251-262.

[60] Reehorst, A.L., 1992, “Prediction of Ice Accretion on a Swept NACA 0012 Airfoil and Comparisons to Flight Test Results,” AIAA Paper 92-0043.

[61] Henry, R., Guffond, D., Aschettino, S., and Duprat, G., 2001, "Characterization of Ice Roughness and Influence on Aerodynamic Performance of Simulated Ice Shapes," 3rd AIAA Aerospace Sciences Meeting and Exhibit, 8-11 January, Reno, NV, AIAA-2001-0092.

[62] Bons, J. P., Taylor, R. P., McClain, S. T., and Rivir, R. B., 2001, "The Many Faces of Turbine Surface Roughness," *Journal of Turbomachinery*, Vol. 123, pp 739-748.

[63] Dukhan, N., Van Fossen, G. J., DeWitt, K. J., Masiulaniec, K. C., 2003, "Experimental Frossling Numbers for Ice-Roughened NACA 0012 Airfoils," *Journal of Aircraft* **40**(6), pp. 1161-1167.

[64] Croce, G., De Candido, E., Habashi, W. G., Munzar, J., Aubé M. S., Baruzzi, G. S., and Aliaga, C., 2010, "FENSAP-ICE: Analytical Model for Spatial and Temporal Evolution of In-Flight Icing Roughness," *Journal of Aircraft*, **47**(4), pp. 1283-1289.

[65] Tecson, L. and McClain, S.T., 2013, "Modeling of Realistic Ice Roughness Element Distributions to Characterize Convective Heat Transfer," 5th AIAA Atmospheric and Space Environments Conference, 24-27 June, San Diego, CA, AIAA-2013-3059.

[66] Tecson, L. and McClain, S.T., 2013, "Convective Enhancement of Surfaces with Realistic Ice Roughness Distributions," 5th AIAA Atmospheric and Space Environments Conference, 24-27 June, San Diego, CA, AIAA-2013-3060.

[67] Walker C. W., McClain S. T., and Shannon T. A., 2014, "Convection from Ice Roughness with Varying Flux Boundary Conditions," 6th AIAA Atmospheric and Space Environments Conference, 16-20 June, Atlanta, GA, AIAA-2014-2463.

[68] McClain, S. T., Tiňo, P., and Kreeger, R. E., 2011, "Ice Shape Characterization Using Self-Organizing Maps," *Journal of Aircraft*, **48**(2), pp. 724-729.

[69] McClain, S. T., Vargas, M., Kreeger, R. E., and Tsao, J., 2015, "A Reevaluation of Appendix C Ice Roughness Using Laser Scanning," SAE Technical Paper 2015-01-2098, 2015, doi:10.4271/2015-01-2098.

[70] Shannon, T. A., and McClain, S. T., 2015, "Convection from a Simulated NACA 0012 Airfoil with Realistic Ice Accretion Roughness Variations," SAE Technical Paper 2015-01-2097, 2015, doi:10.4271/2015-01-2097.

[71] Shannon, T. A., and McClain, S. T., 2016, "Convection from a Simulated NACA 0012 with Icing Roughness of Different Shape and Thermal Conductivity," 8th AIAA Atmospheric and Space Environments Conference, 13-17 June, Washington, DC, AIAA-2016-3588.

[72] McClain, S. T., 2016, "Manual Point Cloud Registration for Combined Ice Roughness and Ice Thickness Measurements," 8th AIAA Atmospheric and Space Environments Conference, June 13-17, Washington, DC, AIAA-2016-3590.

[73] The International Association for the Properties of Water and Steam, 2007, "Revised Release on the IAPWS Industrial Formulation 1997 for the Thermodynamic Properties of Water and Steam," http://www.iapws.org/.

[74] Wilke, C. R., 1950, "A Viscosity Equation for Gas Mixtures," *Journal of Chemical Physics*, **18**(4), pp. 517-519.

[75] Coleman, H. W., and Steele, W. G., 1999, *Experimentation and Uncertainty Analysis for Engineers*, 2nd ed., John Wiley and Sons, Inc., Hoboken, NJ.

[76] Kline, S. J., and McClintock, F. A., 1953, "Describing Uncertainties in Single-Sample Experiments," *Mechanical Engineering*, **75**, pp. 3-8.